Associated Higgs production at Tevatron and LHC

Diplomarbeit der Fakultät für Physik
der
Ludwig-Maximilians-Universität München

vorgelegt von

Michael Bussmann
aus
Bielefeld

Februar 2002

Erstgutachterin *Frau Professorin Dr. Dorothee Schaile*
Zweitgutachter *Herr Professor Dr. Christian Kiesling*

Für meine Eltern.

Contents

1 Theory **17**
- 1.1 Standard Model 17
  - 1.1.1 Overview 17
  - 1.1.2 Local gauge invariance 18
  - 1.1.3 Electroweak Interaction 20
  - 1.1.4 Strong Interaction 21
  - 1.1.5 Standard Model Higgs 22
- 1.2 Signals 26
  - 1.2.1 Signal Z^0H 26
  - 1.2.2 Signal $W^{\pm}H$ 28
- 1.3 Backgrounds 29
  - 1.3.1 Continuous backgrounds 29
  - 1.3.2 Resonant Backgrounds 32

2 Colliders **35**
- 2.1 Hadron Collider Physics 35
  - 2.1.1 Parton distribution functions 35
  - 2.1.2 Dynamic processes 39
  - 2.1.3 Particle production 42
  - 2.1.4 Machine parameters 42
- 2.2 Tevatron 43
  - 2.2.1 Accelerator Chain 44
  - 2.2.2 The Tevatron 46
- 2.3 LHC 46
  - 2.3.1 Accelerator Chain 46
  - 2.3.2 The LHC 46
- 2.4 Comparison 48

3 Detectors **49**
- 3.1 Physics Requirements 49
  - 3.1.1 Coordinate System 49
  - 3.1.2 Operation at high luminosity 49
  - 3.1.3 Transverse momentum 50
  - 3.1.4 Energy 51

3.1.5 Lepton ID 51
3.1.6 Missing transverse energy 52
3.1.7 Jet energy 52
3.1.8 b-jet ID 53
3.2 DØ 55
3.2.1 Overview 55
3.2.2 Inner detector 55
3.2.3 Calorimeters 57
3.2.4 Muon spectrometer 59
3.3 ATLAS 60
3.3.1 Overview 60
3.3.2 Inner Detector 60
3.3.3 Calorimeters 63
3.3.4 Muon spectrometer 65
3.4 Comparison 67
3.4.1 Particle Identification 67
3.4.2 Lepton ID 67
3.4.3 Jet ID 69
3.4.4 b-jet ID 69
3.4.5 Summary 69

4 Event generation and detector simulation 71
4.1 Monte Carlo 71
4.1.1 Introduction 71
4.1.2 Higgs boson mass 72
4.1.3 Decay channels 73
4.1.4 Additional settings 74
4.1.5 Choice of PDF 76
4.1.6 Cross sections 77
4.2 Fast simulations 79
4.2.1 PGS 79
4.2.2 ATLFast 80

5 Analysis 85
5.1 Event reconstruction 85
5.1.1 Physics objects 85
5.1.2 Interface 86
5.1.3 Analysis Maker 86
5.1.4 Jet momentum calibration 88
5.1.5 Tagging 90
5.1.6 Cone radius 93
5.1.7 Di-jet mass resolution 95
5.2 Analysis $l^+l^-b\bar{b}$ 97
5.2.1 Event characterization 97
5.2.2 Kinematic variables 107

5.2.3 Event selection 110
5.3 Analysis $l^{\pm}\nu b\bar{b}$ 113
5.3.1 Event characterization 113
5.3.2 Kinematic variables 121
5.3.3 Event selection 122

6 Results **123**
6.1 Results for $l^{+}l^{-}b\bar{b}$ 123
6.1.1 Efficiencies 123
6.1.2 Significance 125
6.2 Results $l^{\pm}\nu b\bar{b}$ 130
6.2.1 Efficiencies 130
6.2.2 Significance 132
6.2.3 Combination of results 136

7 Conclusion and Outlook **139**

A Pythia settings **141**

B Pythia branching ratios **142**

C ATLFast parameters **143**
C.1 Cluster parameters 143
C.2 Lepton parameters 144
C.3 Jet parameters 145

List of Figures

1.1 *Leading order Feynman diagram for the process* $q_i\bar{q}_i \to Z^0H$, *including decay channels* 26
1.2 *Branching ratios of the different Higgs boson decay channels* . . . 27
1.3 *Leading order Feynman diagram for the process* $q_i\bar{q}_j \to W^{\pm}H$, *including decay channels* 29
1.4 *Leading order Feynman diagrams for the processes* $q_i\bar{q}_i \to b\bar{b}$ *and* $gg \to b\bar{b}$ 30
1.5 *Leading order Feynman diagrams for single top production, including decay channels* 31
1.6 *Leading order Feynman diagrams for the* $t\bar{t}$ *final states.* 32
1.7 *Leading order Feynman diagrams for the* $W^{\pm}b\bar{b}$ *and* $Z^0b\bar{b}$ *final states.* 33
1.8 *Leading order Feynman diagrams for the resonant backgrounds, including decay channels* 34

2.1 *Peterson fragmentation functions as used in the Monte Carlo generation* 40
2.2 *Schematic view of the Tevatron accelerator chain* 44
2.3 *Schematic view of the LHC accelerator chain* 47

3.1 *Momentum measurement in a solenoid magnet* 50
3.2 *Definition of the signed impact parameter* 54
3.3 *Schematic view of the DØ detector* 55
3.4 *Side view of the DØ Inner Detector* 56
3.5 *Schematic view of the ATLAS detector* 61
3.6 *Side view of the ATLAS Inner Detector* 62

4.1 *Kinematic map of the experiments used for the CTEQ5M1 parton distribution function [34]* 76

5.1 *Jet momentum calibration factor for b-jets and light jets* 88
5.2 *Calibrated jet momentum calibration for b-jets and light jets* . . . 89
5.3 *Parameterized b-tagging efficiency for DØ and ATLAS* 90
5.4 *Parameterized mistagging probability for charm flavoured jets* . . 91
5.5 *Parameterized mistagging probability for light jets, including hadronically decaying tau leptons* 92

5.6 *Reconstructed invariant mass and number of b-jet pairs for DØ (top: ATLFast, bottom: PGS)* 94
5.7 *Reconstructed invariant mass and number of b-jet pairs for ATLAS* 95
5.8 *Reconstructed invariant mass of b-jet pairs for DØ (left: ATLFast, right: PGS)* 96
5.9 *Reconstructed invariant mass of b-jet pairs for ATLAS* 96
5.10 *Number of b-tagged jets for DØ, final state* $l^+l^-b\bar{b}$ 98
5.11 *Number of b-tagged jets for ATLAS, final state* $l^+l^-b\bar{b}$ 99
5.12 *Difference between the PGS and the ATLFast simulation in the reconstruction efficiency for electrons.* 101
5.13 *Differences in the* p_T *distribution for the light lepton with the highest transverse momentum in the final state* $l^+l^-b\bar{b}$ *between the ATLFast (top) and the PGS (bottom) simulation of the DØ detector* 103
5.14 *Number of leptons for DØ, final state* $l^+l^-b\bar{b}$ 104
5.15 *Number of leptons for ATLAS, final state* $l^+l^-b\bar{b}$ 105
5.16 p_T *distribution for the b-jet with the highest transverse momentum, final state* $l^+l^-b\bar{b}$*, obtained with the* ATLFAST *simulation of the* DØ *detector for a Higgs mass of 115 GeV/*c^2 107
5.17 *Invariant mass of the two OSSF leptons in the final state* $l^+l^-b\bar{b}$*, obtained with the ATLFast simulation of the DØ detector for a Higgs mass of 115 GeV/*c^2 108
5.18 *Invariant mass of the b-jet pair for signal and resonant background in the final state* $l^+l^-b\bar{b}$*, obtained with the ATLFast simulation of the DØ detector for a Higgs mass of 115 GeV/*c^2 109
5.19 *Invariant mass of the b-jet pair for signal and continuous background in the final state* $l^+l^-b\bar{b}$*, obtained with the* ATLFAST *simulation of the DØ detector for a Higgs mass of 115 GeV/*c^2 . . . 111
5.20 *Invariant mass of the b-jet pair for signal and continuous background in the final state* $l^+l^-b\bar{b}$*, obtained with the* ATLFAST *simulation of the ATLAS detector for a Higgs mass of 115 GeV/*c^2 . 113
5.21 *Missing transverse energy in the final state* $l^{\pm}\nu b\bar{b}$*, obtained with the* ATLFAST *simulation of the* DØ *detector for a Higgs mass of 115 GeV/*c^2 114
5.22 *Number of b-tagged jets for DØ, final state* $l\nu b\bar{b}$ 115
5.23 *Number of b-tagged jets for ATLAS, final state* $l\nu b\bar{b}$ 116
5.24 *Differences in the* p_T *distribution for the light lepton in the final state* $l^{\pm}\nu b\bar{b}$ *between the ATLFast (top) and the PGS (bottom) simulation of the DØ detector* 117
5.25 *Number of leptons for DØ, final state* $l\nu b\bar{b}$ 118
5.26 *Number of leptons for ATLAS, final state* $l\nu b\bar{b}$ 119

6.1 *Significance v.s integrated luminosity for the* Z^0H *process at a center of mass energy of 2 TeV.* 127

6.2 *Significance v.s integrated luminosity for the* Z^0H *process at a center of mass energy of 14 TeV.* 128
6.3 *Significance v.s integrated luminosity for the* $W^{\pm}H$ *process at a center of mass energy of 2 TeV.* 132
6.4 *Significance v.s integrated luminosity for the* $W^{\pm}H$ *process at a center of mass energy of 14 TeV.* 135
6.5 *Significance v.s integrated luminosity for the combined signal processes at a center of mass energy of 2 TeV.* 136
6.6 *Significance v.s integrated luminosity for the combined signal processes at a center of mass energy of 14 TeV.* 137

List of Tables

1.1 Elementary fermions in the Standard Model 17
1.2 Gauge bosons and interactions 18
1.3 Electroweak gauge bosons and their masses 24

2.1 Tevatron and LHC 48

4.1 Monte Carlo generation – Number of events 71
4.2 Restrictions on the decay channels set for different Monte Carlo samples 73
4.3 Branching ratios 75
4.4 Cross section × branching ratio for the signal process $W^{\pm}H$ and Z^0H obtained from Pythia [fb] 77
4.5 Cross section × branching ratio for the background processes $W^{\pm}H$ and Z^0H obtained from Pythia [fb] 78

5.1 Accepted cross sections for the final state $l^+l^-b\bar{b}$ 106
5.2 Accepted cross sections for the final state $l\nu b\bar{b}$ 120

6.1 Reduction efficiencies for $l^+l^-b\bar{b}$ at the Tevatron center of mass energy 124
6.2 Reduction efficiencies for $l^+l^-b\bar{b}$ at the LHC center of mass energy 125
6.3 Expected number of events for processes with the final state $l^+l^-b\bar{b}$ at 2 TeV center of mass energy 126
6.4 Expected number of events for processes with the final state $l^+l^-b\bar{b}$ at 14 TeV center of mass energy 129
6.5 Reduction efficiencies for $l\nu b\bar{b}$ at the Tevatron center of mass energy 130
6.6 Reduction efficiencies for $l\nu b\bar{b}$ at the LHC center of mass energy 131
6.7 Expected number of events for processes with the final state $l^{\pm}\nu b\bar{b}$ at 2 TeV center of mass energy 133
6.8 Expected number of events for processes with the final state $l^{\pm}\nu b\bar{b}$ at 14 TeV center of mass energy 134

A.1 Initial Pythia settings 141

A.2 **Individual settings for $W^{\pm}b\bar{b}$ and $Z^0b\bar{b}$** 141

B.1 **Branching ratios obtained from Pythia** 142

C.1 **ATLFast cluster parameters** 143
C.2 **Explanation of ATLFast cluster parameters** 143
C.3 **ATLFast electron parameters** 144
C.4 **ATLFast muon parameters** 144
C.5 **ATLFast tau parameters** 144
C.6 **Explanation of ATLFast lepton parameters** 144
C.7 **ATLFast jet parameters** 145
C.8 **ATLFast b-jet parameters** 145
C.9 **Explanation of ATLFast jet parameters** 145

Introduction

The Standard Model of particle physics describes all the elementary particles and their interactions known today. The theoretical foundation of the Standard Model is the so called principle of local gauge invariance, which governed the development of the two parts of the Standard Model, the theory of electroweak interactions and quantum-chromo-dynamics.

With the discovery of the W boson and the Z^0 at the Super Proton Synchrotron at CERN (**C**onseil **E**uropéenne pour le **R**echerche Nucléaire) and the following precision measurements of many Standard model parameters at LEP (**L**arge **e**lectron **p**ositron collider) the Standard model has proven to be successful.

Today the Higgs boson is the only particle predicted by the Standard Model which has not yet been observed. It has been introduced to describe massive particles in a local gauge invariant model. If no Higgs boson is discovered the Standard Model will have to be changed.

The mass of the Higgs boson is a free parameter in the Standard Model. Results obtained at LEP [1] have ruled out with a 95% confidence level the existence of a Standard Model Higgs boson with a mass lighter than 114.1 GeV/c^2.

With the start of the TEVATRON Run II in March 2001 and the LHC (**L**arge **h**adron **c**ollider) beginning its operation in 2006 the search for the Higgs boson continues.

In this thesis the propects of finding a Standard Model Higgs boson with a mass in the range of 115 GeV/c^2 to 130 GeV/c^2 produced in association with a Z^0 or $W^\pm$ are presented for both the TEVATRON and LHC center of mass energy.

In the case of the TEVATRON the predictions of previous studies showed a considerable spread. In this thesis a direct comparison using two different fast detector simulations, ATLFAST and PGS, which resemble the performance of the upgraded DØ detector at the TEVATRON is presented.

For the ATLAS detector the discovery prospects for a Higgs boson via associated production were compared to the TEVATRON case.

All final states including light charged leptons entered the analysis, leading to the possible production processes

$$\mathrm{Z^0 + H \rightarrow l^+l^- + b\bar{b}}$$
$$\mathrm{W^\pm + H \rightarrow l^\pm\nu + b\bar{b}}$$

For these final states new Monte Carlo samples were produced for both the signal and the background processes. These included new matrix element calculations which significantly altered the cross sections quoted in previous studies.

For the direct comparison of different detector simulations an object oriented analysis framework has been developed in the course of this thesis. Its main purpose is to keep the analysis independent of the Monte Carlo generator and detector simulation while providing reusable and tested analysis routines flexible enough to adapt to different analysis requirements.

These demands led to an analysis package which is not restricted to Higgs search analysis but can be reused for many analysis purposes. New generator and simulation packages can easily be integrated in the framework. Furthermore experimental data can be analysed in the same way as simulated events.

For the analysis the b-tagging efficiency and jet energy calibration were changed and different aspects of the particle identification and reconstruction have been studied.

Chapter 1

Theoretical principles

1.1 The Standard Model of Particle Physics

1.1.1 Overview of the Standard Model

All known particles are either fermions or bosons [2]. A fermion has a half integer spin, a boson an integer spin. The basic constituents of matter are fermions.

Table 1.1: **Elementary fermions in the Standard Model**

Family 1	Family 2	Family 3	I_3	Q	Y
$\begin{pmatrix} \nu_e \\ e \end{pmatrix}_L$	$\begin{pmatrix} \nu_\mu \\ \mu \end{pmatrix}_L$	$\begin{pmatrix} \nu_\tau \\ \tau \end{pmatrix}_L$	$\begin{pmatrix} +1/2 \\ -1/2 \end{pmatrix}_L$	$\begin{pmatrix} 0 \\ -1 \end{pmatrix}_L$	-1
$(e)_R$	$(\mu)_R$	$(\tau)_R$	0	-1	-2
$\begin{pmatrix} u \\ d' \end{pmatrix}_L$	$\begin{pmatrix} c \\ s' \end{pmatrix}_L$	$\begin{pmatrix} t \\ b' \end{pmatrix}_L$	$\begin{pmatrix} +1/2 \\ -1/2 \end{pmatrix}_L$	$\begin{pmatrix} +2/3 \\ -1/3 \end{pmatrix}_L$	$+1/3$
$(u)_R$	$(c)_R$	$(t)_R$	0	$+2/3$	$+4/3$
$(d)_R$	$(s)_R$	$(b)_R$	0	$-1/3$	$-2/3$

The elementary fermions in the Standard Model, grouped in three families. Also listed are the third component of the weak isospin I_3, the electromagnetic charge Q and the weak hypercharge Y.

The elementary spin-$\frac{1}{2}$ fermions can be subdivided into three families (see table 1.1). Each family consists of one doublet of fermions which can interact strongly and one doublet of fermions which can only interact via the electromagnetic or the weak force. The former are called quarks, the latter leptons.

Today, four different interactions are known, the electromagnetic, the weak, the strong and the gravitational interaction. The standard model[1] provides a formalism to describe all but the gravitational interaction in one consistent model.

Each of these interactions is mediated by a particle, called a gauge boson. In the standard model eleven gauge bosons are known. They are listed in table 1.2. Within the standard model all interactions are locally gauge invariant. In the following the principle of gauge invariance is introduced[2].

Table 1.2: **Gauge bosons and interactions**

Boson	γ	$W^{\pm}$	Z^0	8 gluons
Interaction	electromagnetic	weak		strong
Effective coupling	1/137	10^{-5}		1
Mass (GeV/c^2)	0	80.43	91.19	0
Range (m)	∞	10^{-18}		$< 10^{-15}$
Q	0	± 1	0	0

Gauge bosons in the standard model. The effective coupling is a measure of the strength of the different interactions. For the strong force the range of the nuclear force is listed.

1.1.2 Non-Abelian local gauge invariance

The theoretical tool to describe particles and their interactions is quantum field theory. In quantum field theory particles are described by fields, the dynamics of interacting particles by the Lagrange density.

Without interactions the dynamics of (particle-)fields ψ are described by the Dirac Lagrange density[3]

$$\mathcal{L}_{Dirac} = \bar{\psi}(i\gamma^{\mu}\partial_{\mu} - m)\psi \tag{1.1}$$

with m the particle mass and γ^{μ} the Dirac matrices. A transformation U of ψ to a different field configuration ψ' must be unitary[4].

$$\psi \to \psi\,' = U\psi, \quad UU^{\dagger} = 1$$

The unitary transformation U has the general form

$$U(\mathbf{x}) = \exp\left(i\alpha^a(\mathbf{x})t^a\right), \quad a = 1 \ldots N^2 - 1 \tag{1.2}$$

---

[1] See standard textbooks [3, 4]

[2] See [5, 6] for details.

[3] In this section $c = \hbar = 1$ are chosen for reasons of convenience.

[4] Probability is conserved ($|\psi\,'|^2 = |\psi|^2 = 1$)

and can depend on the spacetime coordinate $\mathbf{x}$.

Here the $(\alpha^a)_{a,a}$ denote arbitrary mappings dependent on $\mathbf{x}$. If the dependence of U on the space time coordinate is omitted, the transformation is the same for every point in space and time. Here we consider the more general case that U locally changes with $\mathbf{x}$.

It is assumed that U belongs to a group of transformations with dimension N. Every member of this transformation group can be expanded in terms of a set of generators, self-adjoint[5] operators t^a.

The principle of gauge invariance states that for a given transformation group the Yang-Mills Lagrangian density [7]

$$\mathcal{L}_{Yang-Mills} = \bar{\psi}(i\gamma^\mu D_\mu - m)\psi - \frac{1}{4}(F^a_{\mu\nu})^2 \tag{1.3}$$

has to be invariant under the transformation U. Note that the first part of $\mathcal{L}_{Yang-Mills}$ resembles $\mathcal{L}_{Dirac}$ if ∂_μ is replaced by the covariant derivative D_μ. In fact $\mathcal{L}_{Yang-Mills}$ can be derived from equation (1.1) replacing ∂_μ by

$$D_\mu = \partial_\mu - igA^a_\mu t^a$$

where g is the coupling constant determining the strength of the interaction and the A^a_μ, the vector potentials which transform like

$$A^a_\mu \rightarrow A^a_\mu{}' = A^a_\mu + \frac{1}{g}\partial_\mu \alpha^a + f^{abc}A^b_\mu \alpha^c$$

define the field tensors

$$F^a_{\mu\nu}t^a = \partial_\mu A^a_\nu - \partial_\nu A^a_\mu + gf^{abc}A^b_\mu A^c_\nu$$

with f^{abc} being the total antisymmetric structure constants and g an arbitrary constant The second part of the equation, $-\frac{1}{4}(F^a_{\mu\nu})^2$, defines a gauge invariant kinetic term for the field. It does not directly derive from equation (1.1) but is added to describe the kinetics for the free field.

The field tensors transform like

$$F^a_{\mu\nu} \rightarrow F^a_{\mu\nu}{}' = F^a_{\mu\nu} - f^{abc}\alpha^b F^c_{\mu\nu}$$

If the Lagrange density $\mathcal{L}_{Yang-Mills}$ [7] is invariant under the transformation U it is said to be symmetric under this transformation. More explicitly the group of all transformations U under which the Lagrange density is symmetric is called the symmetry group of $\mathcal{L}_{Yang-Mills}$.

If a symmetry group is chosen, the field tensors can be calculated. Thus the choice of a symmetry and the principle of gauge invariance lead to an interaction, mediated by a field described by $F^a_{\mu\nu}$.

---

[5] $(t^a)^\dagger_{k,l} = (t^a)_{k,l}$

Symmetry groups are either Abelian, meaning commutative, or non-Abelian, referring to the commutation relation for the group generators, which in the general case of a non-Abelian group reads

$$[t^a, t^b] = i f^{abc} t^c$$

and equals zero for an Abelian symmetry group.

1.1.3 The $\mathbf{SU(2)_L \otimes U(1)_Y}$ model of the electroweak interaction

Electromagnetic and weak interaction can be unified to one interaction, the electroweak interaction, described by a non-Abelian theory postulated by Glashow, Salam and Weinberg [8–10].

Weak interactions violate parity[6] [11]. Only left handed particles and right handed anti-particles can interact weakly. Handedness is defined by the chiral operators

$$\mathbf{P}_L = \frac{1}{2}(1 - \gamma^5), \quad \mathbf{P}_R = \frac{1}{2}(1 + \gamma^5)$$

which select the left (right) handed part of the Dirac spinor ψ. The mass eigenzustand of a particle can be a mixture of a right handed and a left handed part, maximum parity violation is only observed for massless fermions. The handedness for all fermions is found in table 1.1, left handed particles are combined in doublets of interacting particles, right handed particles are arranged in singlets.

The symmetry group in the GSW-theory is given by

$$SU(2)_L \otimes U(1)_Y$$

and describes the electroweak interaction of massless fermions. The subscript L denotes parity violation while the subscript Y is the weak hypercharge. It is important to notice that the $U(1)_Y$ part of the symmetry group is not equal to the $U(1)_{QED}$ group of QED[7].

The generator for the $U(1)_Y$ group is $\frac{1}{2}Y$, for $SU(2)_L$ the generators are the three Pauli matrices $\frac{1}{2}\tau^a$, written as $\vec{\tau}$. The covariant derivative becomes

$$D_\mu = \partial_\mu + i\frac{g'}{2}B_\mu Y + i\frac{g}{2}W_\mu^a \tau^a \tag{1.4}$$

with g, g' the electroweak coupling constants, B_μ the vector potential associated with the weak hypercharge and W_μ^a the vector potentials related to the Pauli matrices. The $U(1)_Y$ group is Abelian while $SU(2)_L$ is not, thus the field tensors can be written as

$$\begin{aligned} B_{\mu\nu} &= \partial_\mu B_\nu - \partial_\nu B_\mu \\ W_{\mu\nu}^a &= \partial_\mu W_\nu^a - \partial_\nu W_\mu^a - g\epsilon^{abc} W_\mu^b W_\nu^c \end{aligned}$$

---

[6] The parity operator $\mathbf{P}$ is defined by $\mathbf{Pr} \to -\mathbf{r}$

[7] QED: quantum electro dynamics, Abelian gauge theory of the electromagnetic interaction [12].

The Lagrange density in the electroweak theory can be written as

$$\mathcal{L}_{GSW} = i\sum f\bar{\psi}_f\gamma^\mu D_\mu\psi_f - \frac{1}{4}(B_{\mu\nu}B^{\mu\nu} + W^a_{\mu\nu}W^{a,\mu\nu})$$

with the sum over all fermions f.

The bosons corresponding to the vector potentials – called vector or gauge bosons – are massless, but experiments show that the weak interaction has a finite range and therefore the gauge bosons are not massless (see table 1.2). A solution to this problem is the Higgs mechanism explained in section 1.1.5.

1.1.4 The SU(3)$_\mathrm{C}$ model of the strong interaction

The strong interaction is described by the non-Abelian symmetry group $SU(3)_C$ where C refers to the colour charge. There are three colour charges denoted red, green and blue. The gauge theory of strong interactions [13] is often referred to as quantum-chromo-dynamics, or QCD.

The bosons mediating the strong interactions are called gluons, which themselves carry a colour charge. Eight[8] gluons corresponding to eight generators λ_a, the Gell-Mann matrices. In this case the covariant derivative is

$$D_\mu = \partial_\mu + i\frac{g_s}{2}G^a_\mu\lambda_a$$

and the field tensors for the gluons fields are given by

$$F^a_{\mu\nu} = \partial_\mu G^a_\nu - \partial_\nu G^a_\mu - g_s f^{abc}G^a_\mu G^b_\nu$$

The self-interaction of the gluons limits the range of the strong interaction. No free colour charge was observed, neither any free quarks or gluons.

Confinement and asymptotic freedom

The strong interaction grows in strength for greater distances. If the distance between two quarks grows, the energy density increases. In this regime so called lattice calculations have to be adopted instead of standard perturbation techniques.

When the energy density reaches the threshold for pair production, quark-anti-quark pairs are produced spontaneously. If the whole system of quarks, called hadron, did not have a colour charge in the beginning, the pair production of quarks will not alter this. Hence, no free colour charge can be observed. This mechanism is called confinement.

At small distances two effects shield the colour charge of particles in the interaction. The first is the vacuum polarisation, in which virtual quark-anti-quark pairs contribute to the effective quark colour charge. The second is gluon colour change. If a quark approaches another quark of the same colour, one of

---

[8] $SU(3) \rightarrow det(U) = +1$ [4]

them is likely to emit a gluon, thereby changing its colour. The latter effect dominates.

Thus at small distances the strong interaction vanishes. This is called asymptotic freedom.

1.1.5 The Standard Model Higgs Mechanism

Goldstone Bosons in non-Abelian gauge theories

The gauge bosons regarded in section 1.1.2 were massless. The Higgs mechanism [14–17] gives a mass to these bosons by introducing scalar fields ϕ, here denoted by multiplets of real valued fields ϕ_i, which are invariant under the transformation

$$\phi_i(\mathbf{x}) \to \phi_i'(\mathbf{x}) = (1 + i\alpha^a(\mathbf{x})t^a)_{ij}\phi_j(\mathbf{x}) = (1 + \alpha^a(\mathbf{x})T^a)_{ij}\phi_j(\mathbf{x}), \quad T^a = it^a$$

where the t^a are the generators of the symmetry group considered. The particles associated to the scalar fields ϕ_i are called Goldstone bosons. The potential $V(\phi)$, the Higgs potential, describes the self interaction of the Goldstone bosons.

At a minimum of the potential the fields have a vacuum expectation value

$$\langle \phi_i \rangle_{min} = (\phi_0)_i$$

Two cases have to be considered. In the first case a transformation T^k leaves the vacuum state ϕ_0 of the scalar field invariant

$$\phi_0' = (1 + \alpha^k(\mathbf{x})T^k)\phi_0 = \phi_0$$

Since $\alpha^k(\mathbf{x})$ is arbitrary, this requires $T^k\phi_0 = 0$ for the chosen generator. In the second case the vacuum state is not invariant for a particular generator $T^{\,l}$ and one finds

$$T^{\,l}\phi_0 \neq 0$$

If the vacuum expectation value of one of the fields ϕ_i is not gauge invariant, it is not symmetric with respect to the selected symmetry group.

The Lagrange density including the Higgs potential and the kinematic terms for the Goldstone boson fields can be written as

$$\mathcal{L}_{Higgs} = \frac{1}{2}(D_\mu\phi)^2 - V(\phi) \tag{1.5}$$

with the covariant derivative

$$D_\mu\phi_i = \partial\phi_i + gA_\mu^a T_{ij}^a \phi_j$$

Expanding the scalar fields about the vacuum expectation value by writing

$$\phi_i(\mathbf{x}) = (\phi_0)_i + \chi_i(\mathbf{x})$$

mass terms for both the gauge bosons, given by

$$m_{ab}^2 = g^2 (T_{ij}^a (\phi_0)_j)(T_{ij}^b (\phi_0)_j)$$

and for the Goldstone bosons arise from equation (1.5) [6]. This will be demonstrated for the case of the electroweak theory.

Symmetry breaking in the Electroweak Theory

In the case of the $SU(2)_L \otimes U(1)_Y$ symmetry group the introduction of a doublet of complex fields[9]

$$\phi(\mathbf{x}) = \begin{pmatrix} \phi^+(\mathbf{x}) \\ \phi^0(\mathbf{x}) \end{pmatrix} = \begin{pmatrix} \phi_1^+(\mathbf{x}) + i\phi_2^+(\mathbf{x}) \\ \phi_1^0(\mathbf{x}) + i\phi_2^0(\mathbf{x}) \end{pmatrix}$$

and a Higgs potential, the so called Mexican hat potential,

$$V(\phi) = -\mu^2 \phi^\dagger \phi + \lambda(\phi^\dagger \phi)^2, \quad \mu^2, \lambda > 0$$

suffices to give masses to the gauge bosons of the electroweak interaction. This form of the Higgs potential constrains the vacuum state of the Higgs scalar field to be unsymmetric with respect to the generators of the gauge group.

The form of the potential can evolve with time so that the vacuum state can become gauge invariant. The change from a symmetric to an unsymmetric vacuum state is called spontaneous symmetry breaking.

The ϕ^+ component is called the charged component and ϕ^0 the neutral component. The vacuum expectation value can be written as

$$\langle \phi \rangle_{min} = \frac{1}{\sqrt{2}} \begin{pmatrix} 0 \\ v \end{pmatrix}, \quad v = \sqrt{\frac{\mu^2}{\lambda}}$$

where the charged component is set to zero because the vacuum is uncharged. This particular selection is possible because all the solutions ϕ_0 minimizing the potential are equivalent and a particular choice can only be justified by physical arguments.

The expansion of ϕ about the vacuum expectation value can be parameterized by

$$\phi(\mathbf{x}) = \exp i\vec{\xi}(\mathbf{x})\vec{\tau} \frac{1}{\sqrt{2}} \begin{pmatrix} 0 \\ v + \eta(\mathbf{x}) \end{pmatrix}$$

with four different degrees of freedom given by $\vec{\xi} = (\xi_1, \xi_2, \xi_3)$ and η. These can be identified with four Goldstone bosons. The three degrees of freedom associated with $\vec{\xi}$ can be removed by a gauge transformation[10] and become the new degrees of freedom of the massive gauge bosons.

---

[9] ϕ_i^+, ϕ_i^0 are the real valued fields ϕ_i used in the last section.

[10] the so called R_ξ gauge

The remaining degree of freedom cannot be removed by a gauge transformation. It is a new, massive particle, the Higgs boson with the mass $m_{Higgs} = \sqrt{2}\mu^2$.

Taking the covariant derivative (1.4) for the electroweak theory and leaving out the terms describing the interaction of the gauge bosons with the Higgs boson one obtains

$$\begin{aligned}(D^\mu\phi)^\dagger(D_\mu\phi) =& (\partial^\mu\eta)^\dagger(\partial_\mu\eta) + \frac{v^2g^2}{8}(W_1^\mu - iW_2^\mu)(W_{1\mu} - iW_{2\mu}) \\ &+ \frac{v^2}{8}(W_{3\mu}^\dagger, B_\mu^\dagger)\begin{pmatrix} g^2 & -gg' \\ -gg' & g'^2 \end{pmatrix}\begin{pmatrix} W^{3\mu} \\ B^\mu \end{pmatrix}\end{aligned}$$

The diagonalisation of the mass matrix is achieved by a rotation which transforms the vector potentials W_3^μ and B^μ like

$$\begin{pmatrix} Z_\mu \\ A_\mu \end{pmatrix} = \begin{pmatrix} \cos\theta_W & -\sin\theta_W \\ \sin\theta_W & \cos\theta_W \end{pmatrix}\begin{pmatrix} W_\mu^3 \\ B_\mu \end{pmatrix}$$

where the angle θ_W, the Weinberg angle, is defined by

$$\cos\theta_W = \frac{g}{\sqrt{g'^2 + g^2}}, \quad \sin\theta_W = \frac{g'}{\sqrt{g'^2 + g^2}}$$

This finally leads to three massive and one massless gauge boson. One can identify these bosons with the particles observed in electromagnetic and weak interactions. The four gauge bosons are listed in table 1.3. The massless gauge boson A^μ can be identified with the Photon. Then the electromagnetic coupling constant is given by

Table 1.3: **Electroweak gauge bosons and their masses**

$W^\pm$	Z^0	A^μ
$\frac{1}{\sqrt{2}}(W_1^\mu \mp iW_2^\mu)$ $m_{W^\pm} = g\frac{v}{2}$	$\cos\theta_W W_\mu^3 - \sin\theta_W B_\mu$ $m_{Z^0} = \sqrt{g^2 + g'^2}\frac{v}{2}$	$\sin\theta_W W_\mu^3 + \cos\theta_W B_\mu$ $m_{A^\mu} = 0$

$$e = g\sin\theta_W = g'\cos\theta_W$$

and the electric charge quantum number Q can be related to the weak isospin I and the weak hypercharge Y by the Gell-Mann-Nishijima relation

$$Q = I_3 + \frac{Y}{2}$$

The Higgs mechanism directly leads to mass terms for the gauge bosons. From low energy phenomena one can relate the mass of the $W^\pm$-boson to the Fermi constant G_F which gives the vacuum expectation value

$$v^2 = \frac{1}{\sqrt{2}G_F} \backsimeq (246\text{GeV})^2$$

but does not determine the mass of the Higgs-boson.

Fermion masses and the Higgs mechanism

Unlike the gauge bosons the fermions do not directly acquire mass via the Higgs mechanism. Instead it is assumed that the strength of the Higgs boson field coupling to the fermion fields, the Yukawa coupling, is proportional to the fermion mass m_f

$$\mathcal{L}_{Yukawa} = -m_f \bar{f} f \left(1 + \frac{\eta}{v}\right), \quad f = f_L + f_R \tag{1.6}$$

All left (f_L) and right (f_R) handed massive fermions couple to the Higgs boson, the observation of neutrino oscillations [18] hints that neutrinos might as well have a mass and might as well couple to the Higgs boson.

The mass eigenstates of quarks are not the eigenstates of the weak interaction, but a mixture of these. As a consequence the weak interaction can induce flavour changes via neutral current interactions[11].

The (primed) eigenstates of the weak interaction are related to the mass eigenstates by the Cabbibo-Kobayashi-Maskawa matrix V_{CKM} [20]

$$\begin{pmatrix} d\,' \\ s\,' \\ b\,' \end{pmatrix} = V_{CKM} \cdot \begin{pmatrix} d \\ s \\ b \end{pmatrix}$$

Constraints to the mass range for Standard Model Higgs boson

In 2000 the LEP collider was shut down after eleven successful years of operation. New constraints were set to the range of Higgs masses which rule out the existence of a Standard Model Higgs boson with a mass lighter than 114.1 GeV/c^2 [1] at a confidence level of 95%.

The LEP results also showed an indication of a Higgs boson with a mass of 115.6 GeV/c^2 but no claim for an observation could be made.

A restrictive upper bound of about 1 TeV to the Higgs mass is set by the Higgs self coupling which leads to probability amplitudes greater than unity in radiative corrections to propagators which contain the Higgs boson [21].

Conclusion

The Standard Model describes the electroweak and the strong interaction in a local gauge theory based on the symmetry group

$$SU(3)_C \otimes SU(2)_L \otimes U(1)_Y$$

with the Lagrange density

$$\mathcal{L}_{SM} = \mathcal{L}_{Yang-Mills} + \mathcal{L}_{Yukawa} + \mathcal{L}_{Higgs}$$

which includes a single uncharged scalar Higgs boson as well as massive gauge bosons and fermions interacting with it.

---

[11] Which are suppressed by the GIM-mechanism [19]

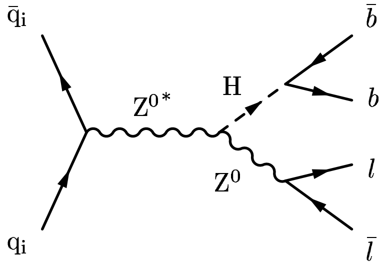

Figure 1.1: *Leading order Feynman diagram for the process* $q_i\bar{q}_i \rightarrow Z^0 H$*, including decay channels*

1.2 Signals for associated Higgs production

1.2.1 Associated Production of a Standard Model Higgs boson with a Z^0 Vector Boson

Production mechanism for Z^0H at Hadron Colliders

The associated production of a Higgs boson with a gauge boson is also referred to as Higgs bremsstrahlung. An off-shell electroweak gauge boson radiates a massive Higgs boson, resulting in a state with one massive Higgs boson and one massive on-shell gauge boson (see figure 1.1)

The total cross section [22, 23]

$$\sigma(\mathrm{q_i\bar{q}_i} \rightarrow \mathrm{Z^0H} + X) = \frac{\pi\alpha^2(L_i^2 + R_i^2)}{72\sin^2\theta_W(1-\sin\theta_W)} \cdot \frac{2|\vec{p}_f|}{\sqrt{\hat{s}}} \cdot \frac{(|\vec{p}_f|^2 + 3m_{\mathrm{Z^0}}^2)}{(\hat{s} - m_{\mathrm{Z^0}}^2)^2}$$

depends on the center of mass energy $\hat{s}$ in the $q_i\bar{q}_j$ system – related to the full center of mass energy s of the hadron collider by the fractions $x_{i,j}$ of s each quark is carrying[12], on the electromagnetic charge e_i of each quark – and on the final momentum of the outgoing $\mathrm{W}^{\pm}$ and the Higgs boson $\vec{p}_f$ in the center of mass frame given by

$$\hat{s} = x_i x_j s, \quad |\mathbf{p_f}|^2 = \frac{s}{4\sqrt{2}} \cdot \frac{m_{Higgs}}{v^2}$$

The chiral couplings of the weak neutral current are defined as

$$L_i = I_3 + R_i, \quad R_i = -2e_i\sin\theta_W$$

Decay modes for Z^0H

The dominant decay mode for the Standard Model Higgs boson with a mass less than $2m_{\mathrm{W}^{\pm}}$ is $\mathrm{H} \rightarrow \mathrm{b\bar{b}}$, because the strength of the Higgs-fermion coupling is

---

[12] See also section 2.1

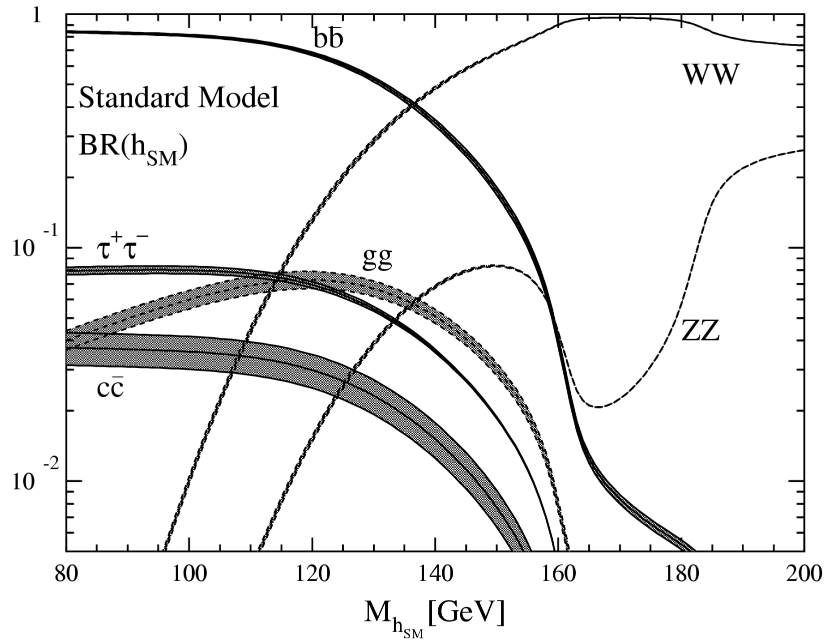

Figure 1.2: *Branching ratios of the different Higgs boson decay channels* (figure taken from [24])

proportional to the fermion mass (see equation (1.6) on page 25) which leads to the partial width [22]

$$\Gamma(\mathrm{H} \to f\bar{f}) = \frac{3G_F}{4\pi\sqrt{2}} \cdot m_{\mathrm{H}} \cdot m_f^2 \cdot \left(1 - \frac{4m_f^2}{m_{\mathrm{H}}^2}\right)^{\frac{3}{2}} \tag{1.7}$$

The Higgs boson decays in the heaviest fermions accessible, see figure 1.2 [24]. For higher Higgs masses the width broadens because more decay channels become accessible.

Since the Higgs boson is a scalar particle the decay does not show a dependency on the polar[13] angle θ.

The two body decay of the Higgs boson is described by the Breit Wigner form for the decay amplitude A which depends on the invariant mass $m_{\mathrm{b\bar{b}}}$ of the two bottom quarks

$$A(m_{\mathrm{b\bar{b}}}) = \frac{-m\Gamma_{el}}{m_{\mathrm{b\bar{b}}} - m_{Higgs}^2 + im_{Higgs}\Gamma_{tot}}$$

with the total width Γ_{tot} and the elastic width Γ_{el} of the Higgs boson.

The leptonic decay of the Z^0 boson to two charged leptons – see figure 1.1 – is considered in this thesis, the hadronic decay modes are not taken into account

---

[13] with respect to the z-Axis defined by the beam

since the resulting final state would include four jets indistinguishable from the QCD background.

As for the Higgs boson the mass of the Z^0 boson is given by the invariant mass of its decay products. The main difference to the Higgs decay is the better mass resolution achievable for the two lepton final state.

Since the Z^0 has spin 1, the differential cross section depends on θ

$$\frac{d\sigma}{d\Omega} \propto (1 + \cos^2\theta)$$

Another decay mode with the Z^0 boson decaying to two neutrinos is considered to be of interest [25] but is not studied in this thesis.

Table 4.2 on page 73 lists the branching ratios for the Z^0 boson leptonic decay channels $Z^0 \to l^+l^-$.

The complete final state for the Z^0H signal considered in this thesis is given by

$$Z^0 + H \to l^+l^- + b\bar{b} + X, \quad l = e, \mu, \tau$$

characterized by two opposite-sign, same-flavour (OSSF) leptons and two b-jets and will be referred to as $l^+l^-b\bar{b}$.

1.2.2 Associated Production of a Standard Model Higgs boson with a W± Vector Boson

Production mechanism for $W^\pm H$ at Hadron Colliders

The production mechanism for $q_i\bar{q}_j \to W^\pm H$ is similar to that of associated production of a Higgs boson with a Z^0 boson (see figure 1.3 on the facing page), the off-shell Z^0 boson is simply replaced by an off-shell $W^\pm$ boson.

The total cross section for the process $q_i\bar{q}_j \to W^\pm H$ at hadron colliders [21–23]

$$\sigma(q_i\bar{q}_j \to W^\pm H + X) = \frac{\pi\alpha^2}{36\sin^2\theta_W}\,|(V_{CKM})_{ij}|^2 \cdot \frac{2|\mathbf{p_f}|}{\sqrt{\hat{s}}} \cdot \frac{(|\mathbf{p_f}|^2 + 3m^2_{W^\pm})}{(\hat{s} - m^2_{W^\pm})^2}$$

The associated production of a Higgs boson with a gauge boson is not the dominant production mode at the TEVATRON. The cross section for the production of a single Higgs boson via gluon fusion – $gg \to H$ – is about and order of magnitude higher, but the final state given by two b-jets can hardly be distinguished from background QCD processes [25].

Additional particles, mainly leptons, coming from the leptonic gauge boson decay, can help identify a signal event. One can conclude that a decision in favour of associated Higgs production is not based on the production cross section but on the event signature, which is easier to distinguish from the great amount of QCD background processes leading to a final state including two bottom quarks.

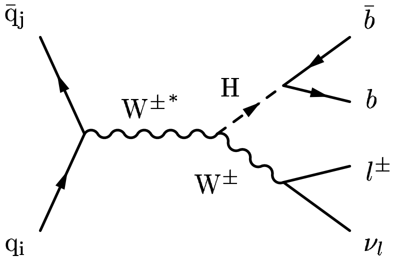

Figure 1.3: *Leading order Feynman diagram for the process* $q_i\bar{q}_j \to W^{\pm}H$*, including decay channels*

Decay modes for $\mathbf{W^{\pm}H}$

The $W^{\pm}$ boson can decay into two leptons. For this decay mode the final state consists of a charged lepton and a neutrino. This decay channel is chosen because an isolated charged light lepton, an electron or a muon, can serve as an indication for a signal event[14]. Table 4.2 on page 73 lists the branching ratios for the $W^{\pm}$ boson leptonic decay channels $W^{\pm} \to l^{\pm}\nu$. The complete final state – which will be referred to as $l^{\pm}\nu b\bar{b}$ – studied in this thesis is

$$W^{\pm} + H \to l^{\pm}\nu + b\bar{b} + X, \quad l = e, \mu, \tau$$

with two b-jets, one charged lepton and missing energy from the neutrino. The Feynman diagram including the decay channels is shown in figure 1.3.

1.3 Backgrounds to the associated Higgs production

Background processes to the signals can be divided in continuous and resonant background processes. The background processes are labelled by the intermediate states characterizing the physical background process.

For events originating from a continuous background process the invariant mass spectrum of the two b-jets does not show a peak caused by the two-body decay of a single particle.

In a resonant background process the two b-jets come from the decay of a single particle and therefore their invariant mass gives a resonance peak in the spectrum. In the following text the background processes will be labeled by the intermediate states characterizing each process.

1.3.1 Continuous backgrounds to the associated Higgs production

The $\mathbf{b\bar{b}}$ background

The $b\bar{b}$ background originates from two different production mechanisms.

---

[14] The channel $W^{\pm} + H \to 4jets$ is not believed to be distinguishable from background processes at hadron colliders [25].

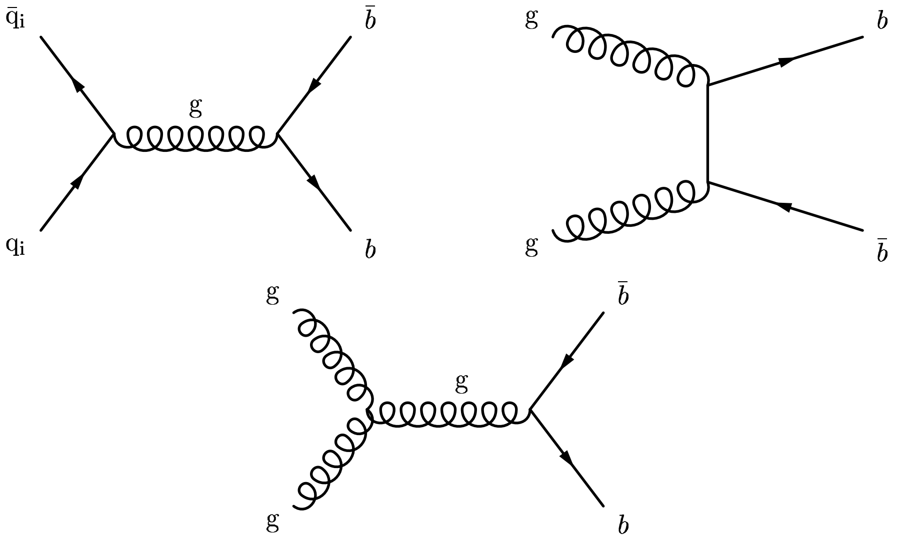

Figure 1.4: *Leading order Feynman diagrams for the processes* $q_i\bar{q}_i \rightarrow b\bar{b}$ *and* $gg \rightarrow b\bar{b}$

The first process is the direct annihilation of two quarks to a gluon which then splits to two bottom quarks (see figure 1.4)

$$q_i\bar{q}_i \rightarrow b\bar{b}$$

In the second process two gluons split to form a final state with two bottom quarks

$$gg \rightarrow b\bar{b}$$

In both cases the final state includes only two b-quarks and no charged leptons. Additional leptons occur in reconstructed events if a lepton belonging to a b-jet which originates from the hadronization of the bottom quark is falsely identified as being isolated (see section 3.4.2 on page 67 on isolation criteria) from the jet.

If only one lepton is misidentified as isolated the final state resembles the final state of the signal $\mathrm{W}^{\pm}\mathrm{H}$. If two isolated leptons are found the $\mathrm{b\bar{b}}$ background results in a final state similar to that of the signal $\mathrm{Z}^0\mathrm{H}$.

The single top quark background

A single top quark together with a bottom quark can be produced via two processes (see figure 1.5 on the facing page).

First an off-shell $\mathrm{W}^{\pm}$ boson can decay into a top quark and a bottom quark

$$q_i\bar{q}_j \rightarrow \mathrm{W}^{\pm *} \rightarrow \mathrm{tb}$$

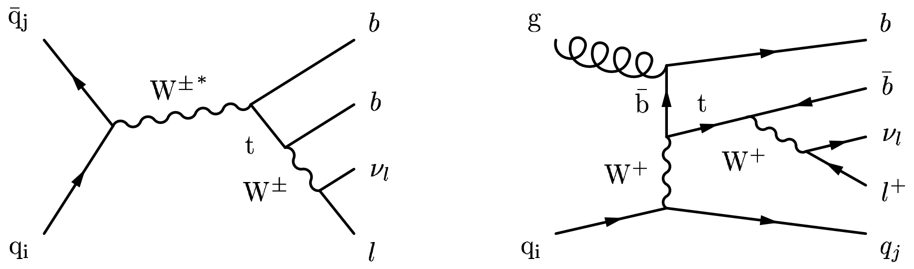

Figure 1.5: *Leading order Feynman diagrams for single top production, including decay channels*

if the center of mass energy of the quark-anti-quark pair, $\hat{s}$, is bigger than the sum of the top quark mass and the bottom quark mass.

Second a top quark can be produced in a so called $\mathrm{W}^{\pm}$ gluon fusion process which leads to a final state with an additional quark

$$q_i\bar{q}_j \to tqb$$

The final state is characterized by a single bottom quark and a top quark decaying into a $\mathrm{W}^{\pm}$ boson and a second bottom quark. If the $\mathrm{W}^{\pm}$ decays into two leptons, the final state is a background to the $\mathrm{W}^{\pm}\mathrm{H}$ signal.

$$t + b\,(+q) \to \mathrm{W}^{\pm}b + b\,(+q) \to \mathrm{l}^{\pm}\nu b + b\,(+q), \quad l = e,\mu,\tau$$

The $\mathrm{t\bar{t}}$ background

The background process with two top quarks as intermediate states is produced similar to the $\mathrm{b\bar{b}}$ process.

For $\mathrm{t\bar{t}}$ to serve as a background process two b-jets in the final state are required plus at least one additional lepton. If both top quarks decay to a $\mathrm{W}^{\pm}$ boson and a bottom quark one finds

$$t + \bar{t} \to W^{+}b + W^{-}\bar{b}$$

The detection of two leptons leads to a background signal to the process $\mathrm{Z}^{0}\mathrm{H}$

$$W^{+}b + W^{-}\bar{b} \to l^{+}\nu_l b + l^{-}\bar{\nu}_l\bar{b}, \quad l = e,\mu,\tau$$

as can be seen on the left hand side of figure 1.6.

In the case of one detected lepton, if one $\mathrm{W}^{\pm}$boson decays hadronically or one lepton is not detected, the process has a signature similar to the process $\mathrm{W}^{\pm}\mathrm{H}$

$$W^{+}b + W^{-}\bar{b} \to l\nu_l b + q_i\bar{q}_j\bar{b}, \quad l = e,\mu,\tau$$

depicted on the right hand side of figure 1.6.

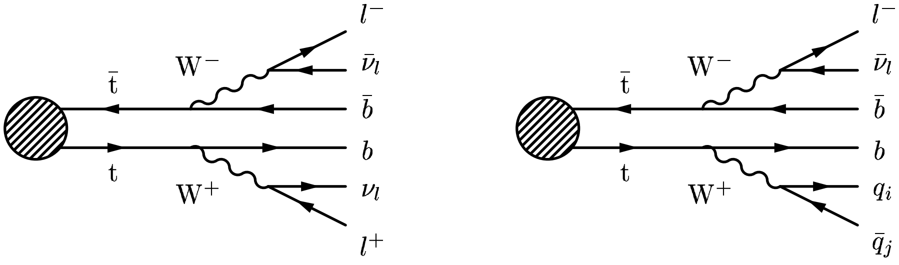

Figure 1.6: *Leading order Feynman diagrams for the $t\bar{t}$ final states.*

The W$^\pm$b$\bar{\text{b}}$ background

In the case of the W$^\pm$b$\bar{\text{b}}$ background process the two bottom quarks are created by a gluon splitting into a bottom quark-anti-quark pair (see figure 1.7 on the next page). The W$^\pm$ boson comes from a charged current induced flavour change of a quark.

$$q_i\bar{q}_j \to \mathrm{W}^\pm + g$$

The final state resembles that of W$^\pm$H process

$$\mathrm{W}^\pm + g \to \mathrm{l}^\pm\nu + \mathrm{b}\bar{\mathrm{b}}, \quad l = e, \mu, \tau$$

The Z^{0}b$\bar{\text{b}}$ background

Like the W$^\pm$b$\bar{\text{b}}$ background process the two bottom quarks in the Z^{0}b$\bar{\text{b}}$ process originate in a gluon splitting (see figure 1.7 on the facing page), but the Z^0 boson is radiated by a quark. Although the process is labelled Z^{0}b$\bar{\text{b}}$ the Z^0 boson can be replaced by an off-shell photon, so the production process can be written as

$$q_i\bar{q}_i \to \mathrm{Z}^0/\gamma^* + g$$

The photon or the gauge boson decay to a pair of charged OSSF leptons. Thus the process Z^{0}b$\bar{\text{b}}$ must be taken into account as a background process to Z^{0}H.

1.3.2 Resonant backgrounds to the associated Higgs production

A Z^0 boson can mimic a H boson if it decays to a bottom quark-anti-quark pair. In this case a peak in the invariant mass spectrum of the b-jets at the Z^0 boson mass $m_{\mathrm{Z}^0} = 91.19\ \mathrm{GeV/c}^2$ is found.

The width of the resonance peak is mostly determined by the jet energy resolution of the detector and not by the natural line width. If the width of the resonance peak becomes bigger than the difference of the Higgs to the Z^0 mass the separation of signal and resonant background becomes difficult.

Another physical difference between the Z^0 boson and the Higgs boson is the spin which leads to a different angular distribution of the bottom quarks in the decay[15].

---

[15] See section 1.2.1

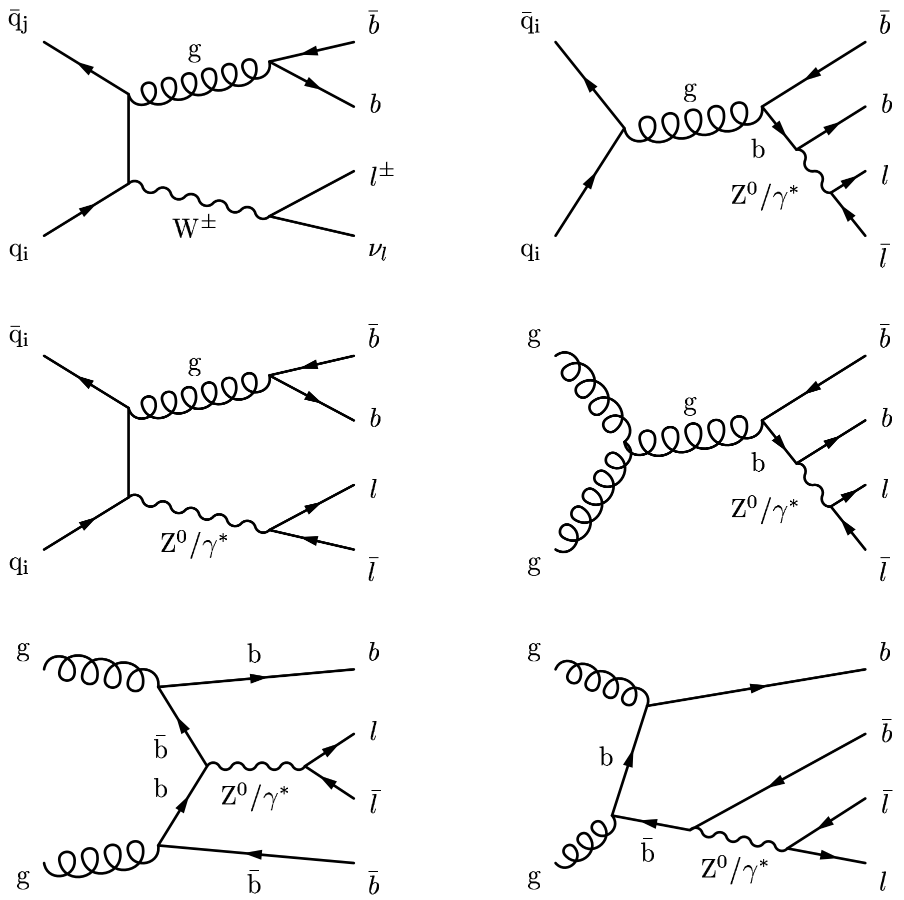

Figure 1.7: *Leading order Feynman diagrams for the $W^{\pm}b\bar{b}$ and $Z^0b\bar{b}$ final states.*

The $\mathbf{W^{\pm}Z^0}$ background

The resonant background process $W^{\pm}Z^0$ is produced by

$$q_i\bar{q}_j \rightarrow W^{\pm}Z^0$$

with an on-shell $W^{\pm}$ and an on-shell Z^0 as the intermediate state (see figure 1.8 on the next page). The final state is similar to the final state for the $W^{\pm}H$ signal

$$W^{\pm} + Z^0 \rightarrow l^{\pm}\nu + b\bar{b}$$

The $\mathbf{Z^0Z^0}$ background

At lowest order two processes seen in figure 1.8 on the following page govern the production of two on-shell Z^0 bosons

$$q_i\bar{q}_i \rightarrow Z^0Z^0$$

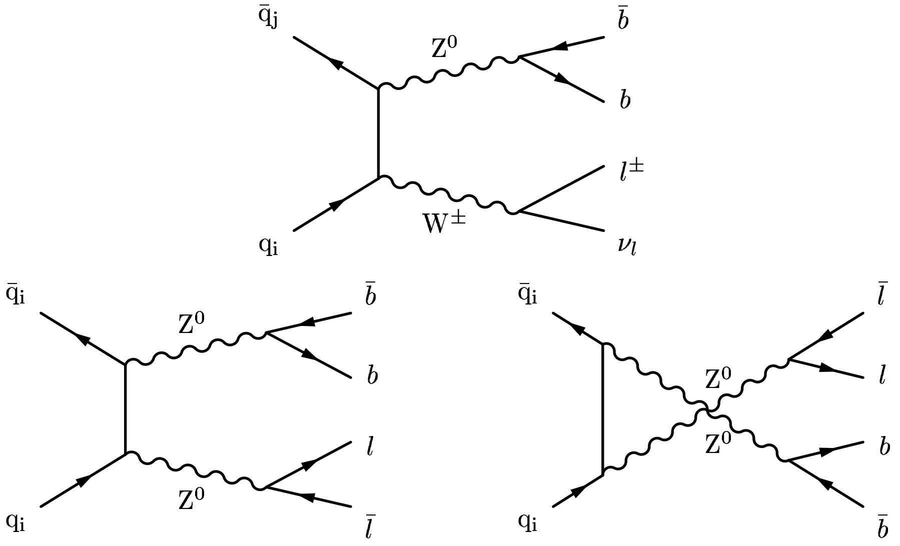

Figure 1.8: *Leading order Feynman diagrams for the resonant backgrounds, including decay channels*

as the intermediate state. If one of the two Z^0 bosons decays into a bottom quark-anti-quark pair and the other to two charged leptons the final state resembles the final state for the Z^0H signal

$$Z^0 + Z^0 \rightarrow l^+l^- + b\bar{b}$$

Chapter 2

Hadron Colliders - Tevatron and LHC

2.1 An introduction to Hadron Colliders Physics

2.1.1 Parton distribution functions

Hadrons are colourless objects. Since the fundamental constituents of hadrons carry colour charge, a hadron has to be composed of more than one of these constituents[1].

The event signatures seen in hadronic collisions are greatly influenced by the fact that hadrons are composite particles. Although the focus is placed on pp and p$\bar{\text{p}}$ colliders, some of characteristics of hadronic collisions described below can be applied to other machines such as electron-proton colliders.

Hadronic collisions interpreted as collisions of their constituents

To simplify the terminology in the subsequent text the proton is taken as an example of a hadron.

In the parton model [26] the proton is assumed to consist of non-interacting partons, each of which carrying only a part of the total proton momentum P. With x_i denoting the fraction of P carried by parton i, the x_i have to satisfy both

$$0 \leqslant x_i \leqslant 1 \quad \text{and} \quad \sum_i x_i = 1 \quad \text{and therefore} \quad \sum_i x_i P = P \tag{2.1}$$

Although the proton is in reality a bound state the assumption of non-interacting partons inside the proton shall be made[2].

---

[1] see 1.1.4 for details on colour charge and the hadron's constituents.

[2] identifying the partons with quarks this can be justified by taking into account asymptotic freedom of the quarks at high Q^2 and short interaction times (see ??)

Then the differential cross section $d\sigma$ for a general interaction of two protons A and B leading to a final state denoted by X and Y can be written as

$$d\sigma(A + B \to X + Y) = \sum_{ij} f_i^A(x_A) f_j^B(x_B) d\hat{\sigma}(i + j \to X + Y)$$

where f_j^B is the number distribution of partons of species j in proton B and the sum is taken for all parton configurations resulting in the final state observed. The cross section of the full hadronic collision depends on the elementary cross section for the parton-parton process denoted by $\hat{\sigma}$.

Since $\hat{\sigma}$ can be calculated, measurements of the cross section σ give information on the parton number distribution functions f.

Q^2 dependent parton distribution functions

Leaving behind the assumption of free constituents the proton model becomes more complex. The distribution functions f become dependent on q^2_{Parton}, the squared momentum transfer between the interacting partons. In this form f is called a parton distribution function.

$$f(x) \to f(x, q^2_{Parton}) \tag{2.2}$$

This momentum transfer is not accessible directly since the final constituents are not existing as free particles[3]. The resulting hadronic state (X, Y) is again a state of bound partons with unknown dynamics. To overcome this problem the nucleon structure has been probed using electrons and neutrinos in deep inelastic scattering reactions.

For the evaluation of $f(x, q^2_{Parton})$ the unknown momentum transfer q^2_{Parton} has to be set to a value Q^2 in the order of the invariant mass of the partons i and j [22].

Deep inelastic electron-nucleon scattering

Probing the structure of a nucleon N with an electron e results in a clear final state characterized by the scattering angle and energy of the outgoing electron.

The scattering cross section can be calculated knowing the initial $(\mathbf{p}_i)$ and final four-vector momentum $\mathbf{p}_f$ of the electron in the inelastic reaction

$$e(\mathbf{p}_i) + N(\mathbf{P}_i) \to e(\mathbf{p}_f) + X$$

In this picture the photon γ mediates the interaction of the electron with the nucleon's constituents. This allows the determination of the charge of the partons involved.

---

[3] see quark confinement described in **??**

The final hadronic state X can consist of several particles, thus the dynamics do not give the same constraints on the masses of the final particles as in the case of elastic scattering. If

$$\mathbf{p}_i = (E_i, \vec{p}_i), \quad \mathbf{p}_f = (E_f, \vec{p}_f)$$

denote the initial and final electron momentum four vectors, with energy and momentum given in the laboratory frame, then the squared momentum transfer Q^2 and the energy loss ν of the electron (the energy of the exchanged Photon γ) can be written as

$$Q^2 = -\mathbf{q}^2 = -(\mathbf{p}_i - \mathbf{p}_f)^2, \quad \nu = \frac{\mathbf{P}_i \cdot \mathbf{q}}{M} = E_i - E_f \tag{2.3}$$

The differential cross section $\sigma_{e+N \to e+X}$ for deep inelastic electron-nucleon scattering is found to be proportional to $\tan^2(\theta/2)$, θ being the scattering angle of the electron in the laboratory frame, and can be expressed in terms of two[4] nucleon structure functions $W_1(q^2, \nu)$ and $W_2(q^2, \nu)$.

The $\tan^2(\theta/2)$ dependency is a consequence of the scatterer being a point-like spin-$\frac{1}{2}$ fermion.

Quarks and partons

Introducing the scaling variable x,

$$x = \frac{Q^2}{2M\nu} = \frac{Q^2}{2M(E_i - E_f)}, \tag{2.4}$$

Bjorken [27] anticipated the nucleon structure functions to be independent of Q^2 in the case of

$$Q^2, \nu \to \infty \quad \text{for fixed} \quad x$$
$$W_1(q^2, \nu) \to F_1(x) \quad \text{and} \quad \frac{\nu}{M} W_2(q^2, \nu) \to F_2(x)$$

by adopting the quark-algebra introduced by Gell-Mann [28] and Zweig [29, 30]. For all fixed positive values of x F_1 and F_2 are finite and non-zero. This was confirmed experimentally at SLAC [31].

Using the de-Broglie wavelength $\lambda_{ep} = h/\sqrt{Q^2}$ corresponding to the momentum transfer Q^2 as a measure for the resolution achieved in the scattering and $\tau_{ep} = \hbar/\nu = (2\hbar M x)/Q^2$ as a rough approximation to the duration of the electron-parton interaction, we can state that with higher Q^2 the nucleon structure is probed to smaller distances and the electron-parton interaction time is becoming shorter.

Scattering at high Q^2 therefore implies that partons have to be point-like objects and the interaction of the partons (which happens on a time scale $\tau_{parton} \approx \hbar/M_X \gg \tau_{ep}$) can be neglected during the scattering.

---

[4] accounting for the magnetic and electric properties of the scatterer

Referring to equation (2.1) for an on-shell parton j with mass $m_j = x_j M$ one finds

$$\begin{aligned} m_j^2 &= (\mathbf{q} + x_j\mathbf{P})^2 = q^2 + 2x_j\mathbf{P}\cdot\mathbf{q} + (x_j\mathbf{P})^2 = q^2 + 2x_jM\nu + m_j^2 \\ \Rightarrow x_j &= -\frac{q^2}{2M\nu} = x \end{aligned}$$

The scaling variable x can be identified by the fraction of the total nucleon momentum the parton is carrying. For spin-$\frac{1}{2}$ fermions this leads to the Callan-Gross relation[5]

$$2xF_1(x) = F_2(x)$$

The experimental verification of Bjorken scaling and the Callan-Gross Relation strongly suggest partons to be identified by almost free, point-like, spin-$\frac{1}{2}$ fermions – quarks.

Quarks as constituents of hadrons

In the case of the nucleon, three contributions to the structure functions have to be taken into account: valence quarks, sea quarks[6] and gluons.

For low x and Q^2 big enough to resolve virtual quark-anti-quark pairs the proton seems to consist of a large number of particles, each of which carrying only a small amount of the proton momentum. The biggest contribution to the sea-quark content of the proton comes from the light $u\bar{u}$ and $d\bar{d}$ pairs. If Q^2 decreases, the number of sea-quark-pairs observed decreases as well.

For higher x only the valence quarks are seen, sharing most of the proton momentum. In this regime the proton is identified to be a bound state of three quarks, two up-quarks and one down-quark.

For reasons of simplicity a parton distribution function is only regarded for up-quarks (f_u, $f_{\bar{u}}$), down-quarks (f_d, $f_{\bar{d}}$) and gluons (f_g).

In electron-nucleon scattering the nucleon is probed by the electromagnetic force. Although the different electromagnetic charges of the quarks can be differentiated, their flavours cannot. Adding data from deep inelastic neutrino-nucleon scattering this problem can be circumvented[7].

Both charged currents mediated by the W$^\pm$ and neutral currents mediated by the Z^0 can be utilized to get information on the nucleon structure.

$$\nu_l + N \to l + N \text{ (Charged current)}, \quad \nu + N \to \nu + N \text{ (Neutral current)}$$

The vital difference to electron-scattering lies in the parity violation of the Weak force. The neutrino couples only to left-handed particles while the Anti-neutrino

---

[5] for a deduction see [3] and [6]

[6] Sea quarks are virtual quark-anti-quark pairs while valence quarks are non-virtual particles. The nucleon is characterized by its valence quark content.

[7] for a thorough treatment see [32]

couples only to right handed particles. Thus the cross sections behave differently for neutrinos and anti-neutrinos as can be seen in the case of the proton [6].

$$\begin{aligned}
\frac{d^2\sigma}{dxdy}(\nu_\mu + p \to \mu^- + X) &\propto xf_d(x) + xf_{\bar{u}}(x)\cdot(1-y)^2 \\
\frac{d^2\sigma}{dxdy}(\bar{\nu}_\mu + p \to \mu^+ + X) &\propto xf_u(x)\cdot(1-y)^2 + xf_{\bar{d}}(x) \\
\frac{d^2\sigma}{dxdy}(e^- + p \to e^- + X) &\propto x\left(\frac{2}{3}(f_u(x) - f_{\bar{u}}(x)) + \frac{1}{3}(f_d(x) - f_{\bar{d}}(x))\right) \\
&\quad \cdot \left[1 + (1-y)^2\right], \quad y = \frac{\nu}{E}
\end{aligned}$$

By combining the data from electron and neutrino scattering one is able to extract the parton distribution functions $f(x)$ for all quark flavours. If

$$\int_0^1 dx \quad x\left[f_u(x) + f_d(x) + f_{\bar{u}}(x) + f_{\bar{d}}(x) f_g(x)\right] = 1$$

is fulfilled the gluonic part $f_g(x)$ can be calculated as well.

The parton distribution functions have been measured for many (x, Q^2) combinations. For unknown points in the (x, Q^2) space the Altarelli-Parisi equations [33] give an evolution scheme for the $f(x)$ taking into consideration lowest-Order QCD corrections. The data collection for parton distribution functions used in this thesis can be found in [34].

2.1.2 Dynamic processes in hadronic collisions

An event detected after a collision took place differs significantly from what would be expected of an elementary interaction. Ignoring detector efficiencies there are several dynamic processes masking the underlying event structure.

Multiple interactions

In a hadronic interaction not only one interaction of two partons can take place. In addition a parton can be scattered on several partons in succession or more than two partons can interact at the same time. In both cases one speaks of multiple interactions.

Multiple interactions can alter the final energy of the outgoing particles produced in the reaction and can add new particles to the signal. For high-p_T – meaning high Q^2 – events considered in this thesis the remaining energy and the time available for theses processes do not change the signal significantly.

A more severe form of multiple interactions can arise if two or more particles inside the beam interact in one collision. This can lead to several interaction points in one collision which have to be resolved as different points by the detector.

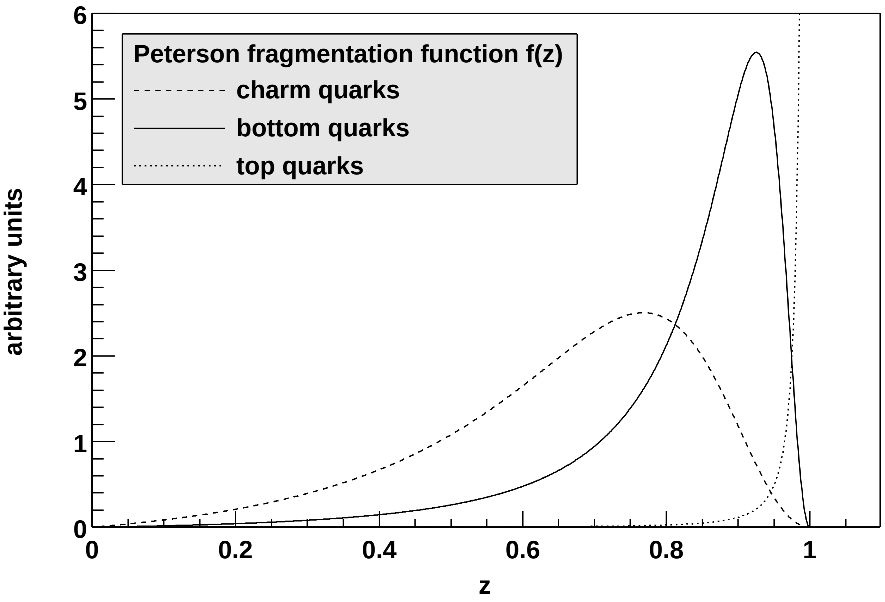

Figure 2.1: *Peterson fragmentation functions as used in the Monte Carlo generation*

Fragmentation of quarks and gluons to hadrons

Since quarks and gluons are confined into hadrons they cannot be observed as free particles. When leaving the interaction region the strong force between the particles grows and with it the energy density. If the energy density is high enough additional quark-anti-quark pairs and gluons are produced. Thus one outgoing parton can create several particles accompanying it. This process is called fragmentation.

Since the final state particles observed are hadrons without a colour charge the partons recombine to form these hadrons. One parton can produce several hadrons, all of them carrying away some of the initial parton momentum. For a high initial parton momentum the hadrons created by this parton get a Lorentz boost towards the direction of the parton momentum. They form a jet, a closely clustered beam of particles pointing into one direction.

The fraction z of the initial longitudinal quark momentum carried away by the quarks created in the fragmentation process can be expressed in terms of the fragmentation functions $f(z)$.

For light quarks (u, d) these distributions are spread over the whole $0 \leqslant z \leqslant 1$ range while for heavier quarks (c,b) they are peaked at high z, meaning that the primary heavy quark in the fragmentation cascade keeps most of its initial momentum.

A parameterization for the fragmentation function for charm and bottom quarks of mass m_Q is given by [35]

$$f(z) \propto \frac{1}{z\left(1-\frac{1}{z}-\frac{\epsilon_Q}{1-z}\right)^2} \tag{2.5}$$

where $\epsilon_Q \propto 1/m_Q^2$ is a free parameter, see also figure 2.1 on the preceding page. Fragmentation plays a key role when identifying partons produced in an event. This is done in several steps. First the hadrons observed are grouped together to form jets. For this task several jet finder algorithms exist. Typically two up to six jets are found per event.

The momentum of the jet is calculated summing over the momenta of the hadrons to reassemble the initial parton momentum. The identification of the jet with a specific parton is called tagging. Tagging uses information like the transverse momentum, the particle content or the vertex position of the jet to assign a flavour-tag to it. Jet-finding and flavour-tagging are not free of ambiguities and therefore fragmentation processes strongly influence the observed signal.

Initial State Radiation

Initial State Radiation (ISR) modifies the event structure mainly by adding additional particles and jets to the event. When reaching the vicinity of the interaction region the particles in the beam are exposed to the force fields of their colliding partner and can radiate bosons mediating the force fields before the collision takes place.

The resulting boson takes away some fraction of the initial parton energy. Some of this energy is needed to produce the real boson which therefore has to be light, in hadronic collisions these are photons and gluons. Photons can be distinguished from jets, for gluons this is not the case. The hadrons created by hadronization of the gluon can result in an additional jet observed in the event or, in a worse case, will be added to existing jets. In this case the jet energy is higher than would be expected by fragmentation and the invariant mass of the jet increases.

Final State Radiation

Final State Radiation (FSR) occurs if one of the outgoing particles radiates a boson after the collision. In most cases this radiation is soft, the bosons take away only a small fraction of the particle's energy. Nevertheless successive radiation of bosons decreases the initial jet energy.

If an invariant mass spectrum of two jets coming from the two-body decay of a particle is considered, FSR results in an additional tail in the spectrum pointing towards lower reconstructed masses.

2.1.3 Particle production in hadronic collisions

Disadvantages of Hadron colliders

As pointed out in section 2.1.1 the partons interacting carry only a fraction of the proton momentum. Thus not all of the proton energy can be exploited to produce particles. The momentum distribution for a parton cannot be calculated from the energy of the proton in the beam which results in an initial collision state not known to the experimentalist.

The typical event treated in this thesis includes several hundred particles in the final state. These particles are created in dynamic processes like those considered in section 2.1.2. This huge number of particles is responsible for both spatial and temporal pile up of particle detections in the detector (see 3.1.2). Most of these particles have a low transverse momentum because they arise from low Q^2 interactions like elastic parton scattering or radiation processes and can be separated from high p_T particles considered as a sign for interesting events.

Advantages of Hadron colliders

As far as circular colliders – storage rings [36] – are regarded, the loss of beam energy induced by Synchrotron radiation becomes important. When the beam is bended in the magnets to follow the ring's curvature a magnetic force is exerted on the beam particles which radiate due to the acceleration [37].

For one revolution of a particle of energy E and mass m in a storage ring of radius R the energy loss E is [36]

$$\Delta E \propto \frac{1}{(mc^2)^{\mathbf{4}}} \frac{E^4}{R} \Rightarrow \frac{\Delta E_{proton}}{\Delta E_{electron}} = \left(\frac{m_e}{m_p}\right)^4 \approx 10^{-\mathbf{13}}$$

and decreases with the fourth power of the beam particle's rest mass. The high proton mass efficiently suppresses Synchrotron radiation, hence in a pp or p$\bar{\text{p}}$ ring the beam energy can be much higher than in an e^+e^- ring.

The momentum distributions of the partons interacting are continuous. In each collision the parton momenta are different and so the center of mass energy in the parton-parton system is different. Although the hadron beams in the collider have a fixed center of mass energy the collision energies are distributed over a range of values. Therefore with a fixed beam energy a hadron collider experiment can explore physics over an energy range – in this sense hadron colliders are sometimes called discovery machines.

2.1.4 Machine parameters of Hadron storage rings

The TEVATRON and the LHC are both examples of storage rings. A storage ring [36] is designed to store beams of particles whose momenta do only differ slightly. In the ring, magnets bend the particle trajectories to form a closed circle.

Two beams are circulating inside the storage ring, one clockwise, the other counterclockwise. In the case of p$\bar{\text{p}}$ rings the different charge q of protons and anti-protons allows the use of one beam pipe for both particle types because the field of the bending magnets deflects the counter-rotating anti-protons and protons in the same direction – thus for a pp collider two separate beam pipes and magnet systems have to be built.

The two beams are brought together at the interaction regions around which a detector is placed. A first characterization of storage rings can be made in terms of the center of mass energy (CM) E_{CM} and the ring radius R. They are linked by the bending magnets' field strength B

$$E_{CM} \propto \pm q \cdot BR \tag{2.6}$$

In a storage ring particles are concentrated in bunches, there is no continuous beam of particles. For TEVATRON and LHC each bunch carries about 10^{11} particles. The section of a bunch transverse to the beam is determined by the horizontal width σ_x and the vertical width σ_y. The luminosity $\mathcal{L}$ is defined by the production rate $\dot{N}_{process}$ and the cross section $\sigma_{process}$ for a given physical process by

$$\dot{N}_{process} = \mathcal{L}\; \sigma_{process} \tag{2.7}$$

In terms of the number of bunches $N_{bunches}$ in the beam, the revolution frequency f_{Rev}, the numbers of particles N_1 and N_2 in the colliding bunches this leads to

$$\mathcal{L} = \frac{1}{4\pi} N_{bunches} \cdot f_{Rev} \cdot \frac{N_1 N_2}{\sigma_x \sigma_y}, \quad f_{Rev} = \frac{c}{2\pi R} \approx 10^4 Hz \tag{2.8}$$

The integrated luminosity L_{Int} is a measure for the number of events one can expect for a specific physical process.

$$L_{Int} = \int_T dt\; \mathcal{L}, \quad [L_{Int}] = barn^{-1}, \quad 1\, barn = 1\, b = 100\, fm^2 \tag{2.9}$$

The machine parameters for the TEVATRON and LHC are found in section 2.4.

2.2 The Tevatron at Fermilab

The TEVATRON is a p$\bar{\text{p}}$ storage ring of 6.3 km circumference and a center of mass energy of 2 TeV situated in Batavia, Illinois, near Chicago. In March 2001 the TEVATRON Run II program started. After a five years break an upgraded accelerator chain and detectors resumed work[8]. The Run II is subdivided in Run IIa which will allow to collect 2 fb^{-1} in about two years and Run IIb with 2 fb^{-1} expected in about four years.

---

[8] Most of the information in this section can be found in [38] and [39].

2.2.1 The accelerator chain

First steps in the accelerator chain

As mentioned in 2.1.4 a storage ring is not designed to accelerate the resting beam particles right after they have been produced. To fill the storage ring the beam particles have to be accumulated and accelerated. This is done in the accelerator chain[9].

A schematic overview of the TEVATRON accelerator chain can be found in figure 2.2.

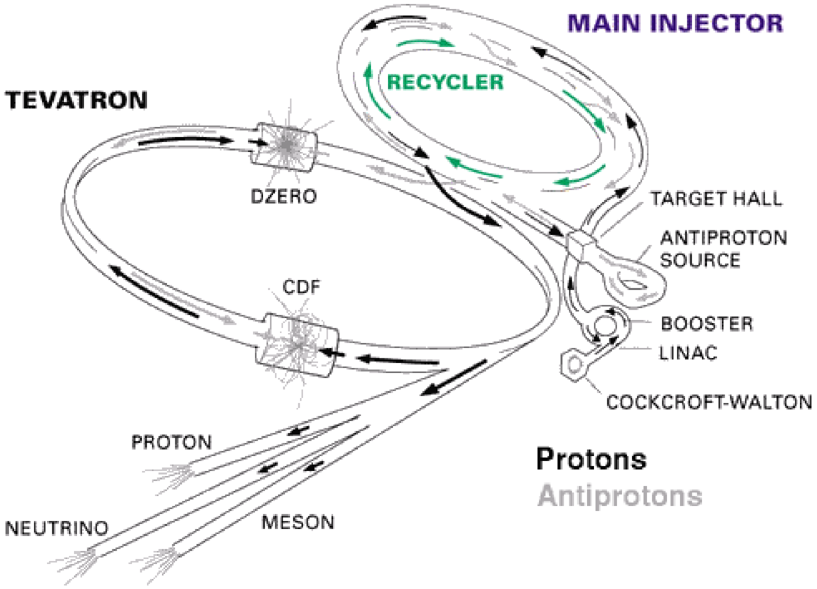

Figure 2.2: *Schematic view of the Tevatron accelerator chain*

Protons are easily produced from hydrogen atoms. The TEVATRON acceleration chain starts with ionised hydrogen H^- coming form a 25 keV source. In Run II the brightness of the source is increased to deliver more protons than in Run I. The ions are accelerated in a Cockroft-Walton cascade generator, an electrostatic accelerator with a potential difference of 750 kV.

The 750 keV H^- ions are passed through a 106 MeV Alvarez high frequency drift tube to a linear accelerator(Linac), leaving it with an energy of 440 MeV. At the end of the Linac the H^- ions pass through a carbon foil which removes the two electrons, leaving protons.

After the Linac the protons enter the Booster, an 8 GeV circular accelerator. At normal operation the beam particles oscillate around the desired orbit and show variations in their velocity. The oscillations are called Betatron oscillations, the velocity variations Synchrotron oscillations. For the higher proton fluxes in Run II the damping system for these oscillations was redesigned. Additionally

---

[9] The different types of accelerators mentioned are described in [36]

the shorter temporal bunch spacing in Run II required a change in the extraction to the Main Injector.

The Main Injector and the Anti-proton source

The Main Injector synchrotron accelerates the 8 GeV protons to 150 GeV. In addition it provides a 120 GeV proton beam for the production of anti-protons. In $p\bar{p}$ colliders the main limitation to the luminosity is the rate of anti-protons injected in the storage ring – unlike proton production the production of anti-protons requires high energy processes like the collision of a proton beam with a fixed target.

The increase in luminosity envisaged for Run II focuses on the increase of the anti-proton delivery rate. The Main Injector proton beam is divided into bunches of particles, each bunch filling a region in phase space. Repeated filling of bunches into the ring is called stacking.

When producing anti-protons the 120 GeV proton beam is focussed on a fix nickel-copper-Target. For the production of one anti-proton typically 10^5 protons are needed. The anti-protons are focussed by a solid lithium solenoid lens and are separated by a dipole magnet. In Run II the focal strength of the lens is increased by a factor 1.5.

The momentum spread of the anti-protons is reduced in the Debuncher, a triangular storage ring in which the anti-proton beam size is cooled stochastically[10]. The cooling bandwidth, meaning the acceptance of momentum spread of the Debuncher and the aperture of the Debuncher are increased in Run II.

In the Accumulator ring the Anti-protons are grouped to bunches and are cooled stochastically. For Run II more anti-protons have to fit into the Accumulator. They are transferred to the Recycler, a new component added for Run II. The Recycler is placed directly on top of the Main Injector ring and has the same circumference of approximately 3.3 km.

After each run anti-protons are left in the Tevatron beam pipe. In Run I these anti-protons had to be dumped and were lost for the succeeding runs. In Run II they are ejected into the Recycler ring where they are stored with the anti-protons coming from the Accumulator ring.

As can be seen from equation (2.8) a decrease in the bunch volume increases the luminosity of the anti-proton beam. Methods of beam cooling achieve this by damping the Betatron and Synchrotron oscillations of the particles.

For the Recycler ring electron cooling has been introduced to cool the anti-proton beam. Since electron beams can be cooled more efficiently[11] mixing *hot* anti-protons with a cooled electron beam decreases the anti-proton beam temperature by momentum exchange between anti-protons and electrons.

---

[10] In stochastic cooling the particle's displacement from the design orbit is measured by a pickup electrode. The displacement is later corrected by a kicker electrode.

[11] due to Synchrotron radiation damping

2.2.2 The Tevatron ring

Since the major changes for Run II consider an increase in luminosity by increasing the number of particles and bunches in the beam the TEVATRON bunch stacking system was changed. Additionally the super-conducting acceleration cavities operate at higher frequencies and with a higher voltage.

The main machine parameters for the TEVATRON Run IIa and IIb are listed in section 2.4.

2.3 The Large Hadron Collider at CERN

The LHC project is scheduled to start in 2006 at CERN near Geneva, Switzerland. Situated in the tunnel formerly occupied by the LEP e^+e^- accelerator the LHC pp collider will have a circumference of 26.7 km and a center of mass energy of 14 TeV, seven times the TEVATRON energy[12].

2.3.1 The accelerator chain

The LHC accelerator chain [40, 41] – see figure 2.3 on the next page – uses the existing PS and SPS accelerator facilities. 92 keV protons from a proton source are injected into the accelerator chain by a 705 kV radio frequency cavity into a pulsed Alvarez Linac where they are accelerated to 50 MeV. For the LHC project a high current and a high pulse rate are required.

The protons are accelerated in the PS Booster ring to nearly 1 GeV before being injected to PS, the Proton Synchrotron ring. For the LHC the PS Booster ejection energy will be raised to 1.4 GeV and new radio frequency equipment will be added to the PS ring to achieve the desired LHC bunch spacing. In November 2000 nominal LHC operation was achieved.

Following the PS the SPS, the Super Proton Synchrotron, has to accelerate the 26 GeV protons coming from the PS to an energy of 450 GeV. The requirements demanded by the LHC design luminosity include changes in the radio frequency system, an upgrade of the injection and ejection facilities and an improvement in damping the Betatron oscillations.

2.3.2 The LHC ring

The LHC [42] will work near the bunch density limit set by the charge density of a bunch. When two bunches cross only a tiny fraction of the particles inside the bunches collide, the rest is deflected by the charges inside the beam. These small deflections add up after each turn and particles can get lost. This beam-beam effect limits the bunch charge density.

Eight 2 MV super-conducting cavities per beam will be accelerating the two proton beams at the LHC. Each cavity is made of copper with a thin coating

---

[12] Since research and tests are still going on in 2001/2002 only preliminary information is given in this section

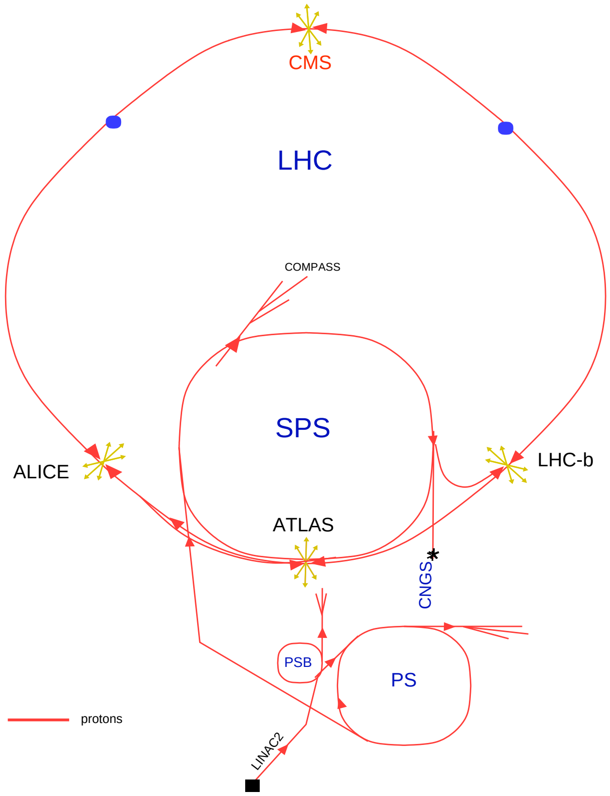

Figure 2.3: *Schematic view of the LHC accelerator chain*

of super-conducting nyobium, a technique used at LEP. The bending dipole magnets have to create a magnetic field of over 8 Tesla. To reach this field strength super-conducting coils are required.

A good vacuum in the beam pipe is essential to reach beam storage times of ten hours and more and a cooling of the beam pipe via a cryogenic system is needed.

2.4 Comparing LHC and Tevatron

Table 2.1: **Tevatron and LHC**

Collider	TEVATRON		LHC	unit
Run	IIa	IIb	high $\mathcal{L}$	–
Particles	p$\bar{\text{p}}$		pp	–
center-of-mass energy	2		14	TeV
Circumference	6.28		26.659	km
Interaction regions	2		3	–
$\mathcal{L}$	0.86	5.2	100	$10^{32} cm^{-2} s^{-1}$
L_{Int}	2	15	$100/year$	fb^{-1}
Bunches per ring per species	36	140 [103][13]	2835	–
Particles per bunch	27 [3]	27 [4]	10.5	10^{10}
Bunch spacing	396	132	25	nsec
Interactions per crossing	2.3	4.8	≈ 20	–

Machine parameters for the TEVATRON *and the* LHC.

Following [22] differences in the physics of p$\bar{\text{p}}$ and pp colliders become small at high energies. Hence the important parameters for a comparison are the integrated luminosity and the center of mass energy. The machine parameters for TEVATRON and LHC are listed in table 2.1.

The values given for the LHC refer to the design luminosity. At the start of LHC the collider will operate with a ten times smaller luminosity. In this thesis the low luminosity option was considered for reasons of comparability with [43].

Chapter 3

Detectors at Hadron Colliders - DØ and ATLAS

3.1 Physics requirements on the detector performance

The two channels $\mathrm{Z^0 + H \rightarrow l^+l^- + b\bar{b}}$ and $\mathrm{W^\pm + H \rightarrow l^\pm \nu + b\bar{b}}$ discussed in section 1.2 set constraints to the detector performance. Here an overview is presented to prepare a comparison of DØ and ATLAS[1].

3.1.1 Detector coordinate system

A description of particle tracks in a detector requires a coordinate system. For both detectors a right handed coordinate system is defined in the following way: The z-axis points in the direction of the beam, the x-axis to the center of the ring and the y-axis upwards. The center of the coordinate system is defined by the center of the interaction region.

The particle tracks are defined by the azimuthal angle ϕ, the transverse momentum p_T and the pseudorapidity η. The pseudorapidity is an approximation to the rapidity y:

$$y = \frac{1}{2}\log\left(\frac{E+p_L}{E-p_L}\right), \quad \eta = -\log\left(\tan\frac{\theta}{2}\right), \quad \eta \approx y \tag{3.1}$$

with p_L being the particle's longitudinal momentum with respect to the beam axis, E its energy and θ the polar angle of the particle track.

3.1.2 Detector operation at high luminosity

The luminosities listed in 2.4 cause a pile up of particle signals in the detector. There are two types of pile up which have to be considered in the detector design, temporal and spatial pile up.

---

[1] For a description of the detector parts mentioned in this section please refer to sections 3.2 and 3.3.

For the temporal pile up the dead time and the readout time of the detector components are critical.

Every detector component has an idle time. In most components the charge deposited by traversing particles is measured and the remaining space charge has to be removed before a subsequent particle crosses the detector volume. This results in a maximum repetition rate for measurements.

Even if a detector is able to handle high repetition rates the information gathered has to be read out and made available for analysis. Fast readout electronics and trigger systems – which decide if a signal should be discarded or not – collect and reduce the event information.

The spatial pile up in the detector is caused by too many particles penetrating the detector simultaneously in a too small volume. This is especially important near the interaction region where single particle tracks have to be identified. A high detector granularity is necessary to avoid ambiguities and distinguish individual particles.

Another consequence of high luminosity is radiation damage inside the detector. The highest doses are found near the interaction region, demanding radiation hard hardware for the inner detector.

3.1.3 Transverse momentum measurement

The transverse momentum of charged particles can be calculated from their measured track in a magnetic field parallel to the beam axis.

In a magnetic field of strength B charged particles are deflected by the Lorentz force and follow a curved track. In the case of a solenoid field the transverse momentum p_T can be calculated from the track curvature by [44]

$$p_T = 0.3 \cdot \frac{BL^2}{8s}, \quad [p_T] = GeV/c, \quad [B] = T, \quad [L] = m$$

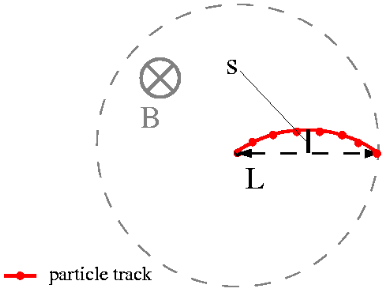

Figure 3.1: *Momentum measurement in a solenoid magnet*

The relative error of the momentum measurement is related to the spatial accuracy $\sigma_{spat.acc.}$ of a single track point and the number N of track points measured by [45]

$$\frac{dp_T}{p_T^2} = \frac{\sqrt{3}}{2}\frac{8}{0.3BL^2} \cdot \sqrt{\frac{720}{N+4}} \cdot \sigma_{spat.acc.}$$

Thus a better spatial resolution, an increase in the number of track point measurements a higher magnetic field and, most importantly, an increase of the solenoid radius L enhance the momentum resolution.

3.1.4 Energy measurement

The energy of particles is measured in the detector calorimeters. A particle traversing the detector material looses energy. The energy deposition in matter differs for different kinds of particles and can be exploited for particle identification.

The relative energy resolution of a calorimeter can be parameterized by three terms [44]

$$\frac{dE}{E} = \frac{a}{\sqrt{E}} \oplus \frac{b}{E} \oplus c = \sqrt{\left(\frac{a}{\sqrt{E}}\right)^2 + \left(\frac{b}{E}\right)^2 + c^2}, \quad [E] = GeV$$

The term $a/\sqrt{E}$ is called the stochastic term and accounts for statistical fluctuations in the number of processes generating the primary signal. The second term b/E includes electronic noise and pile up effects. The constant term c originates in non-uniform signal collection, energy leaks and calibration errors.

A detector component is characterized by the radiation length and the nuclear absorption length.

The radiation length is a typical length for the occurrence of bremsstrahlung and electromagnetic scattering processes [45].

Photons from bremsstrahlung are radiated by charged particles if they interact with the electromagnetic field of the nuclei of the detector material. If their energy is high enough they can create electron-positron pairs which likewise can emit bremsstrahlung. Thus a cascade of electron-positron pairs and photons can develop inside the detector called an electromagnetic shower.

In dense materials with high atomic numbers hadrons are likely to interact strongly with the nuclei and fragment. Subsequent interactions result in a hadronic shower. The typical length on which a strong interaction of high energetic particles with the nuclei is likely to occur is called the nuclear absorption length. Electromagnetic showers are shorter and more collimated than hadronic showers.

3.1.5 Identification of leptons

For both channels $\mathrm{W} + \mathrm{H} \rightarrow \mathrm{l}\nu + \mathrm{b\bar{b}}$ and $\mathrm{Z}^0 + \mathrm{H} \rightarrow \mathrm{l}^+\mathrm{l}^- + \mathrm{b\bar{b}}$ leptons have to be identified. All three lepton flavours, electrons, muons and taus have to be considered and each flavour requires special detector features.

The leptons observed in $W^{\pm}H$ or Z^0H events originate in a $W^{\pm}$ or Z^0 decay[2]. In both decays the light lepton has a high energy since it comes from the decay of a heavy particle ($m_{W^{\pm}}, m_{Z^0} > 80 GeV/c^2$).

The final $W^{\pm}$ and Z^0 bosons are produced on-shell. For the Z^0 this allows the reconstruction of the invariant mass if both leptons from its decay are observed in the detector (the leptonic $W^{\pm}$ decay always includes an unobservable neutrino).

In the associated Higgs production the off-shell vector bosons loose most of their energy in the Higgs radiation process due to the large Higgs mass considered ($m_{h_0} \geqslant 90 GeV/c^2$). In most cases the final state bosons have low momenta.

For the signal only those leptons with high transverse momentum in a pseudorapidity region centered around $\eta = 0$ are considered. To use cuts on the invariant Z^0 mass, the energy and momentum measurements have to be good enough to reconstruct a mass peak.

Finally a good track resolution is required to distinguish different event topologies – for example in the case of the $t\bar{t}$ background, the two observed leptons come from the decay of two separate particles, a W^+ and a W^-.

Electrons, muons and taus are reconstructed in different parts of the detector. Electron reconstruction uses the inner detector, where the electron's track parameters and charge are determined, and the electromagnetic calorimeter.

The main information on the muons comes from the muon spectrometers situated on the outside of the detector. The tau lepton can decay hadronically, producing a jet. In this analysis the misidentification of a τ-jet as a heavier b-jet is considered – to distinguish both the b-tagging efficiency of the detector is crucial (see section 3.1.8).

3.1.6 Missing transverse energy measurement

In the case of the $W + H \rightarrow l\nu + b\bar{b}$ channel a significant part of the event energy is not observed due to the invisible neutrino energy.

Only the missing transverse energy E_T^{miss} is accessible in the detector. The loss of near-beam-pipe particles outside the detector acceptance can be compensated in a detector calibration and is not vital for the determination of the neutrino energy.

Especially in the case of ATLAS the pile up of particle signals in the detector makes a good determination of the energy deposited in the detector volume necessary.

This requires a hermetic coverage of the event region and a precise linear energy response in the calorimeters.

3.1.7 Jet energy measurement

The Higgs mass is calculated as the invariant mass of two b-tagged jets. A precise knowledge of the b-jet four vectors is needed to discriminate the mass

---

[2] the decay $H \rightarrow l^+l^-$ is not considered in this study because it is suppressed with respect to $H \rightarrow b\bar{b}$

peaks created by the decays $Z^0 \to b\bar{b}$ and $H \to b\bar{b}$.

The b-jets coming from the Higgs decay have a high transverse momentum $\mathrm{p_T}$, hence the momentum measurement distinguishes these jets from low-p_T jets originating in background processes. This demands a good energy resolution and granularity in the hadronic calorimeter to determine the value and direction of momentum for all particles as an input to the jet-finder algorithms.

Dynamic effects discussed in section 2.1.2 can only be compensated if all the particles originating from fragmentation and radiation processes are detected and the jet energy measurement is accurate enough to serve as an input to a jet calibration algorithm. Thus the response to energy deposition inside different detector parts and the minimal energy deposition creating a response have to be accounted for.

3.1.8 Identification of b-jets

The most crucial detector performance issue is the jet flavour tagging, identifying the flavour of the quark forming the jet. There exist several tagging schemes using information gathered in different parts of the detector.

A tagging scheme can be characterized by a tagging efficiency, giving a value for the probability of identifying the correct flavour content, and a mistagging probability for assigning an incorrect flavour content to a jet.

In the special case of the decay $\mathrm{H} \to \mathrm{b\bar{b}}$ the b-tagging efficiency greatly influences the signal observed in the detector. For ATLAS and DØ the maximum achievable b-tagging efficiency is about 60%. Since two bottom flavoured jets have to be identified only about a third of all events survive and enter the analysis.

A bottom quark has a mass of about 4 GeV, approximately four times heavier than the charm quark. The bottom flavoured hadrons (B-hadrons) formed in the fragmentation process carry most of the original quark momentum[3].

The high invariant mass accounts for a wide spread of the tracks inside the jet, because a larger fraction of each particle momentum will be transverse with respect to the original quark direction, and thus can cancel out large momentum components from other particles in the jet.

The weak decay of B-hadrons involves a flavour change resulting in a long lifetime of about 1.5 ps^{-1}. Before the decay a B-hadron can travel a measurable distance of the order of 1 mm, forming a displaced secondary vertex.

The Lifetime tag

A first step in b-tagging is the determination of the signed transverse impact parameter d_0. The impact parameter is the transverse distance of the jet-track to the beam axis at the point of closest approach. The direction of a reconstructed jet when extrapolated to the primary vertex defines the so called jet axis.

---

[3] See notes on fragmentation in 2.1.2.

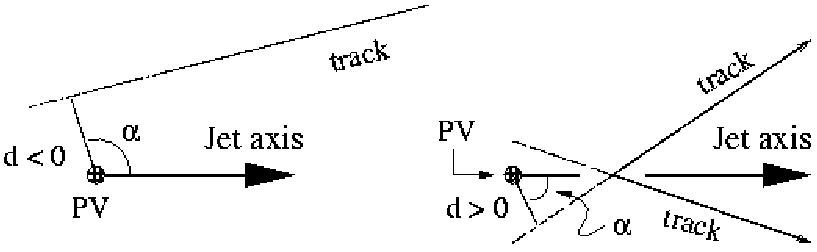

Figure 3.2: *Definition of the signed impact parameter*

A charged particle track is assumed to belong to a jet coming from a secondary vertex if the angle α enclosed by the line defined by the impact parameter and the jet axis is less than $\frac{\pi}{2}$ – it then has a positive impact parameter. Otherwise the track is expected to originate in the primary vertex or to belong to a different jet – in which case its impact parameter is negative (see figure 3.2).

By this method the impact parameters of the tracks, weighted by their measurement errors, are distributed symmetrically around zero for jets with tracks coming from the primary vertex. For jets with a displaced secondary vertex the distribution shows a surplus of positive values. Thus the form of the distribution can help identify jets coming from a secondary vertex.

A high track resolution is required to measure the impact parameter with high accuracy.

Reconstruction of the secondary vertex

Reconstructing the vertex position requires a good reconstruction of particle tracks inside the inner detector system. In addition the spatial resolution of the detector near the beam pipe must allow for a decision whether tracks originate in the same vertex or not.

A secondary vertex can be reconstructed in either two dimensions – in the (R, ϕ) plane – or three dimensions, with a supplemental measurement of the z-coordinate. Since the interaction region itself is spread out in z-direction a good knowledge of the primary vertex position event-by-event is essential[4].

Looking for leptons with high transverse momentum inside jets

An additional mean to tag a b-jet is to look for soft leptons, electrons or muons, with a high transverse momentum inside reconstructed jets.

Inside a b-jet the leptons originating in the semi-leptonic decay of the bottom quark have a high transverse momentum relative to the jet-axis due to the high mass of the bottom quark. Thus the transverse momentum of the leptons belonging to a jet indicates if the jet is formed by a light quark or a heavy quark.

---

[4] If multiple interactions are taken into account, there can exist more than one primary vertex.

3.2 The DØ Detector

3.2.1 Overview of the DØ detector layout

DØ is one of the two multipurpose detectors at the Tevatron. In this section the upgraded DØ detector for Run II of the Tevatron is described [46–48].

The detector can be subdivided into three main parts, the inner detector, the calorimeter system and the muon spectrometer. The whole detector is about 20 meters long and 10 meters high.

Its subsystems are divided into a central cylindrical barrel part and two end-cap parts on each side of the barrel.

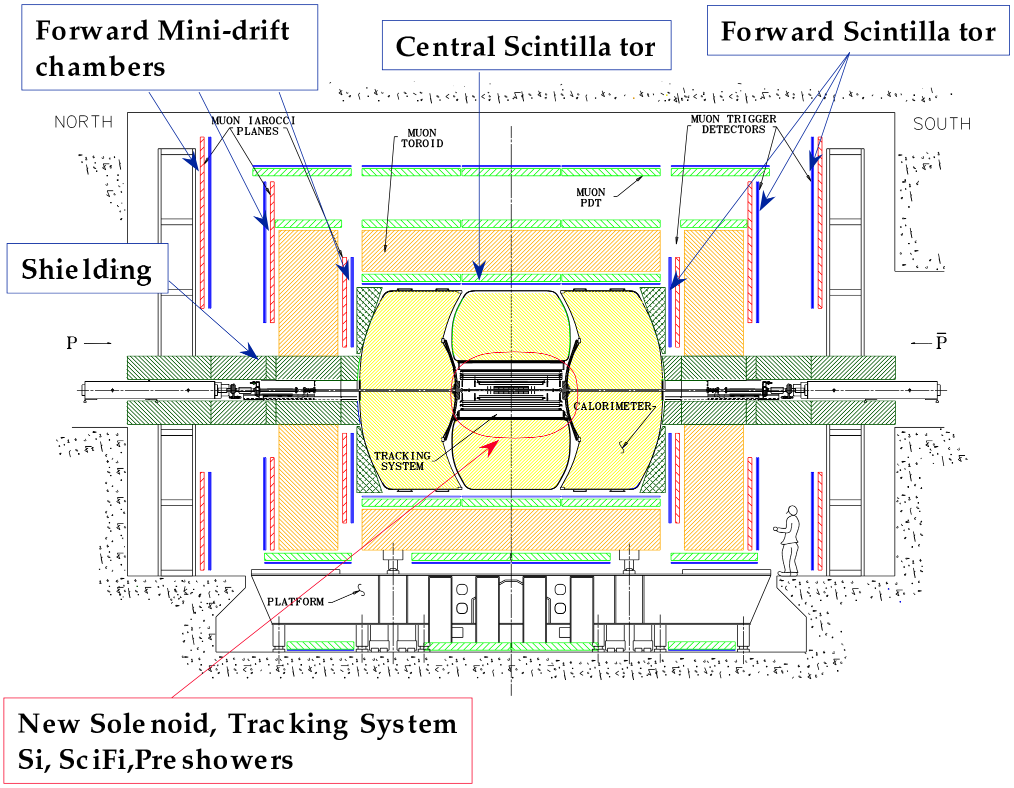

Figure 3.3: *Schematic view of the DØ detector*

3.2.2 The DØ Inner Detector

The DØ inner detector provides a spatial image of the tracks of charged particles allowing a determination of charge momentum and impact parameter – neutral particles do not leave signals in the inner detector.

The inner detector was fully redesigned for Run II and replaced the old central detector systems. It encloses the interaction region where the proton and anti-proton beams collide.

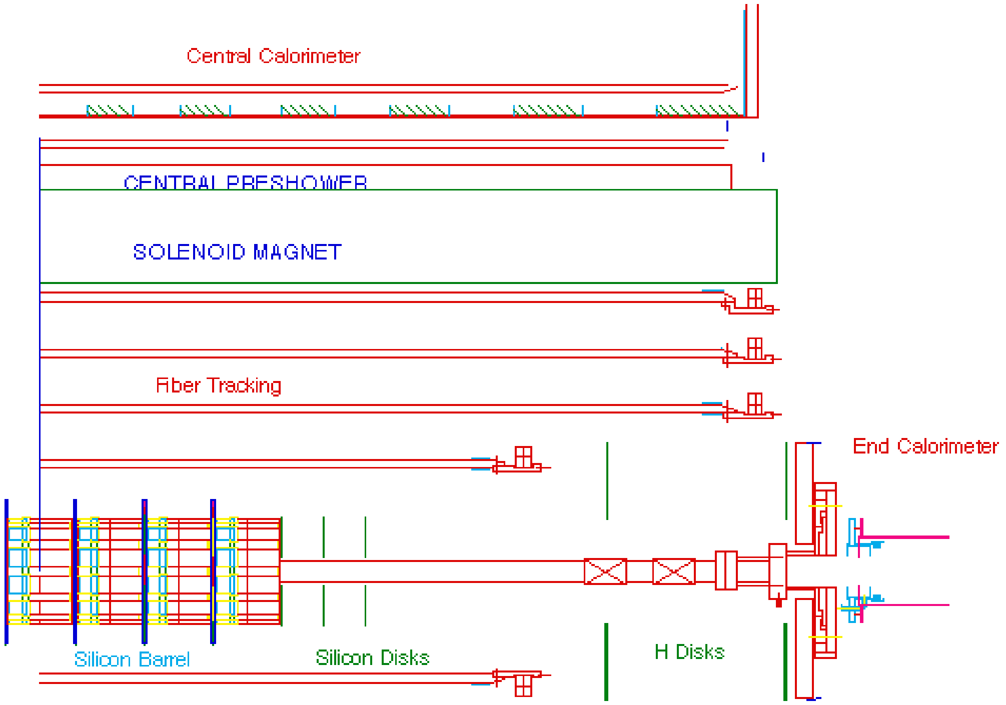

Figure 3.4: *Side view of the DØ Inner Detector*

The Solenoid Magnet

The inner detector is surrounded by a super-conducting solenoid magnet with a field strength of 2 Tesla. The solenoid, a two layer coil with a mean radius of 0.6 meters, is about 2.8 meters long and is housed in a liquid helium cryostat. Its field is uniform to 0.5 % and parallel to the beam axis.

The Silicon Vertex Detector

The silicon vertex detector (SVD) is closest to the beam pipe and has a radius of 0.2 meters. It covers the pseudorapidity region up to $|\eta| = 3$ and is divided into a barrel part – measuring the $\mathrm{r} - \phi$ coordinates of particle tracks – and a disk part which measures $\mathrm{r} - \mathrm{z}$ and $\mathrm{r} - \phi$ coordinates.

Both parts consist of silicon microstrip detectors: Semiconducting strip detectors which collect electron-hole pairs created by charged particles passing the detector, which allow track position determination in one dimension.

There are six concentric barrel layers of microstrip detectors parallel to the beam axis. The layers are rotated to each other in a 90° angle to achieve a point resolution of 10 μm. A small stereo angle between the layers also provides information on the z-coordinate.

The disk system is divided into a small inner disk near to the barrel and a larger outer disk with the microstrip detectors perpendicular to the beam axis. This setup allows to measure all three space coordinates of a particle hit.

A vertex resolution of 40 μm in the (r, ϕ) plane and 100 μm in z-direction is achieved.

The Scintillating Fiber Tracker

Surrounding the SVD the fiber tracker extends to a radius of about 0.5 meters from the beam pipe. The fiber tracker is used for track reconstruction in the region $|\eta| \leqslant 2$ and provides fast triggering for electrons and muons. The 2.6 meter long fibers have a diameter of 830 μm.

If a particle passes a fiber part of the deposited energy is re-emitted as scintillation light and picked up by photo-multipliers at each end of the fiber which convert the light signal into an electronic signal. The difference in the detection time at both fiber ends allows the determination of the z-coordinate of the particle hit. Scintillation fibers show fast response.

Eight concentric cylindric layers of fibers parallel to the beam axis allow a spatial resolution of about 100μm by shifting the layers to each other. The (r, ϕ) information from fiber hits is used in the first trigger level.

3.2.3 The DØ Calorimeters

Changes imposed on the DØ calorimeter system for Run II mainly concern new readout electronics, the original Run I setup was preserved and is presented here.

There exist a central and an end part, both liquid argon sampling calorimeters housed in cryostat vessels.

A modular calorimeter design was chosen, integrating the electromagnetic calorimeter in the hadronic calorimeter, thereby reducing the need for complex cryogenic systems. Both electromagnetic and hadronic calorimeter have a spatial resolution of $\Delta\eta \times \Delta\phi = 0.1 \times 2\pi/64$. The energy resolution for the electromagnetic calorimeter is about $0.2/\sqrt{\mathrm{E}}$ and $0.8/\sqrt{\mathrm{E}}$ for the hadronic calorimeter.

Preceding the electromagnetic calorimeter a preshower detector, subdivided in a central and a forward part, is used for electron identification and energy sampling with high granularity to support track finding.

The Central Calorimeter

The central calorimeter covers the region of $|\eta| \leqslant 1$. It consists of about seven absorption lengths of material.

The central electromagnetic calorimeter placed in front of the hadronic calorimeter has a thickness of approximately 20 radiation lengths and is subdivided in 32 modules, each with a four layer structure.

The first two layers measure the longitudinal shower development near the beginning of the shower. The third layer spans the region of maximum electromagnetic shower energy deposits and the fourth completes a module.

Plates of 3 mm thick nearly pure depleted uranium are interspersed by 2.3 mm gaps filled with liquid argon. Electromagnetic showers initiated in the high Z uranium material develop in the calorimeter, the charged shower particles ionise the argon and the ions are collected by two electrodes on each side of the gap.

A calorimeter with active regions alternating with regions of dense material where particle showers initiate is called sampling calorimeter. The potential between the electrodes is typical 2 to 2.5 kV, resulting in an ion drift time of 400 ns.

The central hadronic calorimeter consists of 16 modules with 6 mm thick uranium-niobium alloy and another 16 modules with copper or stainless steel plates with a thickness of 46.5 mm. The former cover a length of 3.2 nuclear absorption lengths, the latter another 3.2.

Electromagnetic and hadronic calorimeter modules are segmented longitudinally because the longitudinal shower profile helps to distinguish electromagnetic and hadronic showers.

The End Cap Calorimeters

The end cap calorimeters placed on each side of the central calorimeter span the region of $|\eta|$ up to 4. The layout is similar to the central calorimeter. The inner part of the end cap calorimeter contains one electromagnetic and one hadronic module, the outer concentric rings consist of 16 modules.

Central and end cap calorimeter are housed in separate cryostats. The gap in between the cryostats is occupied by the intercryostat detector, an array of scintillation counters. Having the same granularity as the central and end cap calorimeter, it minimizes the amount of dead space in the detector and is vital to determine missing transverse energy and jet energy.

For the DØ upgrade the intercryostat detector had to be moved to a region where the influence of the solenoid's magnetic field on the photo-multipliers is less severe.

The Central Preshower detector

The cylindrical central preshower detector is placed in a 5 centimeter gap between the solenoid coil and the cryostat housing the central calorimeter at a distance of about 0.7 meters from the beam pipe.

Three axial layers of scintillating fibers cover a range of $|\eta| < 1.3$. A lead absorber before the detector completes the material before the central preshower to two radiation lengths to initiate particle showers.

A position resolution of 1.4 mm for electrons and 0.6 mm for muons has been obtained[5]. More importantly, the fast photo-multipliers and read out electronics

---

[5] The muon is heavier than the electron, thus it produces less bremsstrahlung and leaves a track while an electron produces a shower

provide low-level trigger information which rejects unwanted events and reduces the amount of data still to analyse by a factor of three.

Energy loss and spatial resolution help identifying electrons and muons. For the energy calibration LEDs[6] are used.

The Forward Preshower detector

The forward preshower detector is mounted on the cryostat wall of the end-cap calorimeter. It is subdivided in two concentric disks on each side of the cryostat vessel, with an outer radius of 33 cm and 58 cm respectively. The disks cover the range $1.4 < |\eta| < 2.5$.

Their performance is comparable to that of the central preshower detector. In addition they give track information in the z-direction owing to their mounting perpendicular to the beam.

3.2.4 The DØ Muon spectrometer

The muon spectrometer consists of several subsystems required to identify muons and measure the transverse muon momentum independently from the inner detector. There are three types of detectors used in the spectrometer, proportional drift tubes, mini drift tubes and scintillators.

Proportional and mini drift tubes have a centered wire and are filled with a mixture of gases. If a particle hits a tube the gas inside the tube is locally ionised. An electric field between the central anode wire and the tube mantle collects the ions and free electrons. Near the anode wire the electrons are accelerated owing to higher field strengths until their energy is high enough for secondary ionisation, forming an electron-avalanche.

The ions induce an electric charge on the anode wire which decreases while the ions drift to the outer wall. Triggering on the rising induction signal enhances the spatial resolution of the track measurement from the tube diameter to 50 μm.

Outside the calorimeter a toroid magnet system, a central toroid and two end-cap toroids, bend the muon tracks to gain information on the muon momentum. The detector efficiency for muons in all the detectors is at minimum 90%.

Central Muon detectors

The gas mixture is chosen to produce enough avalanche electrons and to remove the remaining space charge as fast as possible. A new mixture – 80% argon, 10% CF_4, 10% CH_4 – gives a maximum drift time of 450 ns.

Spanning the region $|\eta| \leqslant 1$ the wide angle muon spectrometer, WAMUS, consisting of three layers of proportional drift tubes parallel to the beam axis measure the arrival time of the muon and the z position of the hit. One layer is placed before the central toroid, the other two after the coils.

---

[6] **L**ight **e**mitting **d**iodes

Right before the first WAMUS layer a scintillation detector is placed for track matching for muons with low transverse momentum down to 1.5 GeV/c with the inner detector data and trigger purposes.

Two additional layers of scintillation counters, one on the outer detector surface and one at the bottom of the detector, with a small pitch in ϕ, provide additional information on muon tracks and allow for the rejection of cosmic muons.

Forward Muon detectors

In the forward region $1 \leqslant |\eta| \leqslant 2$ the old proportional chambers were replaced by mini drift tubes with an internal cross section of 10 mm × 10 mm and a drift time of 60 ns.

Two layers of mini drift tubes are placed outside, one inside the toroids. Each of the drift tube layers is accompanied by a scintillation counters with a resolution of $\Delta\phi \times \Delta\eta = 0.08 \times 0.1$.

As in the case of the WAMUS system the scintillation counters give information for tracking and on muons with low transverse momentum.

3.3 The ATLAS Detector

3.3.1 Overview of the ATLAS detector layout

The ATLAS detector [43] will be one of the LHC multi-purpose experiments. It is about the size of a five story building, 46 meters in length and 20 meters in height.

The ATLAS detector layout resembles the DØ layout in many ways, only partly owing to the fact that both are multi purpose apparatus. In a wider sense DØ is a test bed for some of the technologies used in ATLAS, the liquid argon calorimetry and the muon spectrometers might serve as examples.

3.3.2 The ATLAS Inner Detector

The inner detector is housed in a cylindrical cavity of 7 meters length and about one meter radius is and surrounded by a two Tesla super-conducting solenoid magnet.

The ATLAS inner detector makes use of three different detector systems, the pixel detector, the silicon tracker and the transition radiation tracker.

All three detector components are only sensitive to charged particles. The former two are placed closest to the beam-pipe and provide a high spatial resolution, the latter one shows less spatial resolution but instead gives access to a high number of points per particle tracks.

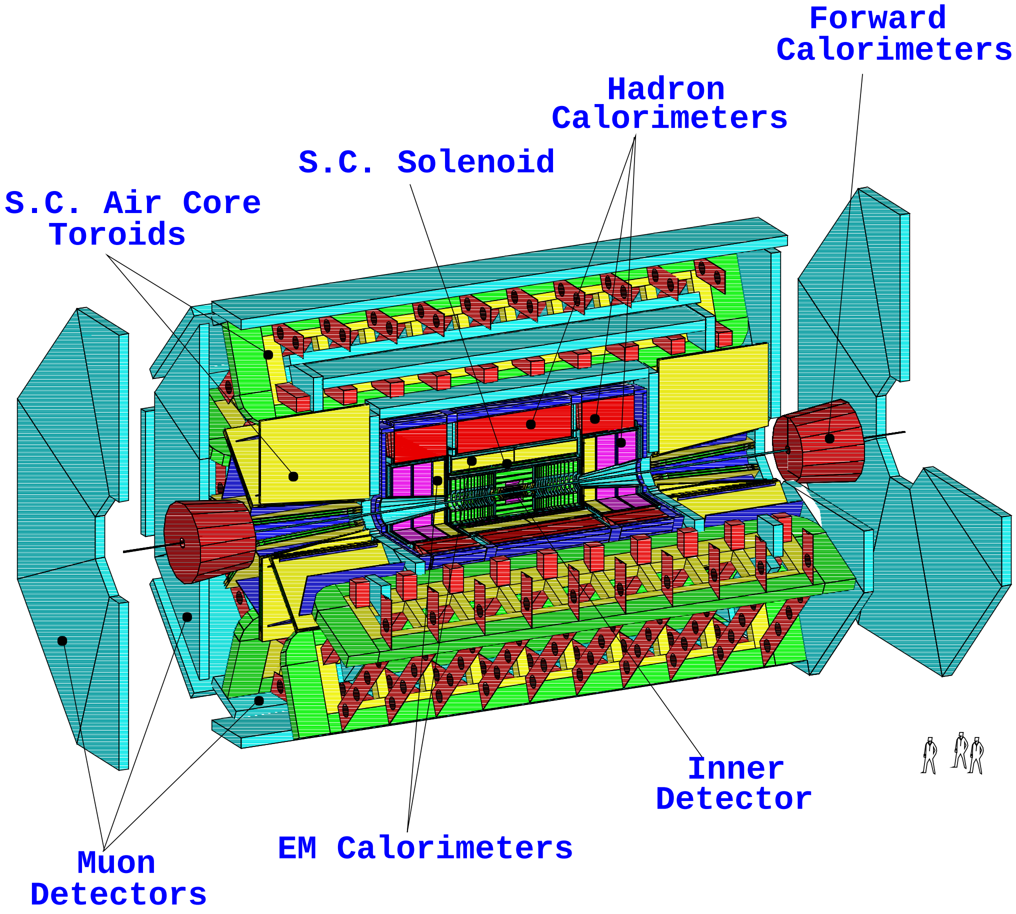

Figure 3.5: *Schematic view of the ATLAS detector*

The Pixel Detector

The pixel detector spans over a range of $|\eta| \leqslant 2.5$. Instead of microstrip detectors as in the case of the DØ silicon vertex detector it is based on semiconductor detectors with a two dimensional segmentation called pixel sensors.

A barrel part of three layers of pixel sensors and an end part with five concentric disks on each side of the barrel layers can be distinguished.

The innermost barrel layer can be removed for the replacement of detector parts damaged by irradiation – the sensors have to withstand ionising radiation of 300 kGy. The remaining two layers have a coverage of $|\eta| \leqslant 1.7$. In the barrel region a resolution of 12 μm in $r \times \phi$ and of 66 μm in the z-direction are achieved.

A resolution in $r \times \phi$ comparable to the barrel part is obtained for the disks which also give information on the r-coordinate with a resolution of 77 μm. The disks span a region of $1.7 \leqslant |\eta| \leqslant 2.5$.

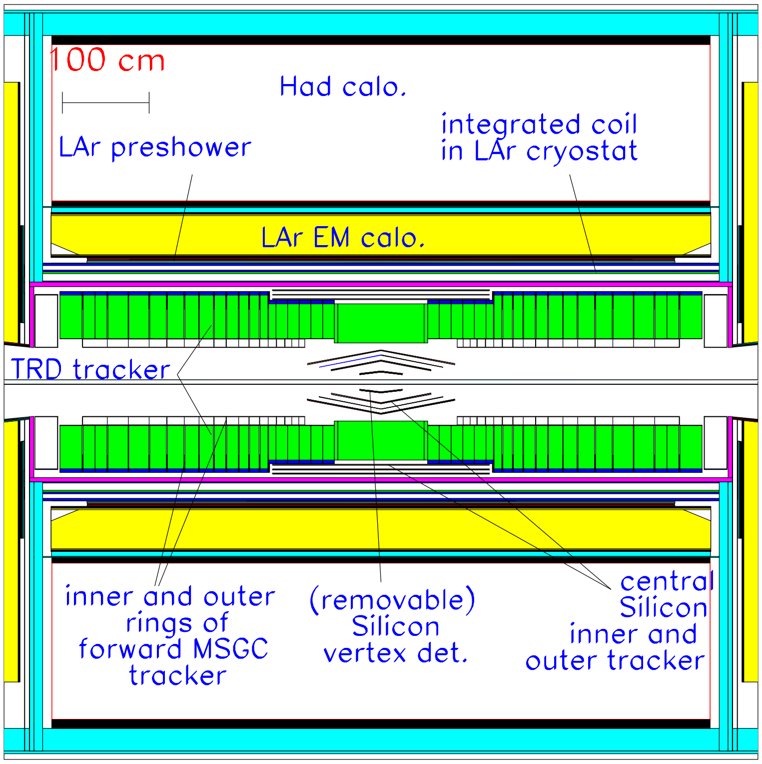

Figure 3.6: *Side view of the ATLAS Inner Detector*

The Silicon Tracker

The silicon tracker is sensitive up to $|\eta| \leqslant 2.5$; like the pixel detector it is subdivided in a barrel and an end-cap part. The tracker uses silicon microstrip detectors (see the description of the DØ silicon vertex detector on page 56).

In the barrel part eight layers of detectors, alternately shifted under a small stereo angle, provide precision measurements in r, ϕ and z. Four barrel modules, each containing two layers, with a maximum outer radius of 0.52 m enclose the pixel detector. Extending to each side, away from the barrel part, the disk modules reach from $|\eta| = 1.4$ to$|\eta| = 2.5$.

Both barrel layers and disks have a resolution of 16 μm in r $\times$ ϕ, the barrel z coordinate is measured to an accuracy of 580 μm. Like the pixel detector, the silicon tracker gives information on track points, vertex position and momentum. Additionally pattern recognition algorithms can distinguish particles by their hit patterns.

The Transition Radiation Tracker

Surrounding the silicon tracker the transition radiation tracker spans the range of $|\eta| \leqslant 2.5$. Its spatial resolution in z is 170 μm and it gives access to a large number of track points, typical thirty and more.

The transition radiation tracker is build of straw detectors. A straw detector is a small tube filled with gas and a wire in the middle. Between the mantle of the tube and the wire high voltage is applied. If a charged particle passes the tube it ionises the gas. The ions and electrons are collected and induce a signal in the straw.

Fast detector response is essential in the LHC environment because of temporal pile up. The small diameter of the straw tubes allows for hit rates of several megahertz since charges inside the gas volume are collected fast.

Seventy percent of the straw tube gas is Xenon, which makes it possible to detect transition radiation [44]. Transition radiation is a threshold effect occurring when a particle traverses an inhomogeneous medium and is dependent on the relativistic velocity p/m of the particle. Transition radiation is peaked forward in the direction of the particle track and is observed for $\beta\gamma \approx 1000$.

Transition radiation photons produce electrons and positrons inside the detector which can be detected in the straw tubes. A signal threshold for the straw tube signal can help to distinguish transition radiation signals from signals caused by ionisation, the former producing a more intense signal than the latter.

Since transition radiation is observed for particles with high $\beta\gamma$ it can be exploited to distinguish light particles from heavy particles. In the transition radiation detector this is done for electrons and hadrons.

The transition radiation tracker has a barrel part with axial straws reaching to $|\eta| \leqslant 0.7$ and two end cap parts with radial straws covering the range of $0.7 \leqslant |\eta| \leqslant 2.5$.

3.3.3 The ATLAS Calorimeters

The ATLAS calorimeter system uses the liquid argon and scintillators as active media. For the ATLAS detector electromagnetic and hadronic calorimeter are separated systems, both divided into a barrel and an end-cap part [49]. Preshower detectors and a supplementary forward calorimeter complete the calorimeter system.

The Electromagnetic Calorimeter

The barrel part of the electromagnetic calorimeter reaches up to $|\eta| = 1.475$, the end-cap part from $|\eta| = 1.375$ to $|\eta| = 3.2$. The entire electromagnetic calorimeter system is confined in a cryogenic system of 13 meters length and 2 meters radius consisting of separate cryostats for the barrel part and the end-cap parts. Its energy resolution is given by

$$\frac{dE}{E} = \frac{0.1}{\sqrt{E}} \oplus 0.07, \quad [E] = GeV$$

Barrel and end cap calorimeter are subdivided in sampling areas with different granularity. In the region of low pseudorapidity ($|\eta| \lessapprox 2$) a finer granularity was chosen than for higher values of η since the physical processes of interest at LHC produce central event signatures as in the case of associated Higgs production.

A typical resolution for the electromagnetic calorimeter in the low η region is $\Delta\eta \times \Delta\phi \approx 0.003 \times 0.1$, for higher values of pseudorapidity the resolution decreases to 0.1×0.1. The highest resolution in both η and ϕ achieved in the central region is $\Delta\eta \times \Delta\phi = 0.025 \times 0.025$.

The electromagnetic calorimeter is a sampling liquid argon calorimeter with a thickness of 24 to 26 radiation lengths. Lead absorbers interleave the active liquid argon parts which have a width of about 2 mm.

For particle energies higher than 20 GeV the relative energy resolution is better than 0.03 and the time resolution is $(1.2/\mathrm{E} + 0.25)\mathrm{ns}, [\mathrm{E}] = \mathrm{GeV}$.

In front of the barrel and end cap part a presampler calorimeter, one active liquid argon layer with a granularity of $\Delta\eta \times \Delta\phi = 0.025 \times 0.1$ is added where the amount of material placed before the electromagnetic calorimeter exceeds two radiation lengths ($|\eta| \leqslant 1.8$).

In the gap between the barrel calorimeter and the end cap calorimeter cryostat a scintillator slab complements the presampler.

The Hadronic Tile Calorimeter

The hadronic tile calorimeter consists of two barrel parts. It is a sampling calorimeter with tiles of scintillators placed between lead absorber plates. The first barrel covers the region $|\eta| \leqslant 1.0$, the second extends to both sides from $|\eta| = 0.8$ to $|\eta| = 1.7$. The energy resolution is given by

$$\frac{dE}{E} \approx \frac{0.4}{\sqrt{E}} \oplus \frac{2}{E} \oplus 0.018, \quad [E] = GeV$$

Scintillation light coming from hadronic shower particles is taken as a measure for the particle energy.

The inner radius of the hadronic tile calorimeter is about 2.3 m, the outer about 4.3 m and has a length of 12 meters.

The Hadronic Liquid Argon Calorimeter

The end cap system of the hadronic calorimeter, the hadronic liquid argon calorimeter, is composed of four wheels, two on each side of the hadronic tile calorimeter barrel with an outer radius of 2 m. They are confined in the same cryostat used for the forward electromagnetic calorimeter.

Liquid argon sampling technology, similar to the electromagnetic calorimeter setup, with copper plate absorbers for shower initiation will be used for the end-cap calorimeter.

The end-cap calorimeter reaches from $|\eta| = 1.5$ up to $|\eta| = 3.2$, at a pseudorapidity value of 2.5 the granularity becomes coarser, changing from a granularity of $\Delta\eta \times \Delta\phi = 0.1 \times 0.1$ to $\Delta\eta \times \Delta\phi = 0.2 \times 0.2$.

The energy resolution for pions in the liquid argon end-cap calorimeter is similar to that of the barrel part.

The Hadronic Liquid Argon Forward Calorimeter

Supplementing the hadronic end cap calorimeter is the forward calorimeter, placed near the inner cryostat walls left and right from the interaction point after the end cap calorimeter. The energy resolution is given by The energy resolution is given by

$$\frac{dE}{E} \approx \frac{0.27}{\sqrt{E}} \oplus \frac{1.7}{E} \oplus 0.04, \quad [E] = GeV$$

The layout of the forward detector is different to the other liquid argon calorimeters. In the region $3.1 \leqslant |\eta| \leqslant 4.9$ covered by the forward calorimeter the level of radiation is very high. Constraints in size set by the limited space available in the cryostat call for a dense, radiation hard design.

To fulfill this limitations the forward calorimeter is subdivided in three sections, each section consisting of a metal matrix with regularly spaced longitudinal channels filled with concentric rods and tubes.

Filling the space between the tubes and the rods the liquid argon is confined in a gap of about 0.25 to 0.38 mm. The rods are at a positive voltage while matrix and tubes are grounded.

With this design a granularity of $\Delta\eta \times \Delta\phi = 0.2 \times 0.2$ was achieved. The full hadronic calorimeter including the forward calorimeter has a thickness of about ten nuclear interaction lengths. Like the electromagnetic calorimeter its fine granularity at low values of pseudorapidity and good energy resolution help to measure the energy and angular distribution of jets.

3.3.4 The ATLAS Muon spectrometer

The muon spectrometer defines the outer layer of the ATLAS detector. Four different chamber technologies are used in the muon spectrometer. Muon identification, momentum measurement and tracking impose constraints on the spatial resolution. Furthermore the muon spectrometer will be used to derive a bunch crossing signal, requiring a detector response time shorter than the LHC bunch spacing of 25 ns.

In the inner part of the muon spectrometer a super-conducting air-core toroid magnet, supplemented by two end cap toroids, bends the muon tracks and allows for a determination of the transverse muon momentum.

The Muon Barrel Chambers

Covering the pseudorapidity range $|\eta| < 1$ three concentric cylinders of chamber modules define the muon barrel spectrometer. The innermost layer is placed inside the field volume of the toroid magnet, the other two near the inner and outer boundaries of the magnetic field.

The basic elements of the muon barrel chamber are drift tubes built of aluminium tubes with a diameter of 3 cm filled mainly with argon gas and a central wire of 50 μm diameter. The drift tubes work similar to the proportional drift tubes (see section 3.2.4 on page 59) with a single wire resolution of 80 μm[7] and are aligned perpendicular to the beam axis.

One muon chamber typically consist of 2x4 mono-layers of drift tubes in the inner barrel part and 2x3 mono-layers in the outer part respectively. A maximum drift time of 700 ns could be obtained. The muon identification efficiency is greater than 90 % for a single muon.

A resistive plate chamber is placed on top of each monitored drift tube chamber. A resistive plate chamber is made of two parallel resistive plates with a uniform electric field between. Each plate is subdivided by insulated strips. In between the plates an ionisable gas is added.

The electric field strength for the resistive plate chamber is 4.5 kV/mm. If a traversing particle ionises the chamber gas, an electron avalanche is created, resulting in an intense charge signal of typically 5 pC.

The resistive plate chambers work as a muon trigger with a spatial resolution of 1 cm and a response time of about 1 ns. Two layers of strips, one parallel to the beam axis and one orthogonal provide a measurement of a muon hit in both coordinates η and ϕ.

The Muon End-cap Chambers

The muon end cap spectrometer consists of four wheels of monitored drift tube chambers covering the range $1 < |\eta| < 2.7$. The drift tube chambers are comparable in spatial resolution and drift time to the barrel chambers. They are positioned perpendicular to the beam axis and allow for a measurement of the muon track coordinates in the (r, ϕ) plane.

All wheels are placed outside the field region of the toroid magnet, limiting the capability for momentum measurements.

In between the wheels thin gap chambers are added as trigger detectors. A thin gap chamber contains an ionisable gas confined between two cathode plates.

In the middle of the chamber equidistant wires serve as anodes and collect electrons liberated by ionisation due to a charged particle crossing the chamber. As in the case of proportional drift tubes an electron avalanche near the wires amplifies the collected signal.

The distance between the cathode plates of the ATLAS thin gap chambers is about 2.8 mm and the operating voltage is 3 kV. With this configuration a drift time smaller than the LHC bunch spacing can be achieved.

The anode wires are arranged parallel to the drift tube wires with a pitch of less than 2 mm, the electrodes are segmented orthogonal to the wires, giving trigger information in both r and ϕ.

In the innermost plane over $2 < |\eta| < 2.7$ cathode strip chambers, similar to the thin gap chambers but with a higher granularity, are added to the muon

---

[7] To achieve such a good resolution the mechanical uncertainties in the spectrometer must not exceed 30 μm– extensive tests of the drift tubes and the chamber modules are therefore needed [50].

system. The cathode gap chambers can withstand the demanding rate of muons in the forward region.

3.4 Comparing DØ to ATLAS

This section gives a comparison of both detectors DØ and ATLAS with emphasis on some of the detector requirements listed in section 3.1 on page 49.

The values listed in the following text serve as an input to the ATLFast detector simulation. A list of the ATLFast parameters for both DØ and ATLAS can be found in appendix C.

3.4.1 Particle Identification

For particle identification, tracks and calorimeter clusters are required. A track is a subsequent number of point measurements of particle hits which can be connected to form a continuous path.

A calorimeter cluster is reconstructed using several cells – independent regions of the calorimeter defined by position and size in the $(\eta \times \phi)$ plane. Cluster reconstruction starts with a single initiator cell, a part of the calorimeter where a high signal was measured. A threshold energy is specified to distinguish an initiator cell from other cells.

Cells containing lower energy hits are added to the initiator cell, forming a cluster. The cluster radius given by $\mathrm{R} = \sqrt{(\Delta\eta)^2 \times (\Delta\phi)^2}$ defines the cluster size, its energy is the sum of the energy deposits measured in the individual cells.

The isolation radius determines the minimum distance in the (η, ϕ) plane for two clusters to be identified as separate.

Both track and cluster reconstruction incorporate ambiguities.

3.4.2 Identification of leptons

Identification of leptons with the DØ detector

In the case of the DØ detector, electrons are identified using calorimeter signals from the electromagnetic calorimeter and the preshower detectors by matching them with tracks from the tracking system. An electron can be reconstructed if its transverse momentum is greater than 2.0 GeV/c.

In the central region $|\eta| \leqslant 1.6$ a signal in the central preshower detector is matched with a track for a particle with transverse momentum greater 5 GeV/c and a calorimeter cluster with an energy greater 7 to 10 GeV. For an electron the isolation radius is less than 0.2 [51].

In the forward region up to $|\eta| = 2.6$ no track information is required, the constraints on transverse momentum and isolation radius are the same as those for the central region.

Subsequent analysis steps [52] lead to an electron identification efficiency greater 95 % for electrons with a transverse momentum greater 5 GeV/c in the region $|\eta| \leqslant 2.6$.

Muons are reconstructed utilizing track information coming from the scintillating fiber tracker and muon spectrometer data [53].

A track is matched with hits in the scintillation detectors of the muon spectrometer. In the next step the hit patterns inside the scintillators and the drift tubes are compared. The signal timing in the different detector parts rejects muons coming from background processes such as cosmic muon showers.

The lower limit to the transverse momentum of reconstructed muons is 1.5 GeV/c. Taking into account material outside the toroid magnet and typical trigger rates the minimum transverse momentum becomes 8.0 GeV/c in pseudorapidity range $|\eta| \leqslant 2$.

A muon is conservatively taken to be isolated if there are no more than two charged particles in an isolation radius of 0.5 around the muon track. For the ATLFast detector simulation used in this thesis (see section 4.2.2 on page 80) an isolation radius of 0.2 was chosen according to results from detector simulations [54].

Hadronically decaying taus are detected by their decay products, mainly neutral pions. The main information for the tau reconstruction is obtained in the electromagnetic and hadronic calorimeter. In addition information gathered from the inner detector can help to identify tracks coming from charged taus.

Taus with a transverse momentum greater 5 GeV/c can be reconstructed up to a pseudorapidity value of 1.5. The initiator cell energy for a tau tagged cluster in the calorimeter is 2 GeV/c [55] and the isolation radius of 0.4 was chosen according to [56].

Identification of leptons with the ATLAS detector

Electrons are reconstructed with the ATLAS detector using data from the inner detector and the electromagnetic calorimeter. For electrons with a transverse momentum less than 7 GeV/c the electron track is extrapolated to the electromagnetic calorimeter. At its crossing point with the calorimeter a local cluster search is initiated.

For electrons with higher p_T it is possible to match calorimeter clusters and tracks and the discrimination of electron and jet signals become important.

Electrons can be reconstructed with an efficiency greater 90 % for pseudorapidity values less than 2.5 and a transverse momentum greater than 5 GeV/c. An electron is taken to be isolated if its distance to other particles in the (η, ϕ) plane is greater than 0.4 [**?**].

Muon reconstruction exploits information coming from the inner detector and the muon spectrometer. Muon track points are measured in both the spectrometer and the inner detector and can be combined to a complete muon track penetrating the full detector volume.

In comparison to DØ ATLAS is able to identify muons with a lower transverse momentum ($p_T \leqslant 6$ GeV/c, instead of $p_T \leqslant 6$ GeV/c) within a region $|\eta| \leqslant 2.5$ at an efficiency greater 90 %.

The ATLAS tau lepton reconstruction algorithm for a hadronically decaying τ differs from the DØ algorithm. Instead of the flavour content the lateral shower size and the number of particle tracks contained in a jet are used as discriminating variables. This choice was based on the fact that tau jets include only a small number of particle tracks and are collimated in the direction of the tau lepton track.

Tau identification is possible for tau jets with $p_T \leqslant 10$ GeV/c and $|\eta| \leqslant 2.5$. If the LHC is working at low luminosity, an isolation radius of 0.3 is appropriate to safely separate tau jets from other particle tracks.

3.4.3 Identification of jets

Jet reconstruction is based on data taken with the hadronic calorimeter system and involves the choice of an adequate jet finder algorithm[8].

In view of the jet reconstruction used (see section 4.2.2) to reconstruct a jet in a certain pseudorapidity region is given. In the case of DØ an identification of jets with $E \geqslant 10$ GeV within $|\eta| \leqslant 2.5$ [57].

At ATLAS jets can be identified within a pseudorapidity region $|\eta| \leqslant 5.0$. The energy threshold is the same as for DØ.

3.4.4 Identification of b-jets

B-tagging at DØ and ATLAS is based on impact parameter measurement and secondary vertex reconstruction as described in section 3.1.8 on page 53.

Studies for b-tagging with soft leptons for DØ show good progress [58]. This also holds for the ATLAS detector [43].

At DØ and ATLAS b-tagging is possible for all reconstructed jets. Parameterizations of the b-tagging efficiency for both detectors are given in section 5.1.5 on page 90.

3.4.5 Summary

The ATLAS detector is designed for event detection at high luminosities. Its performance outranges the DØ performance in most cases. Nevertheless parameters important for the analysis are comparable. Differences can be found for the acceptance region for lepton identification, jet energy resolution and b-tagging efficiency – for which the ATLAS detector performance is found to be better.

---

[8] see **??** for details on jet finder algorithms

Chapter 4

Event generation and detector simulation for DØ and ATLAS

4.1 Monte Carlo generation using Pythia

4.1.1 Introduction

Table 4.1: **Monte Carlo generation – Number of events**

Process	DØ	ATLAS	Comment
Z^0H	100000	100000	$m_H = 90, 115, 120, 125, 130$
$W^{\pm}H$	100000	100000	$m_H = 90, 115, 120, 125, 130$
$b\bar{b}$	350000	350000	
$t\bar{t}$	300000	300000	$W^{\pm} \to$ anything
$W^{\pm *} \to tb$	150000	150000	$\sqrt{\hat{s}} \geqslant m_t + m_b$
tqb	150000	150000	
$Z^0b\bar{b}$	300000	300000	full Z^0/γ^* propagator
$W^{\pm}b\bar{b}$	300000	300000	
Z^0Z^0	150000	150000	
$W^{\pm}Z^0$	150000	150000	

Number of events generated for signal and background processes.

Signals and backgrounds[1] have been produced especially for this study.

The newest version of the Pythia [59] Monte Carlo event generator (Pythia 6.203) was used to generate comparable event samples for both the Tevatron

---

[1] See 1.2 and 1.3 for a theoretical treatment of signals and backgrounds including the leading order Feynman Diagrams.

and LHC center of mass energy and common settings were retained for both environments, see appendix A.

Furthermore the backgrounds $W^{\pm}b\bar{b}$ [60] and $Z^0b\bar{b}$ [61] were added to PYTHIA as external user processes.

In all cases high statistics of the order of 10^5 events were available, though some compromises had to be made due to computation time and disk space. Table 4.1 lists the numbers of events generated for the signal and background processes.

The decision to generate a certain number of events was guided by the size of the cross section for each process. In all cases the background processes have a bigger cross section than the signal and it is not possible to mirror the ratio of cross sections in the ratio of events as can be seen from tables 4.4 and 4.5.

As a compromise a minimum factor of 1.5 more events were produced for the background processes.

In the subsequent analysis two independent detector simulations were executed. Since both rely on the same event generator data this information was stored to disk and read out again by the detector simulations. The storage needed for the event generator data was the limiting factor for the event sample sizes.

The generation of the event samples was thus held independent of the detector simulation and the same data could be made available to both simulations.

4.1.2 Production of Monte Carlo samples for different Higgs boson masses

The lower bound to the Higgs boson mass is given by recent LEP results[2]. For Higgs boson masses higher than $2m_{W^{\pm}}$ the decay $H \rightarrow W^{\pm}W^{\pm}$ is dominant. At a Higgs mass of 135 GeV/c^2 the WW^* decay mode becomes dominant.

For reasons of comparability with [25] and [62, 63] the lowest mass value was chosen as 90 GeV/c^2. Two additional mass fix-points, 120 GeV/c^2 and 130 GeV/c^2, coincide with the values chosen for the TEVATRON and ATLAS analysis.

Another two intermediate values, 115 GeV/c^2 and 125 GeV/c^2, were added to have a smooth coverage of the mass range set by the LEP measurements [1] and the region of interest for the TEVATRON.

---

[2] See section 1.1.5 on page 25

4.1.3 Selection of decay channels

Table 4.2: **Restrictions on the decay channels set for different Monte Carlo samples**

Process	Decay channels	Comment
Z^0H	$Z^0 \to l^+l^-, l = e, \mu, \tau$ $H \to b\bar{b}$	
$W^{\pm}H$	$W^{\pm} \to l^{\pm}\nu, l = e, \mu, \tau$ $H \to b\bar{b}$	
$b\bar{b}$	–	no decay restrictions
$t\bar{t}$	$t \to W^{\pm}b$	
$W^{\pm *} \to tb$	$W^{\pm *} \to tb$ $t \to W^{\pm}b$ $W^{\pm} \to l^{\pm}\nu, l = e, \mu, \tau$	
tqb	$t \to W^{\pm}b$ $W^{\pm} \to l^{\pm}\nu, l = e, \mu, \tau$	
$Z^0b\bar{b}$	$Z^0 \to e\bar{e}$ $Z^0 \to \mu\bar{\mu}$ $Z^0 \to \tau\bar{\tau}$	exclusive sample of 100000 events exclusive sample of 100000 events exclusive sample of 100000 events
$W^{\pm}b\bar{b}$	$W^{\pm} \to e\nu_e$ $W^{\pm} \to \mu\nu_{\mu}$ $W^{\pm} \to \tau\nu_{\tau}$	exclusive sample of 100000 events exclusive sample of 100000 events exclusive sample of 100000 events
Z^0Z^0	$Z^0 \to l^+l^-, l = e, \mu, \tau$ $Z^0 \to b\bar{b}$	
$W^{\pm}Z^0$	$W^{\pm} \to l^{\pm}\nu, l = e, \mu, \tau$ $Z^0 \to b\bar{b}$	

List of the decay channels selected for the different Monte Carlo samples.

The final states for the processes $W^{\pm}H$ and Z^0H include leptons of all three flavours. Thus the production of inclusive samples with all three lepton flavours was chosen in the Monte Carlo generation. In the analysis electrons and muons are treated in the same way and the lepton flavour is not taken into account.

Nevertheless some differences occur with regard to tau leptons. Tau leptons decaying into hadrons are treated as jets by the detector simulation. As a consequence a misidentification of the jet flavour reduces the number of reconstructed taus.

If a tau lepton decays into lighter leptons, electrons or muons, these leptons are not identified as originating from a tau decay by the detector simulation. Instead they are considered as direct decay products of the associated gauge boson. Since the light leptons only carry a part of the momentum of the primary tau lepton, including these leptons can alter the distribution of lepton momenta.

This effect is reduced by the requirement that the leptons entering the analysis are isolated, because a lepton coming from a tau decay is often accompanied by other particles and therefore rejected.

The selected decay channels included in the different Monte Carlo samples can be found in table 4.2 on the preceding page. The table only lists the extra restrictions imposed on the particle decay, if a channel is left out this means that the particle in question is not limited in its decay.

In the case of the $W^{\pm}b\bar{b}$ and $Z^0b\bar{b}$ background processes separate samples for each lepton flavour were produced.

Since the process labelled $t\bar{t}$ includes backgrounds to both signal processes an inclusive sample was produced. The $W^{\pm}$ boson was not restricted to decay leptonically, which would be the favoured option if only the final state with two leptons – as indicated on the left hand side of figure 1.6 on page 32 – was considered.

Instead the sample also includes those decays relevant for the comparison with the $W^{\pm}H$ final state. Taking into account table 4.3, the branching ratio for the non-leptonic decay of the $W^{\pm}$ is about 68%. If both bosons created as intermediate particles in the $t\bar{t}$ process decay hadronically, the final state is different from both signal final states. Thus about 46% of the sample are discarded. Only about 10% of the whole sample are relevant as background to the Z^0H signal while the remaining 22% resemble the final state of the $W^{\pm}H$ signal.

No branching ratio is given for the decay of the Higgs boson to a bottom quark-anti-quark pair, because only this decay is considered. For the top quark decaying into a $W^{\pm}$ boson and a bottom quark the branching ratio given by PYTHIA is listed since the top quark branching ratios have not yet been measured in full detail.

The branching ratios given by [2] differ from those used by the PYTHIA Monte Carlo generator. For reasons of comparison the PYTHIA branching ratios relevant for the analysis are listed in appendix B on page 142.

4.1.4 Additional Pythia settings

Where available the standard PYTHIA process selection scheme has been followed in the generation of the Monte Carlo samples, nonetheless some additional settings were necessary to produce the desired final states.

The processes $W^{\pm}b\bar{b}$ and $Z^0b\bar{b}$ have not yet been available in PYTHIA (January 2002), and their contribution to the background could only be estimated in former analysis [25, 62, 63]. For this thesis a new external library [60, 61] to the PYTHIA Monte Carlo generator was available for PYTHIA version 6.1.

Table 4.3: **Branching ratios**

Decay channel	Branching ratio [2]
$\mathrm{H} \to \mathrm{b\bar{b}}$	depends on $\mathrm{m_H}$
$\mathrm{Z}^0 \to \mathrm{e\bar{e}}$	$(3.367 \pm 0.005)\%$
$\mathrm{Z}^0 \to \mu\bar{\mu}$	$(3.367 \pm 0.008)\%$
$\mathrm{Z}^0 \to \tau\bar{\tau}$	$(3.371 \pm 0.009)\%$
$\mathrm{Z}^0 \to \mathrm{l^+l^-}, \mathrm{l} = \mathrm{e}, \mu, \tau$	$(10.105 \pm 0.004)\%$
$\mathrm{Z}^0 \to \mathrm{b\bar{b}}$	$(15.13 \pm 0.05)\%$
$\mathrm{W}^\pm \to \mathrm{e}\nu_\mathrm{e}$	$(10.66 \pm 0.20)\%$
$\mathrm{W}^\pm \to \mu\nu_\mu$	$(10.49 \pm 0.29)\%$
$\mathrm{W}^\pm \to \tau\nu_\tau$	$(10.4 \pm 0.4)\%$
$\mathrm{W}^\pm \to \mathrm{l}^\pm\nu, \mathrm{l} = \mathrm{e}, \mu, \tau$	$(31.55 \pm 0.15)\%$
$\mathrm{t} \to \mathrm{W^\pm b}$	99.8% (Pythia restriction)
$\mathrm{W}^{\pm *} \to \mathrm{tb}$	depends on $\sqrt{\hat{\mathrm{s}}}$

Branching ratios for the decay channels listed in table 4.2

The interface for the integration of external processes to PYTHIA was changed in version 6.2, which restricted the use of the external libraries to version 6.161. In the following those settings necessary for the integration of the external processes to PYTHIA are described (see also table A.2 in appendix **??**).

In the case of the process $\mathrm{W^\pm b\bar{b}}$ a choice of the mass scale Λ determining the evolution of the strong coupling constant by

$$\alpha_{strong}(Q^2) \propto \frac{1}{\log Q^2/\Lambda^2} \tag{4.1}$$

has to be made. At this scale the coupling α_{strong} becomes strong if Q^2 is decreased. The scale was chosen to be $\Lambda \equiv m^2_{\mathrm{W}^\pm}$, keeping in mind that the heaviest particle produced in this process is the $\mathrm{W}^\pm$boson.

Two options for the $\mathrm{Z^0 b\bar{b}}$ matrix element calculation are available for selection. One can either choose the calculation to include only those terms relevant for the Z^0 propagator or one can select the matrix element to be calculated with the full $\mathrm{Z}^0\gamma^*$ propagator, which gives a better estimate of the cross section and was therefore chosen for the sample generation. In the latter case the lower bound to the mass of the off-shell photon was set to $10\ \mathrm{GeV/c^2} \approx 2\mathrm{m_{bottom}}$.

The process $\mathrm{W}^{\pm *} \to \mathrm{tb}$ has been generated using the standard W^* production process and requiring $\sqrt{\hat{\mathrm{s}}} \geqslant \mathrm{m_{top}} + \mathrm{m_{bottom}}$. This enhances the final tb state.

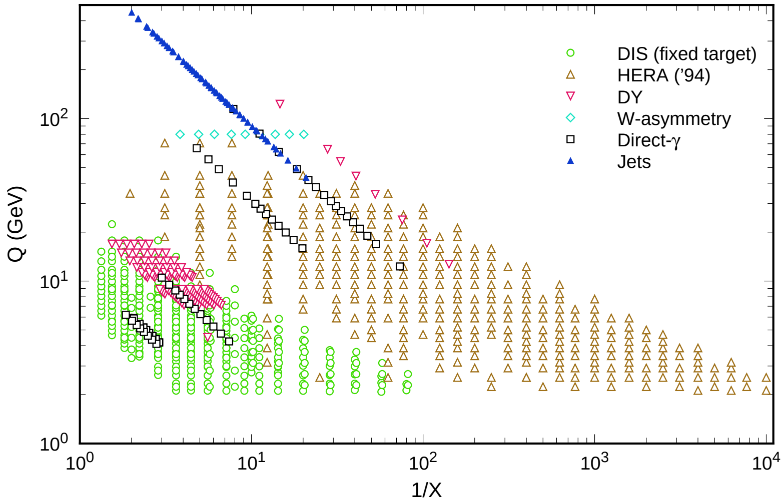

Figure 4.1: *Kinematic map of the experiments used for the CTEQ5M1 parton distribution function [34]*

4.1.5 Choice of a parton distribution function

As was explained in detail in section 2.1 on page 35 the choice of a parton distribution function is crucial for a correct simulation of the physics process generation. As stated in [63] changing the parton distribution function can alter the cross section by upto 20%.

Since two different versions of PYTHIA were used for the event generation the external PDF library supplied by the CTEQ collaboration [34] was linked to PYTHIA.

For this study the CTEQ5M1 parton distribution set was selected which includes next to leading order calculations of hard, non-elastic interaction cross sections, assuming a vanishing quark mass for all quark flavours.

The CTEQ5M1 set includes data from deep inelastic scattering collected with the H1 and ZEUS detectors at the HERA ep collider in 1996 and 1997 – see references in [34] and figure 4.1. Data on inclusive jet production collected by DØ in 1998 was also added to the CTEQ5M1 set as well as other data sets collected by different FERMILAB collaborations.

4.1.6 Cross sections for signal and background processes

Cross sections for signal processes

Table 4.4: **Cross section × branching ratio for the signal process $W^{\pm}H$ and Z^0H obtained from Pythia [fb]**

m_H	Z^0H			$W^{\pm}H$		
	DØ	ATLAS	ratio	DØ	ATLAS	ratio
90	16.6 ± 0.5	149 ± 5	9	91 ± 1	890 ± 10	10
115	6.9 ± 0.1	66 ± 1	10	36 ± 1	390 ± 10	11
120	5.6 ± 0.1	55 ± 1	10	29 ± 1	320 ± 10	11
125	4.5 ± 0.1	44 ± 1	10	22 ± 1	260 ± 10	12
130	3.4 ± 0.1	34 ± 1	10	17.5 ± 0.8	199 ± 9	11

Cross sections for the signal processes $Z^0+H \rightarrow l^+l^-+b\bar{b}$ and $W^{\pm}+H \rightarrow l\nu_l+b\bar{b}$. The fourth and the seventh column list the ratio ATLAS/DØ.

The cross sections for the signal process $W^{\pm}H$ and Z^0H are listed in table 4.4. The errors are obtained from the spread of repeated PYTHIA runs. In each run 10000 events were produced, the maximum error is less than 5 % for all cross section values, including the background cross sections.

For higher Higgs masses the cross section decreases by more than a factor of five. This is caused by the decrease of the branching ratio for the decay $H \rightarrow b\bar{b}$.

A factor of ten in the cross section is gained, changing the center of mass energy energy from 1980 GeV to 14 TeV. Having a look at table 4.5 on the next page one can see that the background processes do not scale with the same factor, instead the factor ranges from about ten up to over one hundred.

The cross sections obtained in this study for the signal processes were found to be in agreement with [63] – referring to a center of mass energy of 14 TeV – but found to be smaller by a factor of 1.5 to 2 if compared to [25] for a center of mass energy of 2 TeV.

Cross sections for background processes

A list of cross sections for all background processes can be found in table 4.5 on the following page. The expected integrated luminosities for both TEVATRON and LHC are stated in units of fb^{-1} – see table 2.1 on page 48 – hence the cross sections are listed in units of fb, although some processes exceed this scale by several orders of magnitude.

At first glance the most dominant background is found to be the $b\bar{b}$ process, which includes all relevant QCD processes leading to a final state with two b-jets. As pointed out in section 1.3.1 on page 29 this background is only relevant if isolated leptons are reconstructed by the detector simulation, thereby faking a signal signature.

Table 4.5: **Cross section × branching ratio for the background processes $W^{\pm}H$ and Z^0H obtained from Pythia [fb]**

Process	DØ	ATLAS	ratio
$b\bar{b}$	$(4.5 \pm 0.1) \times 10^{10}$	$(3.4 \pm 0.1) \times 10^{11}$	7.6
$t\bar{t}$	6600 ± 100	$(6.6 \pm 0.1) \times 10^{5}$	100
$W^{\pm *} \to tb$	3200 ± 100	$(3.6 \pm 0.1) \times 10^{4}$	11
tqb	610 ± 10	$(7.8 \pm 0.1) \times 10^{4}$	130
$Z^0b\bar{b}$, $Z^0 \to e\bar{e}$	710 ± 10	$(3.7 \pm 0.1) \times 10^{4}$	53
$Z^0b\bar{b}$, $Z^0 \to \mu\bar{\mu}$	710 ± 10	$(3.7 \pm 0.1) \times 10^{4}$	53
$Z^0b\bar{b}$, $Z^0 \to \tau\bar{\tau}$	350 ± 10	5500 ± 100	16
$W^{\pm}b\bar{b}$, $W^{\pm} \to e\nu_e$	3100 ± 100	$(4.3 \pm 0.1) \times 10^{4}$	14
$W^{\pm}b\bar{b}$, $W^{\pm} \to \mu\nu_\mu$	3100 ± 100	$(4.3 \pm 0.1) \times 10^{4}$	14
$W^{\pm}b\bar{b}$, $W^{\pm} \to \tau\nu_\tau$	3100 ± 100	$(4.3 \pm 0.1) \times 10^{4}$	14
Z^0Z^0	87 ± 1	850 ± 10	10
$W^{\pm}Z^0$	131 ± 6	1450 ± 70	11

Cross sections for all background processes. The third and the fifth column list the ratio ATLAS/DØ.

A more severe constraint to the analysis is set by the different scaling of the background and signal processes with raising center of mass energy. This is especially relevant in the case of the $Z^0b\bar{b}$ and tqb background processes which increase by a factor of about 50 and 130 respectively.

Taking a closer look at the $Z^0b\bar{b}$ process, a difference in the cross section for the decay channel $Z^0b\bar{b} \to \tau\bar{\tau}b\bar{b}$ to the decays involving lighter leptons is visible. This difference occurs, because the production process $gg \to Z^0b\bar{b}$ does not give enough energy to produce a final state with two bottom quarks and two heavy tau leptons.

In the case of the three-gluon-vertex in figure 1.7 on page 33, the incoming gluon carries a smaller fraction x of the proton momentum than the initial quark in the analogue process, in which a gluon is radiated and splits into two bottom quarks. Thus the intermediate Z^0/γ^* boson is produced off-shell and does not carry enough energy to produce two tau leptons.

The biggest difference in the cross sections for a center of mass energy of 2 TeV was found for the $Z^0b\bar{b}$ and $W^{\pm}b\bar{b}$ process which were underestimated in [25] by factors of four and two respectively. Also differences were found for the other background processes. At 14 TeV the figures quoted in [63] agree with the cross section values obtained in this study.

Note on accepted cross sections

The cross sections for signal and background processes give a first impression of how many particles are to be expected at a center of mass energies of 2 TeV and 14 TeV respectively.

For a direct comparison of the detection capabilities of the DØ and ATLAS detector a characterization of the final state reconstructed by the detector simulations PGS and ATLFAST is needed. These can be found in sections 5.2.1 and 5.3.1.

4.2 Fast detector simulations

For this thesis two fast detector simulations, PGS and ATLFAST were used. A fast detector simulation is not a full detector simulation.

Full detector simulations are based on detailed geometrical models of a detector. Each detector part is described by its three dimensional shape and the matter included in its volume. The full simulation then describes the interaction of the particles with matter and computes the signal output of each detector component. This approach to event reconstruction is slow and requires a lot of computing time.

Fast detector simulations do not attempt to simulate the physical detector response but emulate the detector performance by calculating key values like particle momenta and missing energy within a simple detector model.

Another difference between a fast and a full detector simulation concerns the integration of low-level analysis routines in the fast simulation, namely b-tagging algorithms and jet energy calibration.

In the case of the ATLFAST simulation the user can use the raw detector output as an input to external analysis routines (see sections 5.1.4 and 5.1.5).

In contrast the b-tagging algorithms integrated in the PGS simulation can only be altered by rewriting the code of the PGS package, so only the external jet calibration routines were applied to the PGS data.

In the following two sections an overview of the detector simulations PGS and ATLFAST is given.

4.2.1 The PGS Detector simulation

The PGS – *Pretty Good Simulation* – detector simulation was designed for the Tevatron Run II Higgs/Susy Workshop and was formerly called SHW.

The SHW software is described in detail in [25], thus only the main features of the PGS simulation are mentioned here.

The main objects entering the analysis are called physics objects. These objects include photons, electrons, muons, hadronically decaying taus, jets and heavy stable particles. Additionally it computes the missing transverse energy and the polar angle giving the direction of the missing transverse energy in the (x,y) plane.

A particle is characterized by two separate detector signals emulated in the PGS simulation, its track and its energy deposit in the calorimeter.

A track is reconstructed using the direction of flight stored in the Monte Carlo event record for each charged final state particle. It is assumed to traverse a certain length in a magnetic field. Based on this length and the strength of the magnetic field the original particle momentum is changed by adding a Gaussian smearing to it.

The calorimeter is simulated by two planes in (η, ϕ), subdivided in cells with alike dimensions, one electromagnetic and one hadronic section. The response of each section to a particle penetrating the calorimeter at a certain point in the plane was calibrated using data obtained during the Tevatron Run I.

Each cell contains the energy deposited by the particles. Cells in the electromagnetic and the hadronic section of the calorimeter are connected to give a tower. The cells or towers are combined to clusters (see section 3.4.1 on page 67) for each calorimeter section.

The clusters are characterized by their cone radius which restricts the maximum extension of a cluster in the (η, ϕ) plane. The cluster algorithm is similar to the ATLFAST algorithm, see section 4.2.2 for details.

Jets are reconstructed from clusters using a cone-algorithm similar to that described in section 4.2.2 on page 82. Missing energy is computed performing a vector sum over all calorimeter tower energies.

In the new[3] PGS simulation all lepton directions are calculated in the track finding algorithm and not reconstructed from calorimeter clusters . For further details on the SHW simulation refer to [25].

The PGS simulation can be used to give an estimate of the DØ detector response. It was designed to serve as a fast simulation for both the CDF and DØ detector and does not yet have the flexibility of the ATLFAST simulation. In this study it was intended to use the PGS simulation as a reference to compare with the performance of the ATLFAST simulation.

4.2.2 The ATLFast detector simulation

Different implementations of the ATLFAST detector simulation exist and were tested for this study. The best tested implementation – also used for the studies in the ATLAS technical design report [64] – was the FORTRAN ATLFast package [65]. An obsolete object oriented version was tested but discarded. The ATHENA implementation was still under development and could not be integrated in the analysis.

For the final analysis the FORTRAN ATLFAST[4] simulation package was chosen. This simulation, though still a fast simulation, gives access to a vari-

---

[3] PGS version 3.2

[4] Version 00-02-21

ety of detector parameters and can be configured to resemble the DØ detector performance.

As in the case of the PGS fast simulation calorimeter clusters and tracks are the basic physics identities applied to reconstruct particles and jets, but track reconstruction is optional and is optimized to simulate the ATLAS inner detector response.

Here only those aspects relevant to the reconstruction of leptons, jets and missing energy are briefly discussed, for further details one can refer to [65].

ATLFAST simulates the calorimeter by a plane in (η, ϕ) divided into cells. The size of a single cell can be changed according to the granularity of the calorimeter.

The ATLFast cluster reconstruction algorithm

For all incoming charged particles the effect of the inner solenoid magnetic field is computed and the particle position in ϕ is changed according to the initial particle momentum. Each particle which produces a signal when traversing the cell deposits its energy in the cell.

The cells are scanned if they can be used to initiate a cluster, the threshold for the minimum energy needed to initiate a cluster was set to 1.5 GeV for in the simulation of detectors, DØ and ATLAS.

After selecting all initiator cells, the cluster reconstruction adds those cells to the cluster which are found inside the area defined by the cluster cone radius $R_{cluster}$, half the maximum cell to cell inside the cluster distance in the (η, ϕ) plane.

If all cells are either discarded or added to a cluster each cluster is required to lie within the pseudorapidity range of the calorimeter and to contain a minimum energy, set to 5 GeV in the case of ATLAS and 3 GeV for DØ[5].

Reconstruction of electrons and muons

When all clusters are reconstructed light leptons – electrons and muons – are identified by matching the position of the cluster with the momentum direction of the particles. Again, a cone radius size is set for each particle flavour to decide whether a calorimeter cluster can be coincides with the particles direction.

For both muons and electrons parameterized smearing for transverse momentum, polar angle and pseudorapidity is invoked before the cluster matching.

Additional acceptance criteria, mainly regarding the isolation of electron and muon tracks have to be fulfilled. The isolation radius for electrons and muons, the minimum distance to the nearest cluster, and the minimal transverse momentum needed for reconstruction both enter the detector simulation.

The cone radius, the maximum lateral size of a cluster belonging to an electron or muon, was set to the default values for the simulation of both detectors

---

[5] This value was taken from the PGS detector simulation and is below all thresholds of identification routines.

since these values did not differ comparing the DØ and the ATLAS environment. The electron cone radius was set to $R_e = 0.2$, likewise for muons.

The jet finding algorithm

The standard jet finding algorithm included in the ATLFAST simulation is a cone algorithm. This jet finding algorithm was also used in the TEVATRON Higgs studies. The clusters not associated with electrons, muons or photons are assumed to originate from jets.

Those clusters inside the specified jet cone radius are labelled to belong to the jet, the position of the energy barycenter of all clusters marks the direction of the jet. The cluster energy is smeared according to a Gaussian energy resolution. The jet is reconstructed if the minimum jet energy is exceeded and if it lies inside the pseudorapidity region where jet reconstruction is available.

Clusters belonging to non-isolated particles are added to the jet if they lie inside the jet cone.

Simple flavour tagging

A simple tagging scheme which allows for subsequent parameterized tagging is included in the jet algorithm. If a quark stored in the event record is found in the vicinity of a reconstructed jet – defined by the cluster cone radius $R_{cluster}$ – the jet is labelled with the quark flavour. The quarks selected for this matching algorithm already lost some of their energy in final state radiation processes.

The tagging algorithm takes into account that some of the particles produced in the hadronization of a quark are not collected by the jet finder algorithm. Thus a comparison of the quark direction of flight after final state radiation with the jet direction is more likely to tag the jet flavour correctly.

In the case of hadronically decaying taus, stored in the ATLFAST simulation event record as jets with a tau lepton flavour tag, the quark flavour tagging scheme is adopted, supplemented by the isolation requirement.

To simulate the DØ detector response the variables listed in appendix C on page 143 were set to appropriate values. The jet energy was recalibrated to compensate losses due to final state radiation and fragmentation processes. Finally the tagging scheme was refined employing a p_T dependent tagging efficiency for b-jets and defining the rejection values for light c-jets and hadronically decaying tau leptons.

With this simple flavour assignment the correct jet flavour is assigned and is available in the raw data output. Since this information would not be accessible for real data it just serves as an input to a following parameterized flavour tagging routine simulating the correct detector response (see section 5.1.5 on page 90) on the basis of the preceding flavour assignment performed by the ATLFAST simulation.

Missing energy calculation

The missing transverse energy $\mathrm{E}_{\mathrm{T}}^{\mathrm{miss}}$ is calculated. Unlike the PGS simulation the ATLFast algorithm does not calculate the missing energy by computing the vector sum over all calorimeter clusters. Instead it takes into account the reconstructed cluster information.

Cells not associated to a cluster, clusters not fulfilling the reconstruction constraints, non-isolated leptons not added to any jet cluster are included in the vector sum of all reconstructed particles and jets. This takes into account the parameterized smearing of the particle and jet momenta and gives a more realistic value for the missing energy.

In a final step the missing energy is smeared, applying the jet energy smearing algorithm to the value obtained in the vector sum.

Chapter 5

Analysis

5.1 Reconstruction of events with the fast detector simulations

5.1.1 Physics objects entering the analysis

Monte Carlo data generated with PYTHIA was passed to the different detector simulations by filling the HEPEVT [66] common block, which includes all information on a single event relevant for reconstruction, with the Monte Carlo data stored on disc.

The data processed by the detector simulations was finally stored to disk for later use in the analysis framework. Since the analysis algorithm was designed to be independent of the detector simulation data format a common interface was defined, see section 5.1.2.

The physics objects entering the analysis were:

1. **Particles, namely electrons and muons**

2. **Jets, including hadronically decaying tau leptons and b-Jets**

3. **Missing transverse energy**

Particles are described by Lorentz four momentum vectors, defined by the momentum components in x, y and z-direction[1] and the particle energy. Furthermore the particle flavour is stored, following the Particle Data Group conventions [2] for flavour numbering.

Finally a reference pointing to the original Monte Carlo data from which the particle was reconstructed is added to the particle information.

Jets are stored in the same way as particles. The position of the jet cluster barycenter in the (η, ϕ) plane and its energy give the jet four momentum vector, not taking into account the mass of the quark, gluon or tau lepton belonging to the jet. This mass was set to zero. For the analysis chain jets and other particles

---

[1] According to the coordinate system described in section 3.1.1 on page 49

are stored using the same data format, thus for the analysis a jet entered the list of particles (see section 5.1.3) as a single particle.

Completing the event information the missing transverse energy and the angle ϕ to which it is pointing is stored for later analysis.

5.1.2 Interface to detector simulations

The interface to the detector simulations was determined by the fact that both the PGS and the ATLFast simulation read out the full HEPEVT common block. The Pythia Monte Carlo generator provides a conversion routine, changing the internal Pythia event structure to the HEPEVT structure.

The HEPEVT data was stored to file, for each event up to 1500 particles could enter the detector simulation. In the case of the PGS software no additional conversion was needed to paste the Monte Carlo data to the detector simulation, for ATLFast another internal conversion to the ATLFast event format was required.

Since the full HEPEVT block was needed for the event reconstruction the number of events was limited by the available disk space. After storing the HEPEVT block to disk the files were read out by the different detector simulation programs. The detector simulation output then entered the analysis chain described in the following chapter.

5.1.3 Object oriented analysis software

For the analysis an object oriented analysis framework, written in C++ and based on the Root [67] software package was written. It allows for Monte Carlo generation, detector simulation and analysis in serial order as well as data storage and later analysis in each step of the event production.

The analysis framework Analysis maker is based on a maker structure. A maker structure consists of a process responsible for the execution of subprocesses. Depending on the current state of each subprocess and the data flow the main process selects which subprocess is executed. The order of execution for the subprocesses can depend on the task which has to be performed, for example the process responsible for event generation would be called before the detector simulation reconstruction process. Several tasks, Monte Carlo generation, detector simulation, triggers and cuts as well as data storage and data reading are performed in subsequent order for each event.

The tasks are placed into lists. A common event object, containing the list of particles – including jets – which survived a test (a trigger or a cut imposing constraints on e.g. the particles momentum or pseudorapidity) and additional information like the missing transverse energy found in an event are posted from task to task.

Two main modules, one performing the event generation and one performing trigger, cut and analysis tasks, form the structure of the analysis algorithm. The former is called TAMEventMaker, the latter TAMAnalysisMaker.

TAMEventMaker consists of three lists, one list containing modules for Monte Carlo generation, a second list with modules for the detector simulation and a third one including tasks which allow for direct file access to event information stored into file. This structure allows for the use of different detector simulations with the same Monte Carlo information and the storage of event information on tree level (Monte Carlo generator data) and detector simulation.

For each list the tasks included in the list are performed for a single event in the order set by the user. After all the tasks found in a list are completed, the algorithm switches to the next list.

The analysis module TAMAnalysisMaker consists of four lists. A list for trigger tasks, one for cuts, one list for data fits and one for additional analysis tasks. Trigger and cut tasks are special tasks which are basically tests and can return a true or false value if an event fulfills a constraint or not. If an event does not survive a certain test, later tests are not performed.

There exist special cuts which put constraints on each particle in the list of particles. If a particle does not pass a test it is removed from the particle list, the particles passing the test are handed to the next test which can reduce the number of particles further.

Since many tests, like a cut on the momentum of a particle, are independent of the particle flavour, a well tested number of cuts can be invoked on each particle, including tests on

- the number of particles surviving several tests
- the momentum four vector components $\mathrm{P_x}$, $\mathrm{P_y}$, $\mathrm{P_z}$ and Energy
- the momentum four vector components $\mathrm{P_t}$, η, ϕ, θ

There also exist tests which need the input of two particles. These are tests on

- the difference $\Delta\eta$ in the pseudorapidity of two particles
- the azimuthal angle $\Delta\phi$ between two particle momentum vectors
- the polar angle $\Delta\theta$ between two particle momentum vectors
- the distance $\Delta R = \sqrt{(\Delta\eta)^2 + (\Delta\phi)^2}$ in the (η, ϕ) plane between two particles

Finally tests on event shape variables were integrated in the analysis.

The order of the tests can be chosen by the user. After all tests are performed the data is stored in histograms if the corresponding test was successful. Either one datum per event, for example the number of particles or the missing transverse energy, or one datum per particle in the particle list enters the histogram.

This setup assures that for both the PGS and the ATLFast detector simulation the same Monte Carlo events enter the reconstruction and the same cuts are invoked on the final simulation output.

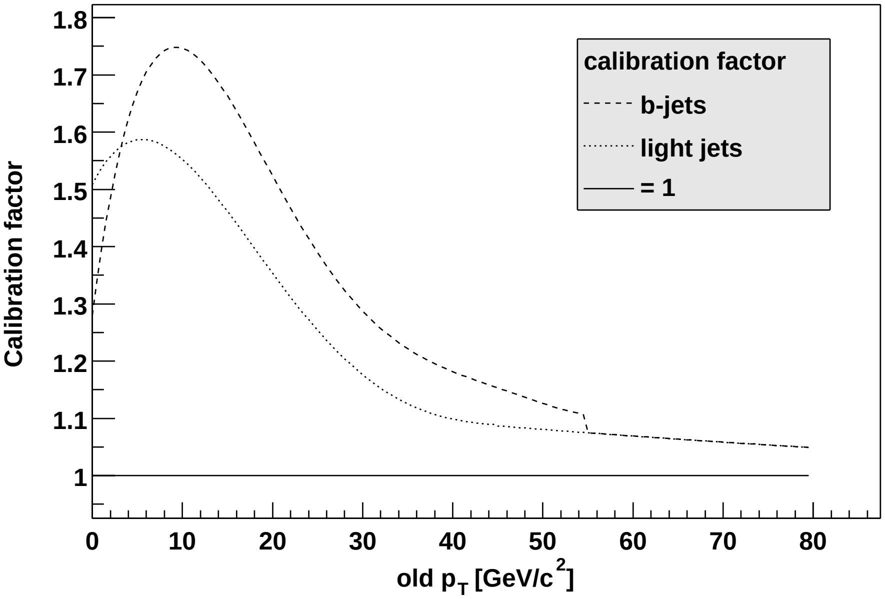

Figure 5.1: *Jet momentum calibration factor for b-jets and light jets*

The full framework is not restricted to the use with Pythia PGS and ATLFast, it can easily be adopted for other Monte Carlo generators and detector simulations by interfacing the event information to the data format given by the simulation in question. Even the event structure itself can be changed, already defined tests do not have to be rewritten. This makes the analysis robust and made the switch from the object oriented ATLFast version to the Fortran version possible.

5.1.4 Calibration of the jet momentum

Both detector simulations reconstruct jets by using a cone algorithm. A reconstructed jet does not resemble the initial quark momentum. For the analysis a calibration of the jet energy allows to reconstruct the peak in the invariant mass spectrum of the two b-jets coming from the decay of the Higgs boson at the Higgs mass.

The calibration was done using the process $W^{\pm}H$ with $H \rightarrow b\bar{b}$, $H \rightarrow u\bar{u}$ and $H \rightarrow gg$ for a Higgs boson mass of $m_H = 100\mathrm{GeV}/c^2$. A detailed description can be found in [65].

The reconstructed jet momentum was compared to the initial quark (or gluon) momentum before Final State Radiation. From this comparison a calibration factor was calculated, giving two different calibration functions, one for

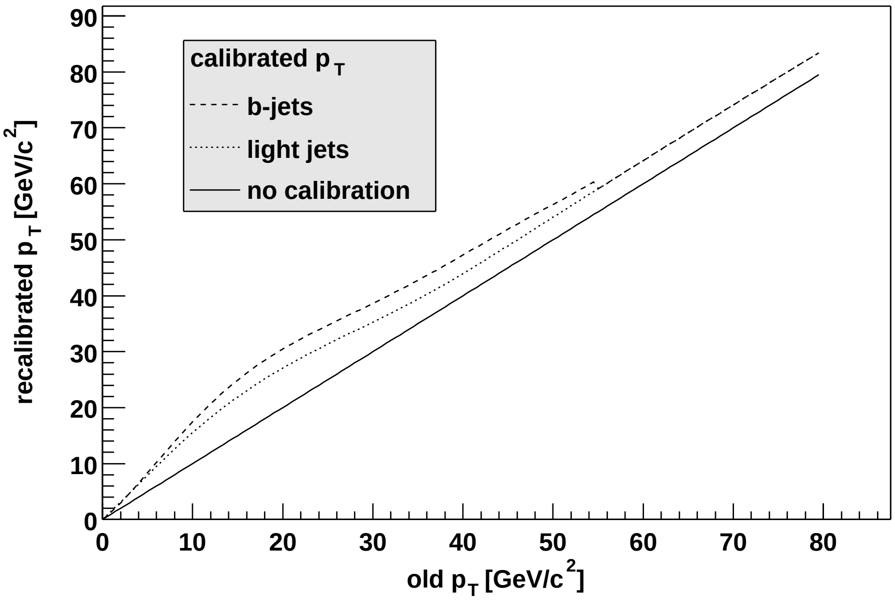

Figure 5.2: *Calibrated jet momentum calibration for b-jets and light jets*

heavy bottom flavoured jets and one for light jets.

$$\begin{aligned}
f_{b-jets}(p_T) &= 0.25436 \times 10^{-7} p_T^5 \\
&- 0.47454 \times 10^{-5} p_T^4 \\
&+ 0.33310 \times 10^{-3} p_T^3 \\
&- 0.10480 \times 10^{-1} p_T^2 \\
&+ 0.12241 p_T \\
&+ 1.2715, p_T < 55 GeV/c \\
f_{light\ jets}(p_T) &= 0.61538 \times 10^{-8} p_T^5 \\
&- 0.13921 \times 10^{-5} p_T^4 \\
&+ 0.11220 \times 10^{-3} p_T^3 \\
&- 0.36973 \times 10^{-2} p_T^2 \\
&+ 0.31468 \times 10^{-1} p_T \\
&+ 1.5085, p_T < 45 GeV/c
\end{aligned}$$

For higher transverse momenta the calibration factors approach unity, since the energy loss due to radiation processes becomes negligible if compared to the total jet momentum as can be seen in figures 5.1 and 5.2.

The calibration factor for b-jets is higher than for light jets, owing partially to the fact that b-jets can include non-observable neutrinos. For low transverse

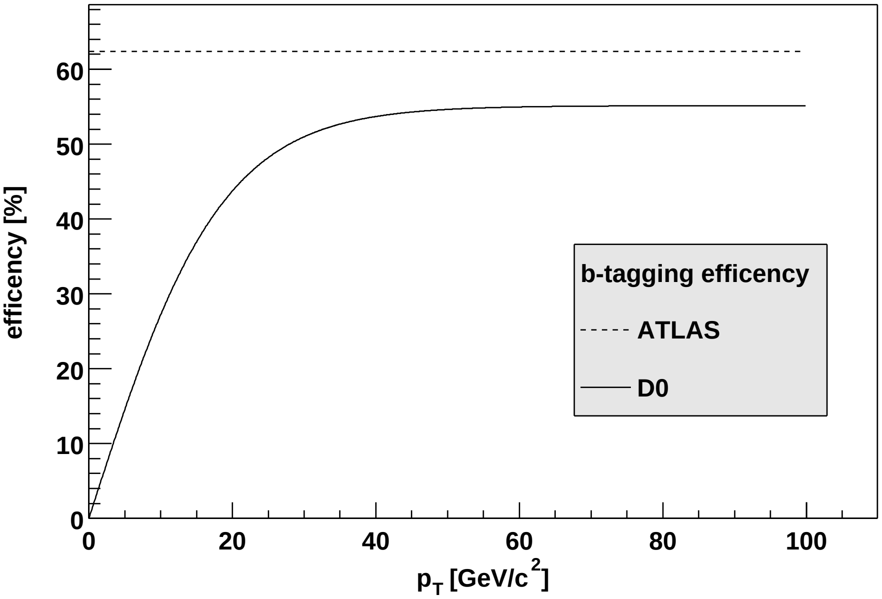

Figure 5.3: *Parameterized b-tagging efficiency for DØ and ATLAS*

momenta (below 20 Gev/c) lighter jets are more collimated than b-jets and the cone algorithm does not add all the particle tracks belonging to the b-jet to the reconstructed jet. This reduces the jet energy which is given by the energy sum of all particles included in the jet.

For higher transverse momenta the difference in the factors decreases since the b-jets get a higher boost in the jet direction and become more collimated.

One can use these calibration functions for both the PGS and ATLFast version since the jet reconstruction algorithms included in the different packages are very similar. The mass peak is correctly located at the Higgs mass with an error less than 2 %[2] for both simulations.

It has to be pointed out that the jet momentum calibration does not give the correct jet energy scale, which is taken into account in the subsequent analysis. The constraints set for jets already include the calibration factors and must be changed if non-calibrated jet information is used.

5.1.5 Parameterized jet flavour tagging

The flavour tagging schemes for the DØ detector as well as the ATLAS detector are not completed at the date of this study. In the case of the DØ detector there exist several proposals for tagging schemes, ranging from simple impact parameter tagging to full three-dimensional secondary vertex reconstruction.

---

[2] see section **??** on page ?? for details.

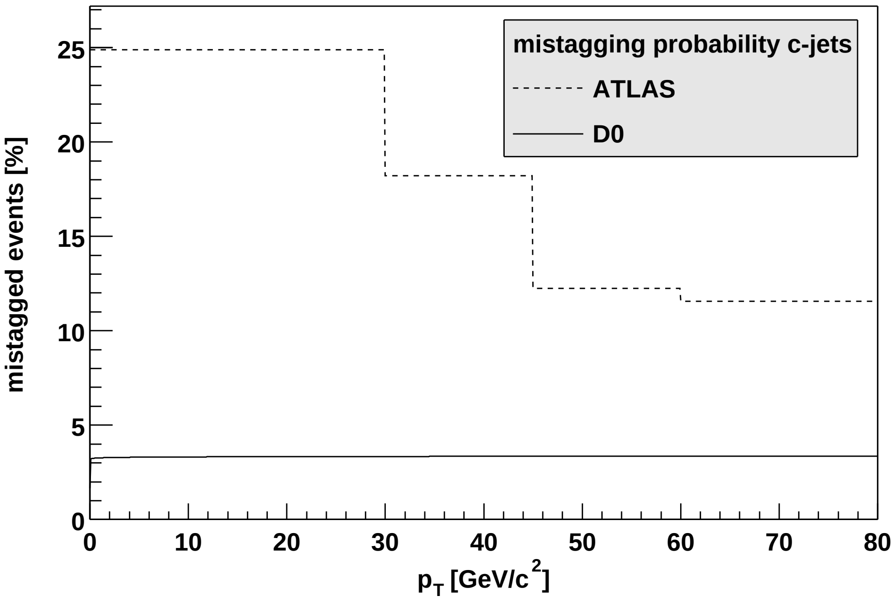

Figure 5.4: *Parameterized mistagging probability for charm flavoured jets*

In this study the flavour tagging algorithms are replaced by a parameterized function depend only on the jet transverse momentum and the initial jet flavour tag. For the PGS simulation the flavour tagging scheme was not changed for reasons of comparability.

Three different flavour tagging parameterizations have to be distinguished, the efficiency for correctly identifying a bottom flavoured jet, the mistagging probability for wrongly identifying a charm flavoured jet as bottom flavoured and the mistagging probability for light jets, including hadronically decaying tau leptons.

For the ATLAS detector the b-tagging efficiency was chosen to be constant for the whole momentum range at 62.4 % [63]. At low values of $\mathrm{p_T}$ the mistagging probability for charm flavoured and light jets is increased to keep the b-tagging efficiency constant.

The DØ b-tagging efficiency strongly increases with increasing transverse momentum [68]

$$f(p_T)^{eff}_{b-tag} = 0.5514 \cdot \tanh(\frac{p_T}{18.15})$$

while the mistagging probabilities are almost constant over a large momentum range

$$f(p_T)^{mistag}_{charm} = 1.657 + 1.61 p_T^{0.01322}$$
$$f(p_T)^{mistag}_{light\,jets} = 0.01$$

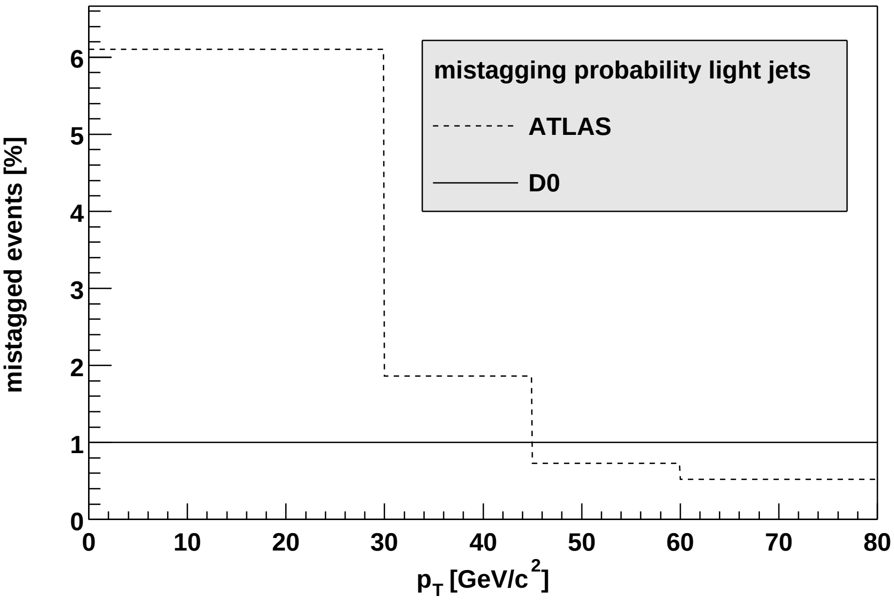

Figure 5.5: *Parameterized mistagging probability for light jets, including hadronically decaying tau leptons*

This parameterization is different to the case of ATLAS in which a growth in the number of mistagged events is accepted to keep the b-tagging efficiency constant [65]

$$f(p_T)^{mistag}_{charm} = \begin{cases} 0.25 & , p_T < 30GeV/c \\ \quad\vdots & \\ 0.12 & , p_T > 60GeV/c \end{cases}$$

$$f(p_T)^{mistag}_{light\,jets} = \begin{cases} 0.06 & , p_T < 30GeV/c \\ \quad\vdots & \\ 0.005 & , p_T > 60GeV/c \end{cases}$$

Both tagging schemes give better results for tagging efficiency as well as mistagging probability at higher values of $\mathrm{P_T}$ (see figures 5.3, 5.4 and 5.5). In this range the jets are more collimated and the secondary vertex resolution is increased.

The tagging algorithm included in the PGS simulation is different from the parameterized tagging schemes listed above. It is based on the CDF flavour tagging efficiencies measured in the TEVATRON Run I. It uses impact parameter as well as Monte Carlo flavour information to assign flavour tags to jets.

The parameterization used for the ATLFAST simulation was computed using the full DØ detector simulation, taking into account the upgraded DØ inner detector system. For the studies in [25, 62, 63] – in which the tagging efficiency was set to 60% and the mistagging probability for charm flavoured jets to 10% – these parameterizations were not available and a difference in b-tagging efficiency from 5 % upto 20 % and more can be found if compared to previous studies.

This greatly reduces the number of events in which two bottom flavoured jets are successfully reconstructed and thus decrease the number of signal events surviving the analysis cuts.

5.1.6 Influence of the cone radius on the reconstructed Higgs boson mass

The cone radius R_{cone} defines a circle around the cluster initiator cell in the calorimeter which encompasses all the calorimeter cells belonging to the cluster. If a calorimeter cluster is associated to a jet the jet energy and direction is given by the deposited cluster energy and the direction of the cluster.

For small cone radii some particle tracks are wrongly excluded from the jet and the estimated jet energy is too small. The number of reconstructed jets is higher than for larger radii. With growing cone radius the number of jets decreases and the jet energy increases.

At cone radii values near 1.0 particle tracks not belonging to the jet are added, increasing the reconstructed mass above the value set in the Monte Carlo generator.

In figure 5.6 on the following page the deviation of the invariant mass – obtained by a simple Gaussian fit to the mass spectrum – from the true Higgs mass m_{true} as entered in the Monte Carlo generation is plotted. On the left the values obtained with the ATLFAST simulation are listed and are opposed to the PGS results on the right.

The best agreement is found for a cone radius of 0.7 in case of the ATLFAST simulation and 0.4 in case of the PGS simulation. For these values the deviation given by

$$d(m_{true}, m_{fit}) = \frac{m_{fit} - m_{true}}{m_{true}}$$

is less than 2% for a Higgs boson mass greater 115 GeV/c^2. The difference found in the number of b-jet pairs for the ATLFAST and PGS simulation originate in the different b-tagging schemes. The PGS tagging algorithm calculates the impact parameter. If a b-jet is split into several jets these jets can have a large impact parameter as well and can therefore be identified as b-jets.

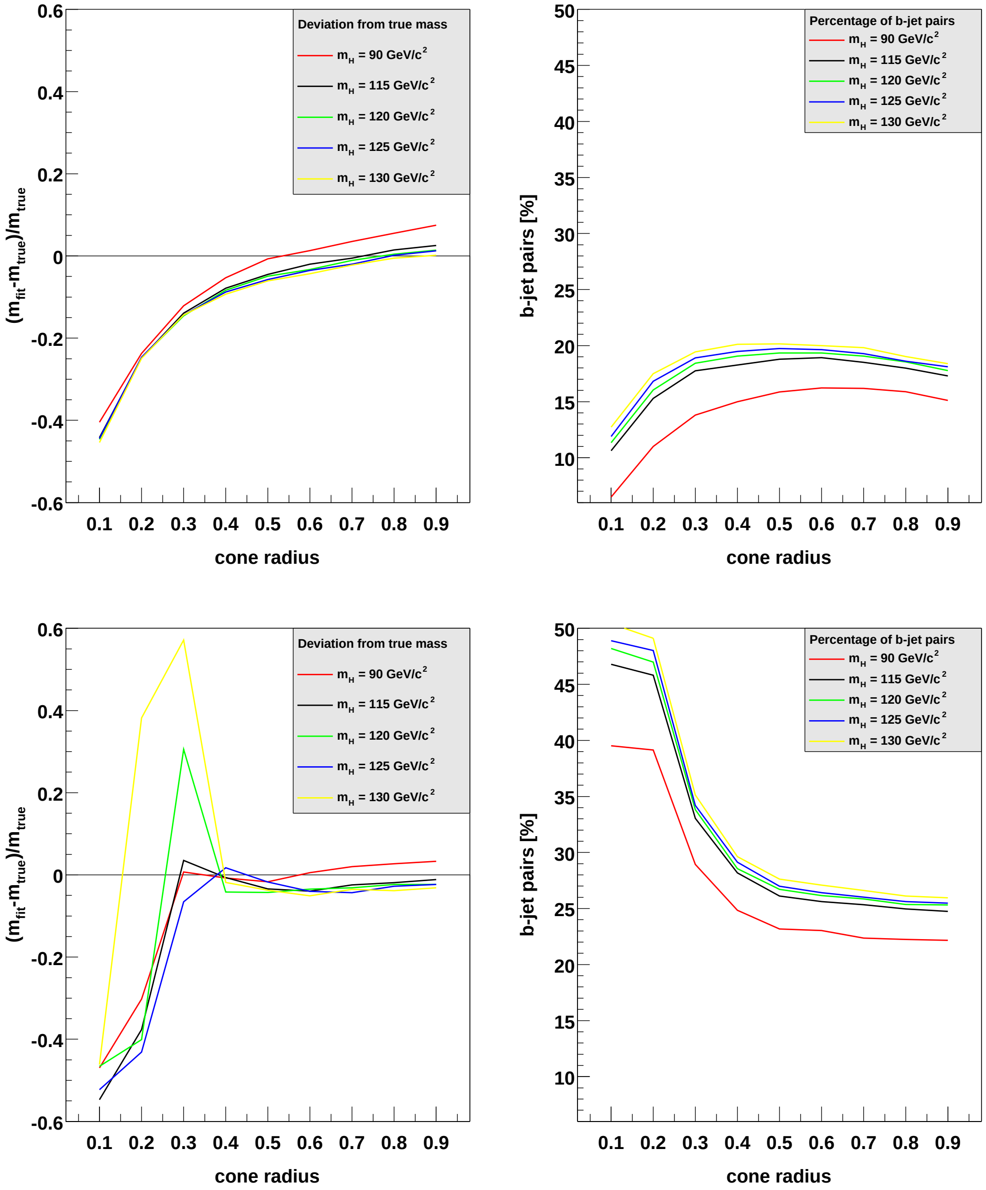

Figure 5.6: *Reconstructed invariant mass and number of b-jet pairs for DØ (top: ATLFast, bottom: PGS)*

Thus the number of b-jets increases for smaller cone radii in case of the PGS simulation. In the case of the ATLFast simulation the b-tagging efficiency depends on the transverse momentum of the jet, which decreases if a jet is split to several jets. A second effect which has to be taken into account is the increase in the number of jets. The fraction of two-jet events decreases while the number of events with three or more jets increases.

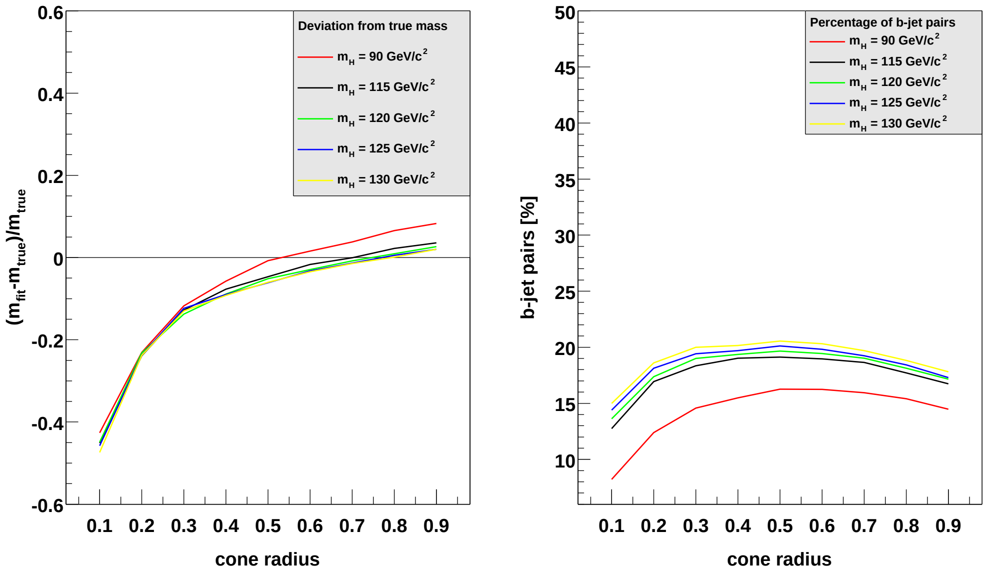

Figure 5.7: *Reconstructed invariant mass and number of b-jet pairs for ATLAS*

Together these two effects slightly decrease the number of b-jet pairs reconstructed by the ATLFast simulation for small cone radii, which can also be seen in figure 5.7 corresponding to the ATLAS detector data.

Comparing the number of reconstructed b-jets obtained with the two detector simulations the values corresponding to the PGS simulation are about 7 % higher than those obtained with the ATLFast simulation.

The plots presented here were produced selecting the signal process $W^{\pm}H$ and setting the Higgs mass to the values used in the analysis. The signal process Z^0H showed similar results.

Except for a Higgs mass of 90 GeV/c^2 the deviation of the fitted value from the true value are small, but only the higher Higgs mass values are not included by the LEP values [1] – hence the detector simulations reconstruct the Higgs mass correctly in the range of interest.

5.1.7 The influence of initial and final state radiation on the di-jet mass resolution

A good di-jet mass resolution of the detector is needed to separate the resonant background processes from the signal. For a Higgs boson mass of 115 GeV/c^2 the distance of the mass peaks produced by the Higgs boson and the Z^0 boson is 25 GeV/c^2.

The ATLFast simulation gives values of 12 % up to 15 % for the di-jet mass resolution that are in agreement with full simulation studies of the ATLAS detector [43].For the DØ detector the Tevatron Higgs Working [25] obtained results for the di-jet mass resolution similar to those found in this study with

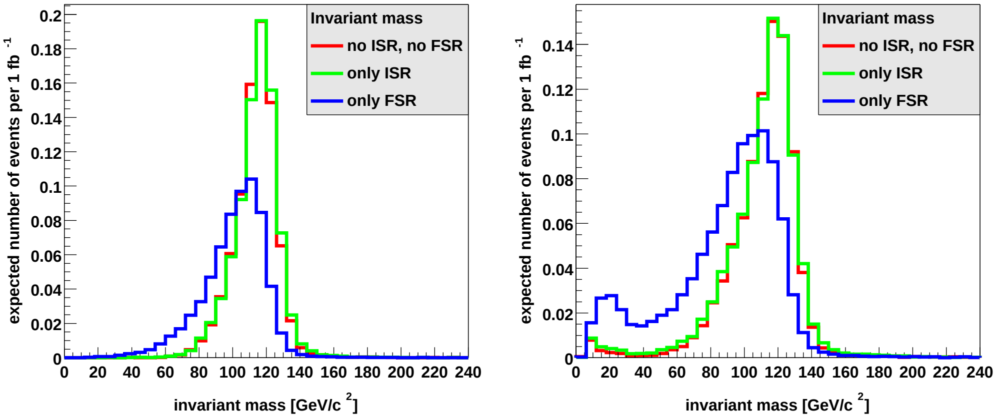

Figure 5.8: *Reconstructed invariant mass of b-jet pairs for DØ (left: ATLFast, right: PGS)*

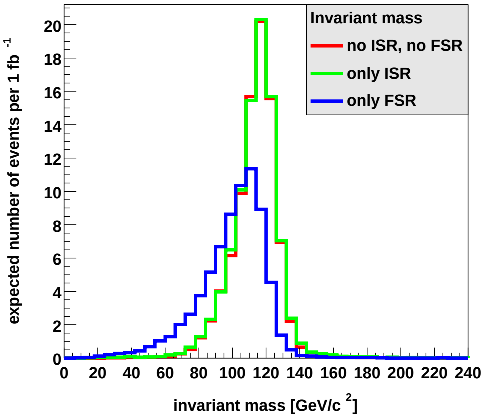

Figure 5.9: *Reconstructed invariant mass of b-jet pairs for ATLAS*

the ATLFast and PGS simulation, but which were scaled to 10 GeV/c^2, which is believed to be achievable with the upgraded detector. For the case of DØ the values for the mass resolution used in this study obtained with the ATLFast version were found to agree with a value of 15 %.

The mass spectrum reconstructed for the two bottom flavoured jets originating in the decay of a Higgs boson with a mass of 115 GeV/c^2 was analysed to determine the influence of initial and final state radiation on the mass resolution.

As was pointed out in section 2.1.2 on page 41 initial state radiation can cause a surplus of values greater than the Higgs mass in the reconstructed mass spectrum. This effect was found to be small in comparison to the distortion of the spectrum caused by final state radiation effects.

A shift to lower mass values is observed – see figures 5.8 and 5.9 – if final state radiation is permitted. This shift is explained in section 2.1.2 on page 41.

The mass peak is broadened and the mass resolution deteriorated. With the upgraded DØ inner detector system the resolution should be enhanced because the origin of tracks can be reconstructed with a better resolution, increasing the number of tracks correctly assigned to a jet.

In this study the mass resolution computed by the detector simulations was used in the analysis. This is a conservative estimate of the detector performance which has proven to be correct in Run I of the Tevatron. It can be scaled to smaller values if the prospected resolution for the DØ detector has been achieved, since it is mostly relevant for cuts restricting the reconstructed mass to a certain range of values only these cut efficiencies have to be recalculated.

Figures 5.8 on the facing page and 5.9 show the different mass distribution. The invariant mass of the two b-jets with highest transverse momentum is plotted. The influence of final state radiation on the invariant mass spectrum is clearly visible in all three plots – it is broadened and the peak of the distribution is slightly shifted to lower mass values.

Comparing the distributions obtained with the PGS and the ATLFAST simulation one observes a difference in the mass spectrum for low masses. The increase in the mass distribution at 20 GeV/c^2 found for the PGS simulation is caused by mistagged tau jets.

For lower transverse momenta the mistagging probability of the PGS impact parameter algorithm increases and the hadronically decaying taus coming from the decay of the Z^0 boson are assigned to the wrong flavour. This deviation is not found in case of the ATLFAST simulation.

5.2 Analysis of the final state $l^+l^-b\bar{b}$

The final state $l^+l^-b\bar{b}$ represents the signal and background final states to the signal process Z^0H. Relevant to the analysis are those events containing two opposite sign, same flavour leptons and two tagged bottom flavoured jets.

With these constraints only the background processes Z^0Z^0, $Z^0b\bar{b}$ and $t\bar{t}$ are relevant. For reasons of completeness the QCD background process $b\bar{b}$ has been added, although it is reduced to negligible values by the later analysis.

5.2.1 Characterization and selection of events with the final state $l^+l^-b\bar{b}$

Number distribution of bottom flavour-tagged jets

The number of bottom flavour-tagged jets – see figures 5.10 and 5.11 – gives an indication of the fraction of events which enter the analysis. Since a number of exactly two jets with a bottom flavour tag is required for the analysis those events with a higher or lower number are discarded.

Mistagging increases the number of b-jets while a lower b-tagging efficiency decreases the number of b-jets found per event. Since the mistagging probability is low the dominant effect is a shift of the number distribution to lower values.

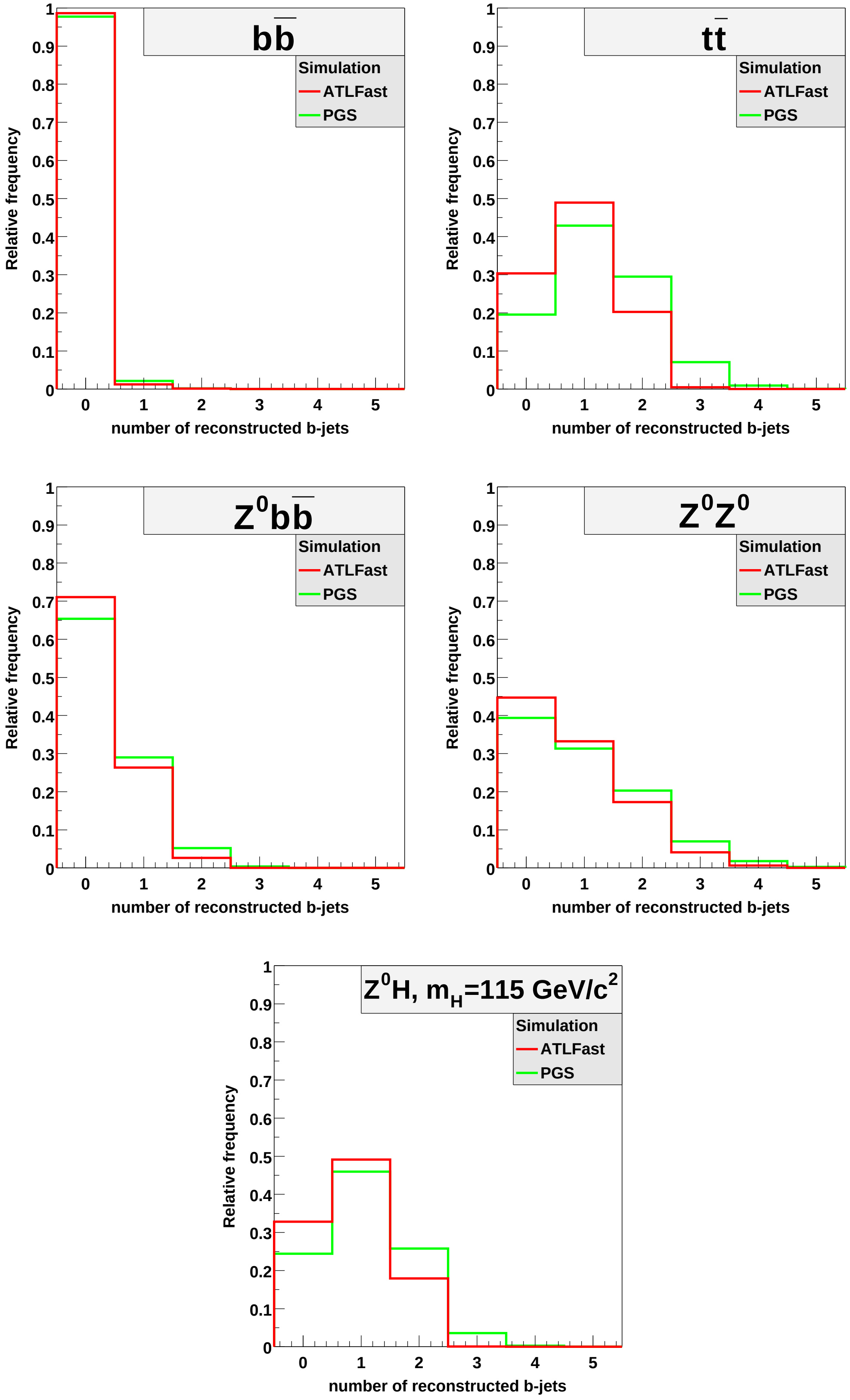

Figure 5.10: *Number of b-tagged jets for DØ, final state* $l^+l^-b\bar{b}$

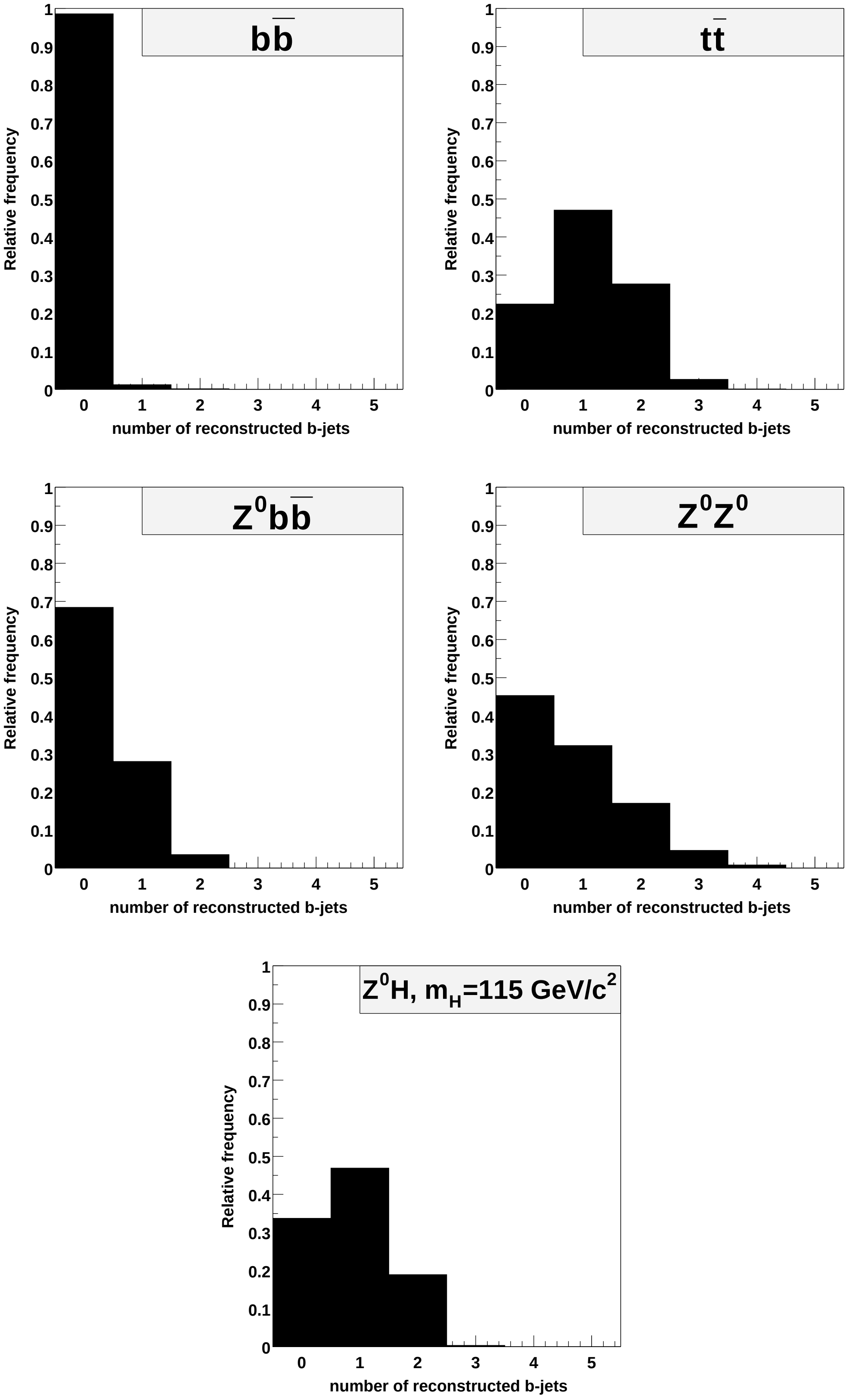

Figure 5.11: *Number of b-tagged jets for ATLAS, final state* $l^+l^-b\bar{b}$

This is obvious for the signal events, which – without mistagging – are expected to have two bottom flavoured jets per event. Instead in many events one b-jet is not reconstructed correctly and a the number of events including only one b-jet is higher than the number of those events with two jets.

The b-tagging efficiency decreases with decreasing transverse momentum. Except for the QCD $b\bar{b}$ and the $Z^0 b\bar{b}$ background all background processes and the signal process mainly include b-jets with high transverse momentum, since the b-jets originate in the decay of heavy particles.

A dependency of the b-jet number on the mass of the particle decaying into two bottom quarks can also be found for the signal process distributions comparing different Higgs boson masses.

For a Higgs mass of 130 GeV/c^2 the number of events including two b-jets is slightly higher than for a mass of 90 GeV/c^2, while the number of events with only one bottom flavoured jet in the final state is lower for a lower mass. Nevertheless this difference is small and therefore only the number distribution for a Higgs mass of 115 GeV/c^2 is shown as an example.

The decrease in the b-tagging efficiency greatly decreases the number of $b\bar{b}$ events with two b-tagged jets. Additionally the restriction to a certain region of pseudorapidity in which b-tagging can be applied reduces the number of b-jet pairs found in the $b\bar{b}$ events.

This partly applies to the $Z^0 b\bar{b}$ process as well, in which the bottom quark pair is created in the decay of a gluon. Here only small deviations in the distributions are found for the three decay channels $Z^0 \rightarrow e\bar{e}$, $Z^0 \rightarrow \mu\bar{\mu}$ and $Z^0 \rightarrow \tau\bar{\tau}$. For the latter the mistagging of tau-jets increases the number of b-jets found compared to the former two.

The relative frequency of b-jet pairs can be taken as an estimate of the average b-tagging efficiency. The square root of the relative frequency of correctly identified b-jet pairs approximately gives the efficiency for the correct identification of one b-jet.

This approximation is valid only for b-jets with high transverse momentum since in this regime the rise in the slope of the b-tagging efficiency function is small and the efficiency can be expressed by a single value. In the case of the ATLAS tagging parameterization this approximation is valid for all transverse momenta because in this scheme the tagging efficiency is held constant.

A comment should be made on the number distribution referring to the processes $Z^0 Z^0$ and $t\bar{t}$. In both cases events with more than two bottom quarks in the intermediate state are included, for example if both Z^0 bosons decay to a pair of bottom quarks. The tagging efficiency reduces the number of events with four bottom flavoured jets in the final state, raising the number of those events including three and less b-tagged jets.

Comparing the results obtained with the PGS simulation to those of the ATLFAST simulation one finds that the PGS flavour tagging algorithm assumes a better b-tagging efficiency than the parameterized efficiency used with the

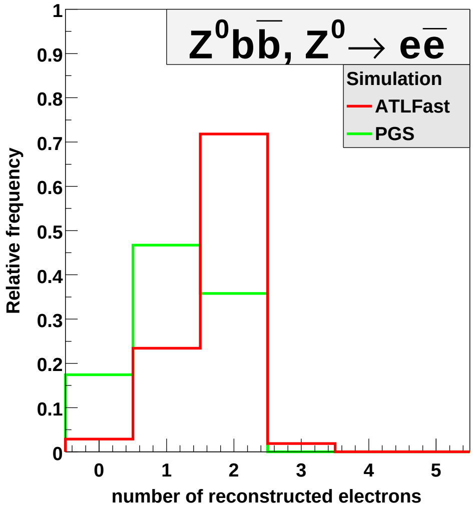

Figure 5.12: *Difference between the PGS and the ATLFast simulation in the reconstruction efficiency for electrons.*

ATLFast simulation[3], resulting in higher values for the number of reconstructed b-jets.

Number distribution of reconstructed charged light leptons

Only those events with two b-jets and two leptons in the final state are considered in the analysis. The lepton number per event was found to be almost independent of the chosen Higgs mass since the leptons originate from the decay of the associated Z^0 boson. Therefore only the signal process with the Higgs mass set to 115 GeV/c^2 is plotted.

The number distributions of isolated, charged light leptons – electrons and muons – are plotted in figure 5.15. Hadronically decaying tau leptons only enter the analysis if they are misidentified as b-jets.

Leptonically decaying tau leptons, more precisely their decay products muons and electrons, enter subsequent analysis steps, because only light charged leptons serve as a trigger constraint for the associated production of a Higgs boson with a gauge boson.

The number distributions presented here are independent of the lepton flavour. Even if a number of two leptons is given in an event, this does not imply that two leptons of the same flavour are found in the event, an event might contain an electron and an anti-muon in the final state.

Despite this insensitivity to the lepton flavour a final state with mixed lepton flavours can only be created by the $t\bar{t}$ process[4]. Hence the relative frequency for

---

[3] see also figure 5.6 in section 5.1.6 on page 93

[4] The $b\bar{b}$ process is not taken into account.

a number of two leptons has to be halved in the $t\bar{t}$ plot if only OSSF[5] leptons are considered.

All Monte Carlos samples except those for the process $Z^0b\bar{b}$ are inclusive samples, meaning they contain charged leptons of all three flavours. Each lepton flavour refers to a certain identification efficiency. Here only the numbers for the mixed sample including all three flavours are presented [6].

In the case of the Z^0Z^0 and $t\bar{t}$ samples the inclusion of purely hadronic and semi-leptonic final states causes the distribution to peak at low values for both b-jets and leptons, which would not be expected for a pure sample containing only those events with a final state $l^+l^-b\bar{b}$.

As was expected the smallest fraction of two final state leptons is reconstructed for the QCD background. It contains only a small fraction of events including one isolated lepton or more.

It was found that the PGS and ATLFast simulation differ significantly in the reconstruction efficiency for electrons, the ATLFast simulation showing a much better reconstruction performance (see figure 5.12 on the preceding page). A similar effect was also found for muons, but it is less pronounced.

The effect is also visible in the transverse momentum distributions for the leptons (see for example figure 5.14). From these distributions one can deduce that the number of leptons reconstructed from the $t\bar{t}$ process are much higher in the case of the PGS simulation and lower for the $Z^0b\bar{b}$ process.

Interestingly these differences only occur at low values of momentum, which suggest that the surplus in leptons for the $t\bar{t}$ process originates in a isolation criterion falsely identifying non-isolated low momentum leptons as isolated.

A possible explanation is the parameterization of the electron identification efficiency implemented in the ATLFast simulation which was designed to fit to the ATLAS environment.

Since the electron reconstruction efficiency is about 90 % for both ATLAS and DØ the values obtained with the ATLFast simulation give a better, if not too good, approximation to the number distribution expected for the DØ detector.

The more obvious difference can be found in the isolation criteria for electrons integrated in the detector simulations (see [25] for details on the PGS isolation criteria).

---

[5] **o**pposite **s**ign, **s**ame **f**lavour

[6] It should be pointed out that the sample $Z^0 \to \tau\bar{\tau}$ contains hadronically decaying tau leptons as well as those decaying leptonically

The ATLFast criterion is based on the selection of an isolation radius, while the PGS simulation criteria also include the distribution of the shower energy in the calorimeters.

Last, the minimum energy for an isolated electron is set to 10 GeV in the standard PGS simulation while this is reduced to 5 GeV in the ATLFast simulation, corresponding to the value stated for the upgraded DØ detector. Despite these differences the effect becomes less important if the samples are mixed and one does not distinguish between different lepton flavours.

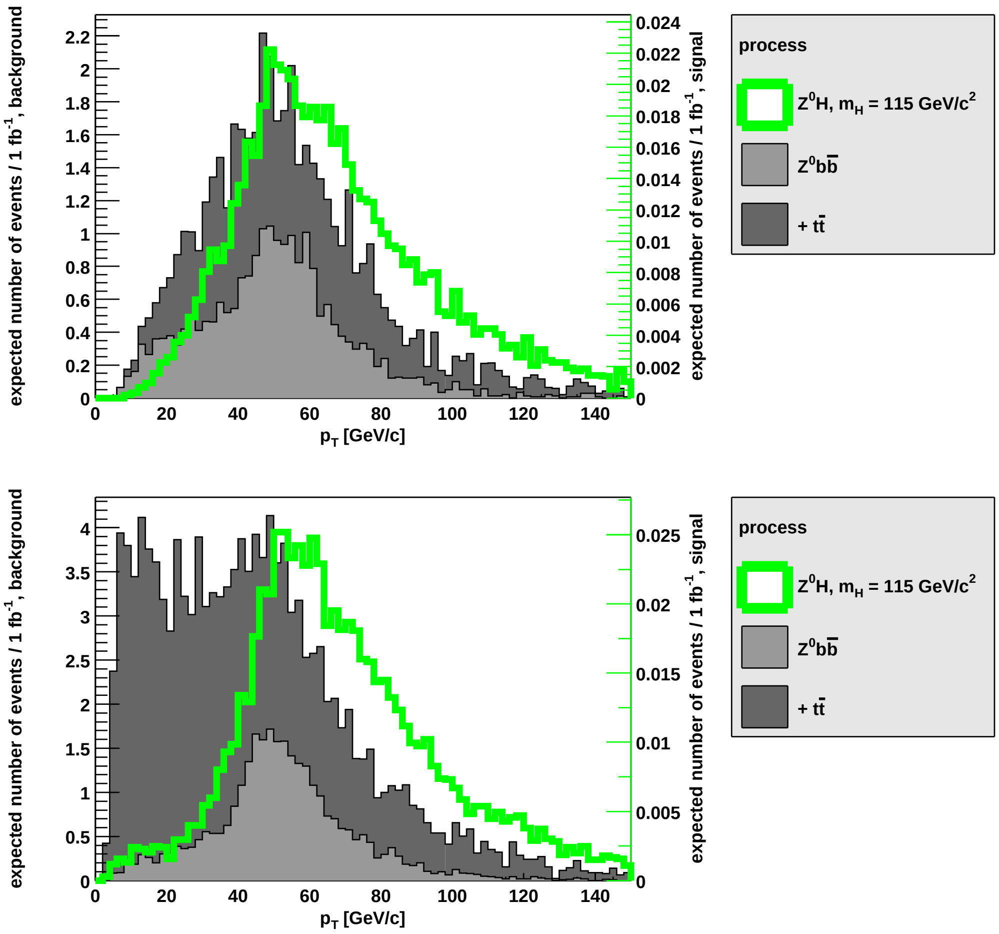

Figure 5.13: *Differences in the p_T distribution for the light lepton with the highest transverse momentum in the final state $l^+l^-b\bar{b}$ between the ATLFast (top) and the PGS (bottom) simulation of the DØ detector*

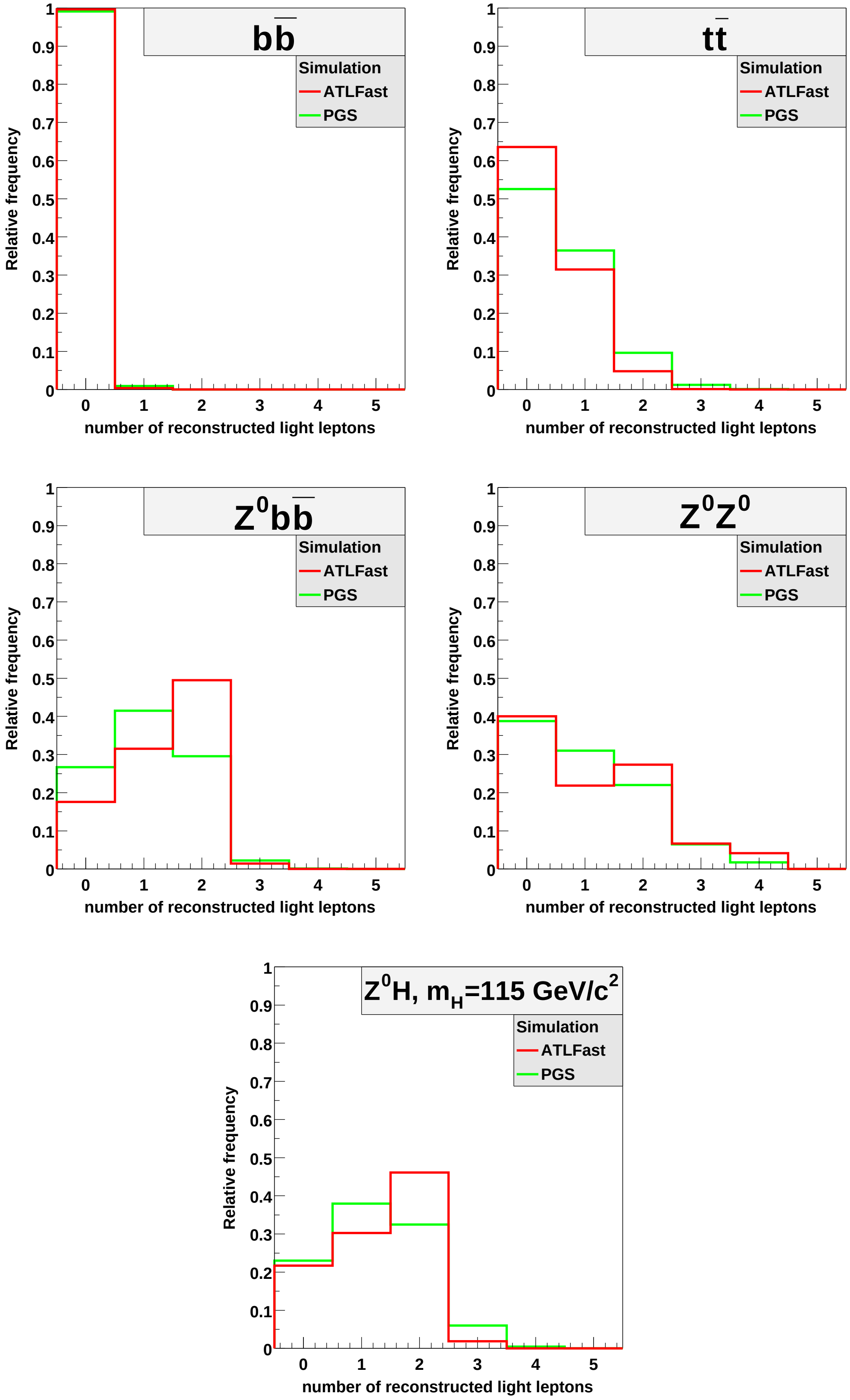

Figure 5.14: *Number of leptons for DØ, final state* $l^+l^-b\bar{b}$

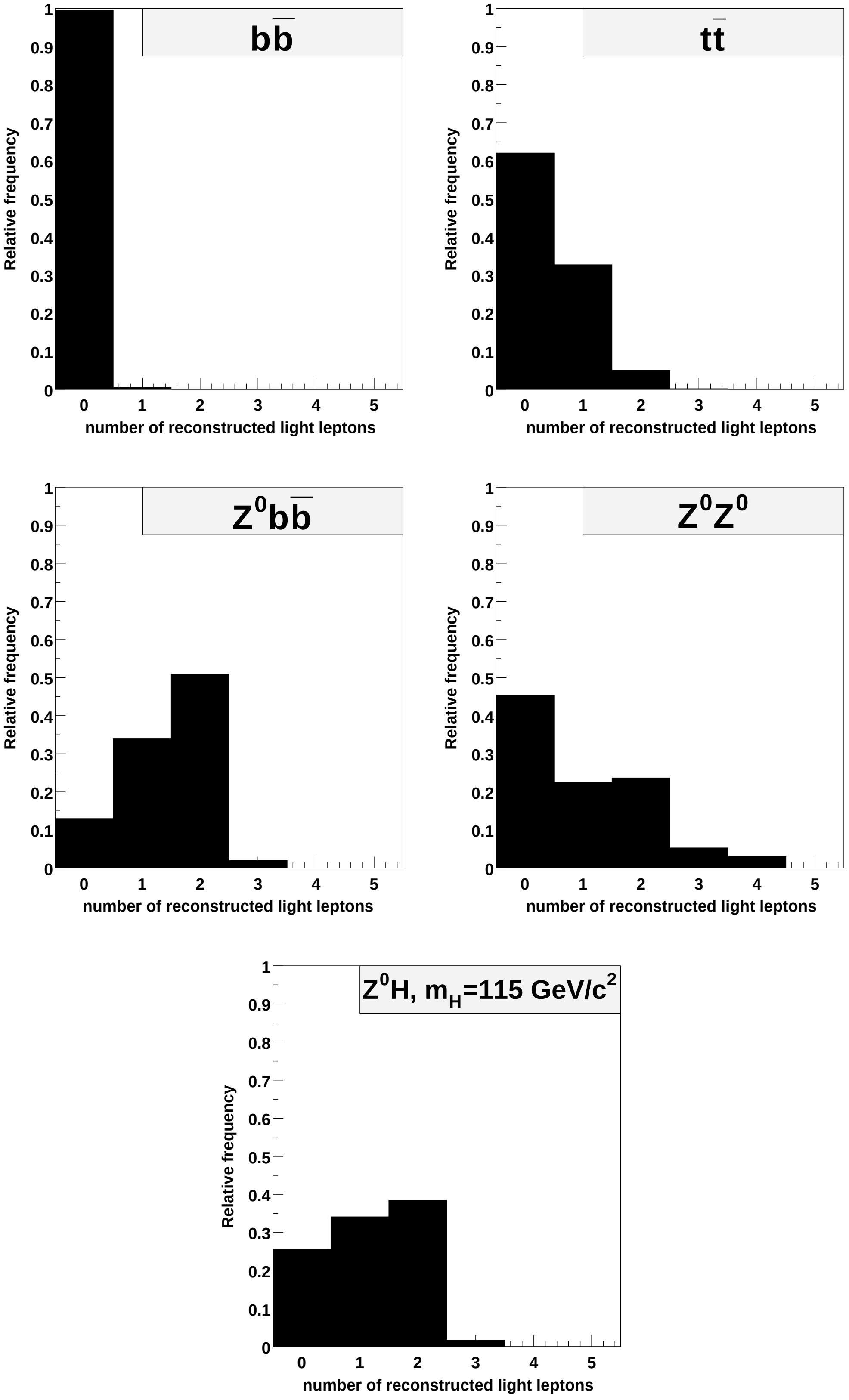

Figure 5.15: *Number of leptons for ATLAS, final state* $l^+l^-b\bar{b}$

Accepted cross sections for the final state $l^+l^-b\bar{b}$

The acceptance criteria for the final state labelled $l^+l^-b\bar{b}$ were chosen as follows: An event has to include

- Two bottom flavour-tagged jets
- Two OSSF light charged leptons

The second constraint assumes that the two leptons with the highest transverse momentum originate in the decay of the Z^0 boson in all signal events, hence the test on sign and flavour is applied to these leptons.

With this pre-selection one obtains the fractions of accepted events found in table 5.1. For the $Z^0b\bar{b}$ process the combined cross section for all lepton flavours is cited.

Table 5.1: **Accepted cross sections for the final state $l^+l^-b\bar{b}$**

Process	surviving events [%]		accepted cross section [fb]	
	DØ	ATLAS	DØ	ATLAS
Z^0H, $m_H = 90$ GeV/c^2	10.2 (9.9)	6.8	1.7 (1.6)	10.1
Z^0H, $m_H = 115$ GeV/c^2	11.5 (11.0)	8.6	0.79 (0.76)	5.7
Z^0H, $m_H = 120$ GeV/c^2	11.6 (11.2)	8.7	0.65 (0.63)	4.9
Z^0H, $m_H = 125$ GeV/c^2	11.8 (11.1)	8.9	0.53 (0.50)	3.9
Z^0H, $m_H = 130$ GeV/c^2	11.9 (11.4)	9.2	0.40 (0.39)	3.1
$b\bar{b}$	≈ 0 (5.7×10^{-4})	≈ 0	≈ 0 (2.6×10^{-5})	≈ 0
$t\bar{t}$	0.55 (1.5)	0.57	36 (99)	3800
$Z^0b\bar{b}$	1.8 (2.7)	2.1	32 (48)	1700
Z^0Z^0	4.3 (4.3)	3.0	3.7 (3.7)	25

Accepted fraction of events and cross sections for the final state $l^+l^-b\bar{b}$. The values in brackets relate to the PGS simulation.

Comparing the accepted fraction of events for the ATLAS and DØ detector one finds they agree with another, although a tendency towards lower acceptance values for signal events can be observed for the ATLAS detector.

The main difference concerns the acceptances for the $t\bar{t}$ background if the results for the PGS and ATLFAST simulation are considered. In this case a discrepancy of a factor three is found. Light charged leptons produced by the $t\bar{t}$

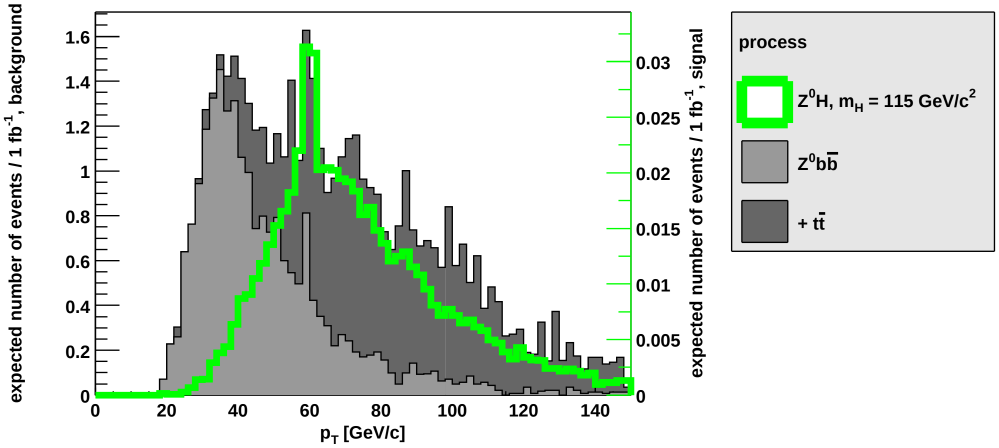

Figure 5.16: *p_T distribution for the b-jet with the highest transverse momentum, final state $l^+l^-b\bar{b}$, obtained with the* ATLFast *simulation of the* DØ *detector for a Higgs mass of 115 GeV/c^2*

process are reconstructed with a higher efficiency by the PGS simulation than by the ATLFast simulation, reversing the effect found for the $Z^0b\bar{b}$ process (see also figure 5.25 on page 118). This clearly alters the results of subsequent analysis criteria imposed on events coming from the $t\bar{t}$ process.

Differences also occur for other background channels, see section 5.2.1 on the preceding page for details.

5.2.2 Selection of kinematic variables

The kinematic variables of interest for the analysis were introduced in [25, 62, 63]. These variables are

- **Transverse momentum**, p_T, of b-jets and charged light leptons
- **Pseudorapidity**, η, of b-jets and charged light leptons
- **Invariant mass** of the b-jet and charged light lepton pair

The first two variables, if combined with the azimuthal angle ϕ, are needed to reconstruct the full momentum four vector for both bottom flavour tagged jets and charged light leptons. The variations in the distributions of the azimuthal angle do not suffice to distinguish background from signal events and therefore only the listed kinematic variables enter the subsequent analysis.

If no radiation processes, detector inefficiencies and reconstruction algorithms – namely jet finding and flavour tagging algorithms – are regarded this set of variables would be sufficient to compute the full kinematics of the final state. Thus a good knowledge of the influence of these effects is vital for the understanding of the event characteristics.

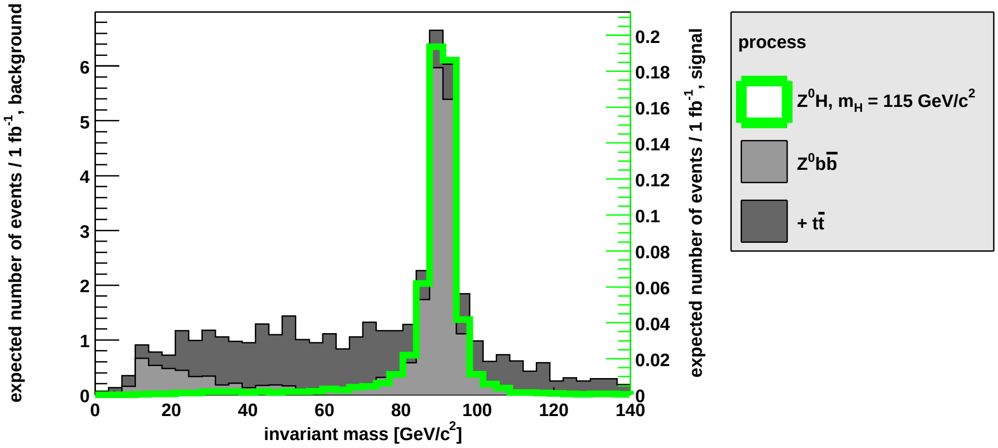

Figure 5.17: *Invariant mass of the two OSSF leptons in the final state $l^+l^-b\bar{b}$, obtained with the ATLFast simulation of the DØ detector for a Higgs mass of 115 GeV/c^2*

For the bottom flavour-tagged jets found in an event the distribution of the transverse momentum and the pseudorapidity was studied looking at

- the b-jet with the highest transverse momentum
- the b-jet with the second highest transverse momentum

This analysis was repeated for the charged light leptons, again selecting

- the charged light lepton with the highest transverse momentum
- the charged light lepton with the second transverse momentum

For an example[7] see figure 5.16 on the preceding page. To give an idea of the form of the distribution for both signal and background the individual continuous backgrounds are stacked on each other, the scale is given by the axis on the left. The right axis gives the scale for the signal process – showing the relative size of background and signal contribution while the shape of signal and background distribution can be compared.

If the background processes enter the analysis additional variables become important to distinguish the latter from the former.

As an obvious choice the invariant mass reconstructed from the four-momentum vectors of the two OSSF leptons with the highest transverse momenta was considered. In the mass spectrum one would observe a peak at the value of the Z^0 mass if the leptons originate from the Z^0 boson associated to the Higgs particle (see figure 5.17). For two particles 1 and 2 and corresponding energies E_i and

---

[7] The peak found in all the distributions at a transverse momentum of about 60 GeV/c is caused by the calibration of the jet energy.

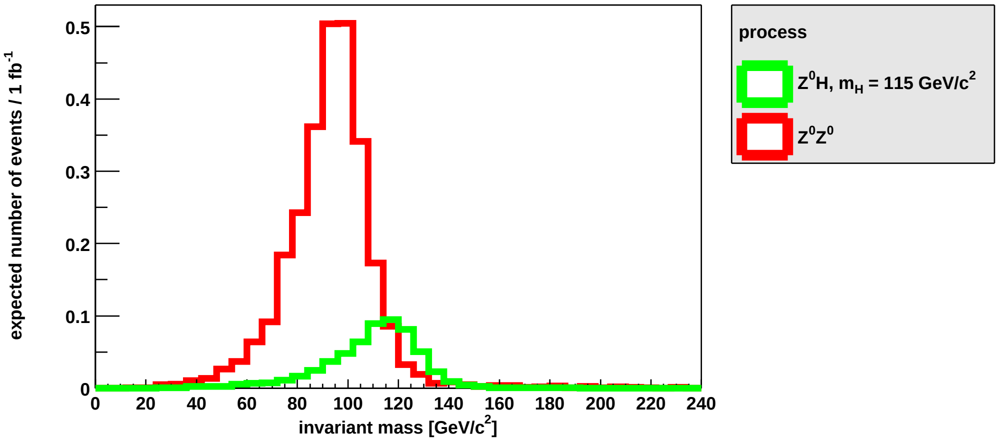

Figure 5.18: *Invariant mass of the b-jet pair for signal and resonant background in the final state $l^+l^-b\bar{b}$, obtained with the ATLFast simulation of the DØ detector for a Higgs mass of 115 GeV/c^2*

momentum vectors $\vec{p}_i$ in the laboratory frame the invariant mass is calculated as

$$m_{inv} = \sqrt{\frac{(E_2 - E_1)^2}{(\vec{p}_2 - \vec{p}_1)^2}}$$

Unfortunately this peak should also be observed for all of the background processes except the $\mathrm{b\bar{b}}$ and $\mathrm{t\bar{t}}$ background. The choice of the reconstructed invariant lepton-pair mass as a discriminating variable becomes important if $\mathrm{t\bar{t}}$[8] background events have to be differentiated from signal events, because the final state leptons in a $\mathrm{t\bar{t}}$ event arise from the decay of two $\mathrm{W}^{\pm}$ bosons.

One of the most promising selection variables is the reconstructed Higgs mass, computed as the invariant mass of the two b-tagged jets with the highest transverse momentum. For all background processes, except the resonant background $\mathrm{Z}^0\mathrm{Z}^0$, no mass peak should be found in the spectrum. Instead the non-resonant background mass distributions should be spread out over the kinematically allowed region of values; in this case one speaks of a continuous background.

For a known Higgs mass those events which do not yield a reconstructed mass value in a certain range near the Higgs mass peak can be discarded as background events. Since the Higgs mass is not known the selection of an appropriate range of values becomes difficult.

As the signal cross section is very small compared to the cross section of the background processes it is vital to reduce the background as far as possible. Furthermore the peak in the mass spectrum created by the resonant background

---

[8] If the $\mathrm{b\bar{b}}$ process is regarded the requirement of two OSSF leptons in the final state suffices to reduce the number of background events enormously.

process Z^0Z^0 must be clearly distinguishable from the signal peak (see figure 5.18). In this case one is able to reconstruct the mass peak with a simple gauss fit, obtaining both a value for the Higgs mass and an estimate of the width of the mass distribution.

In this study the Higgs mass is determined by the Monte Carlo generator setting. Thus the appropriate mass and range can be set beforehand. The results give an indication of the capabilities of further studies including mass peak reconstruction.

As a last variable the amount of hadronic energy deposited in the calorimeter was introduced in [25] as a variable and was replaced by constraints on jets with no bottom flavour-tag [62, 63]. This jet constraint includes information on radiative processes and event characteristics differing from the clean final state with two b-tagged jets and two charged light leptons.

Even in signal events additional jets can be found. These are either caused by the jet finder algorithm splitting a single jet into two or by high energetic particles coming from radiative remnants such as gluons produced in the final state radiation which are identified as jets. Thus the

- **Transverse momentum** of jets with no bottom flavour tag and the
- **Pseudorapidity** of jets with no bottom flavour tag

are added to the list of kinematic selection variables.

For this study an optimization of the variable selection criteria was not intended. It is believed that an improved simulation of the detector response is needed to fully exploit the differences in the kinematic variables selected to distinguish background from signal events.

The determination of the DØ detector performance has made good progress and the knowledge obtained since the beginning of the TEVATRON Run II will enter the simulation software. For the ATLAS detector simulation the ATLFAST simulation is being redesigned as an object oriented module in the new ATLAS software environment ATHENA.

The use of a fast detector simulation does not permit a sufficient reconstruction of kinematic variables to fully simulate the correct detector performance. Instead it gives a satisfactory simulation of the event characteristics which can be used to identify selection variables and study the effect of optimization techniques [69].

5.2.3 Selection of events

The criteria for the event selection are adopted from [25] for the analysis of the associated Higgs production at a center of mass energy of 1980 GeV – in the following text simply referred to as 2 TeV – and [63] for 14 TeV center of mass energy.

These so called cuts intend to reduce most of the continuous background by defining a fixed range for the kinematic variables introduced in section 5.2.2.

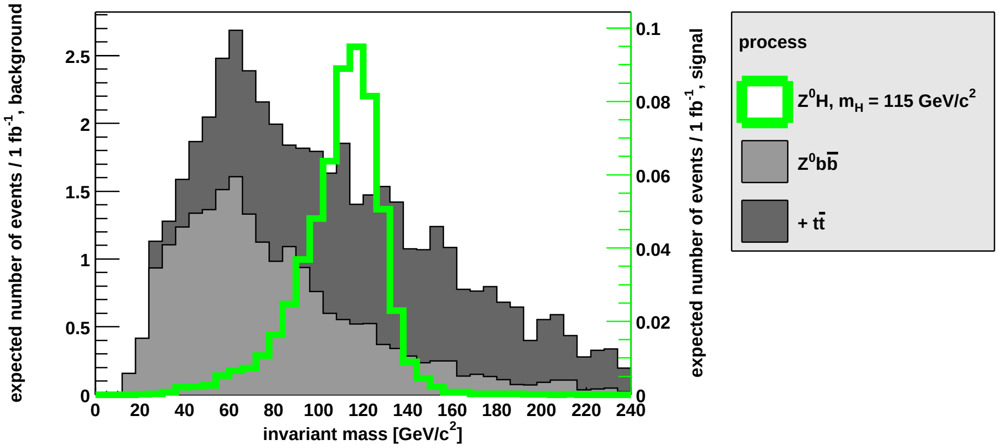

Figure 5.19: *Invariant mass of the b-jet pair for signal and continuous background in the final state $l^+l^-b\bar{b}$, obtained with the* ATLFast *simulation of the DØ detector for a Higgs mass of 115 GeV/c^2*

Although more efficient analysis techniques can improve the separation of background and signal events the results obtained with the kinematic constraints listed here serve as a good estimate of the DØ and ATLAS detection capacities with regard to associated Higgs production.

For reasons of brevity bottom flavour-tagged jets will be referred to as b-jets, the term lepton will label an isolated electron or muon. A jet without a bottom flavour tag will simply be called jet.

Furthermore the transverse momentum will be abbreviated $\mathrm{p_T}$ and the pseudorapidity range will be defined by the absolute value of η. The invariant mass of the leptons and the b-jets are labelled $\mathrm{m_{l^+l^-}}$ and $\mathrm{m_{b\bar{b}}}$ respectively – the Higgs and $\mathrm{Z^0}$ boson mass are given by $\mathrm{m_H}$ and $\mathrm{m_{Z^0}}$.

Selection criteria for a center of mass energy of 2 TeV

For a center of mass energy of 2 TeV the kinematic constraints were set as follows:

1. Two b-jets in $|\eta| < 2.0$
   - one with $\mathrm{p_T} > 20$ GeV/c
   - one with $\mathrm{p_T} > 15$ GeV/c
2. Two OSSF leptons with $\mathrm{p_T} > 10$ GeV/c in $|\eta| < 2.0$
3. $|\mathrm{m_{l^+l^-}} - \mathrm{m_{Z^0}}| < 10\ \mathrm{GeV/c^2}$
4. A maximum of one additional jet with $\mathrm{p_T} > 15$ GeV/c within $|\eta| < 2.5$

5. No additional jet with $p_T > 30$ GeV/c within $|\eta| < 2.5$

6. $|m_{b\bar{b}} - m_H| < 30\ \%\ m_H$

The constraints on the pseudorapidity basically describe the acceptance region for the reconstruction of b-jets and leptons. Pseudorapidity distributions do not show differences between signal and background events, neither for b-jets nor for leptons – regardless which center of mass energy is considered.

Events containing b-tagged jets with a low momentum are rejected by the first two constraints. These include jets falsely assigned with a bottom flavour tag, because the mistagging probability increases with decreasing transverse momentum, as well as b-jets created in the hadronization of a low-energy bottom quark.

It also improves the mass resolution of the invariant mass of the two b-jets, because b-jets with a higher momentum are more collimated and a jet cone algorithm is more likely to correctly assign tracks to jets.

The following step in the analysis chain sorts out events including leptons of the wrong flavour and charge and rejects events with only one lepton in the final state. The momentum constraint allows for the rejection of low momentum leptons produced in hadronization and radiation processes.

The constraint imposed on the invariant mass of the lepton pair discards most of the events in which the final state leptons are not produced in a Z^0 boson decay.

Additional jets with no bottom flavour tag and a high momentum should originate in the decay of a particle with a high mass like the top quark. This cut replaces the constraint on the hadronic energy cut according to [63].

The final cut on the invariant mass of the b-jets was added to estimate the maximum performance of an analysis which can identify the peak in the mass spectrum assigned to the Higgs boson correctly. The choice of 30 % m_H corresponds to a di-jet mass resolution of 15 % which was obtained with the DØ detector in Run I. It is believed that this value can be decreased to 10 %.

Selection criteria for a center of mass energy of 14 TeV

The kinematic cuts for a center of mass energy of 14 TeV are

1. Two OSSF leptons with $p_T > 15$ GeV/c in $|\eta| < 2.5$

2. $|m_{l^+l^-} - m_{Z^0}| < 6$ GeV/c^2

3. Two b-jets with $p_T > 15$ GeV/c in $|\eta| < 2.5$

4. No additional jet with $p_T > 30$ GeV/c within $|\eta| < 5.0$

5. $|m_{b\bar{b}} - m_H| < 20\ \%\ m_H$

These cuts resemble the cuts chosen for a center of mass energy of 2 TeV, only the mass constraints on the di-jet and di-lepton have been adopted to the ATLAS mass resolution for b-jets (see figures 5.19 and 5.20) and light charged leptons.

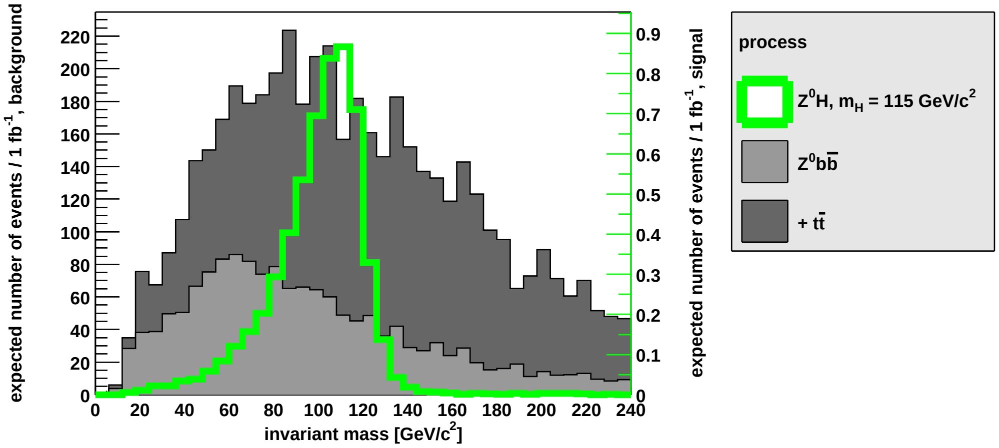

Figure 5.20: *Invariant mass of the b-jet pair for signal and continuous background in the final state $l^+l^-b\bar{b}$, obtained with the* ATLFast *simulation of the ATLAS detector for a Higgs mass of 115 GeV/c*^{2}

5.3 Analysis of the channel $\mathrm{l}^{\pm}\nu\mathrm{b}\bar{\mathrm{b}}$

The signal event $\mathrm{W}^{\pm}\mathrm{H}$ and the corresponding background events are subsumed under the final state $\mathrm{l}^{\pm}\nu\mathrm{b}\bar{\mathrm{b}}$, meaning that the state is characterized by a lepton, missing transverse energy and two b-tagged jets.

The dominant background processes with the desired final state were found to be $\mathrm{t}\bar{\mathrm{t}}$, $\mathrm{W}^{\pm *} \rightarrow \mathrm{tb}$, tqb, $\mathrm{W}^{\pm}\mathrm{b}\bar{\mathrm{b}}$ and $\mathrm{W}^{\pm}\mathrm{Z}^0$. Again the QCD background was added to the analysis but no events were found to survive the analysis chain.

The main difference two the $\mathrm{Z}^0\mathrm{H}$ final state is the missing transverse energy $\mathrm{E}_{\mathrm{T}}^{\mathrm{miss}}$ caused by an undetected neutrino with high energy (see figure 5.21 on the next page).

5.3.1 Characterization and selection of events with the final state $\mathrm{l}\nu\mathrm{b}\bar{\mathrm{b}}$

Number distribution of bottom flavour-tagged jets

In figures 5.22 and 5.23 the number distributions of b-tagged jets are presented. The distributions for the $\mathrm{b}\bar{\mathrm{b}}$ and $\mathrm{t}\bar{\mathrm{t}}$ process can be found in section 5.2.1 on page 97.

As was the case for the $\mathrm{Z}^0\mathrm{H}$ signal process the number distributions for the $\mathrm{W}^{\pm}\mathrm{H}$ process look similar, regardless of the Higgs mass. Since the reconstructed b-jets originate from the decay of the Higgs boson, the number distributions for both signal processes look almost alike, the differences are caused by the different final momentum of the Higgs boson.

The similarity in the distributions for the $\mathrm{Z}^0\mathrm{b}\bar{\mathrm{b}}$ and $\mathrm{W}^{\pm}\mathrm{b}\bar{\mathrm{b}}$ processes are also caused by the similarity of the underlying bottom quark production process. In

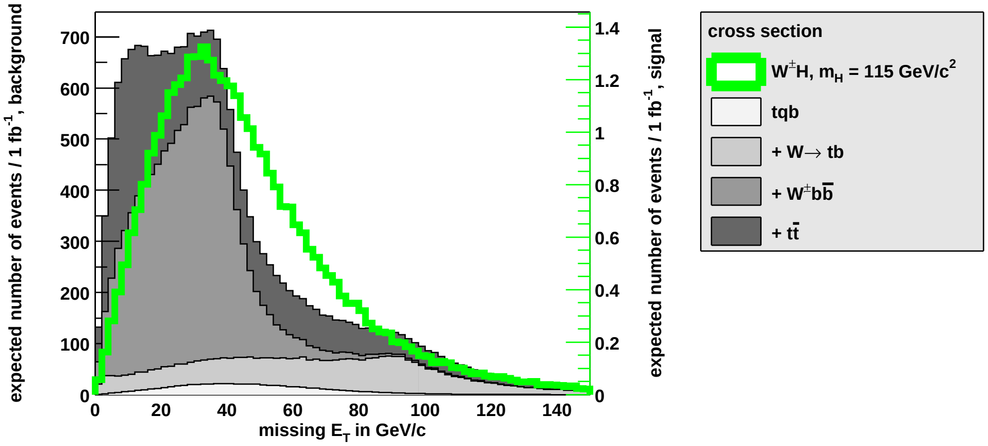

Figure 5.21: *Missing transverse energy in the final state $l^\pm \nu b\bar{b}$, obtained with the* ATLFast *simulation of the* DØ *detector for a Higgs mass of 115 GeV/c^2*

the $W^\pm b\bar{b}$ process the vast majority of the b-tagged jets found in the final states originates in the splitting of a gluon to a bottom quark-anti-quark pair.

The number distribution for the single top processes labelled $W^{\pm *} \rightarrow tb$ and tqb look very different, although the final state contains one b-jet coming from the splitting of a gluon to a pair of bottom quark and one originating in the decay of a top quark.

This difference can be explained looking at the allowed decays set for the $W^\pm$ in the production of the corresponding Monte Carlo samples. In the case of the $W^{\pm *} \rightarrow tb$ process the $W^\pm$ was allowed to decay leptonically as well as to a top quark and a bottom quark. Thus only some of the events contain the desired final state. This was not the case for the tqb sample, which only includes those intermediate states with a top quark and a bottom quark in the final state.

Comparing the signal processes for both final states $l^+l^-b\bar{b}$ and $l^\pm\nu b\bar{b}$ and the background process $W^\pm Z^0$ one finds that the number distributions for b-tagged jets almost comply with each other, only for Higgs masses higher than the Z^0 boson mass a higher number of two-jet events is found.

Especially in case of the signal process the events reconstructed with the PGS simulation include more b-jets than those events coming from the ATLFast simulation. The difference is consistent with what has been observed for the Z^0H final state. In the analysis less of the $W^\pm H$ events obtained with the PGS simulation are rejected by the demand of two b-jets in the final state.

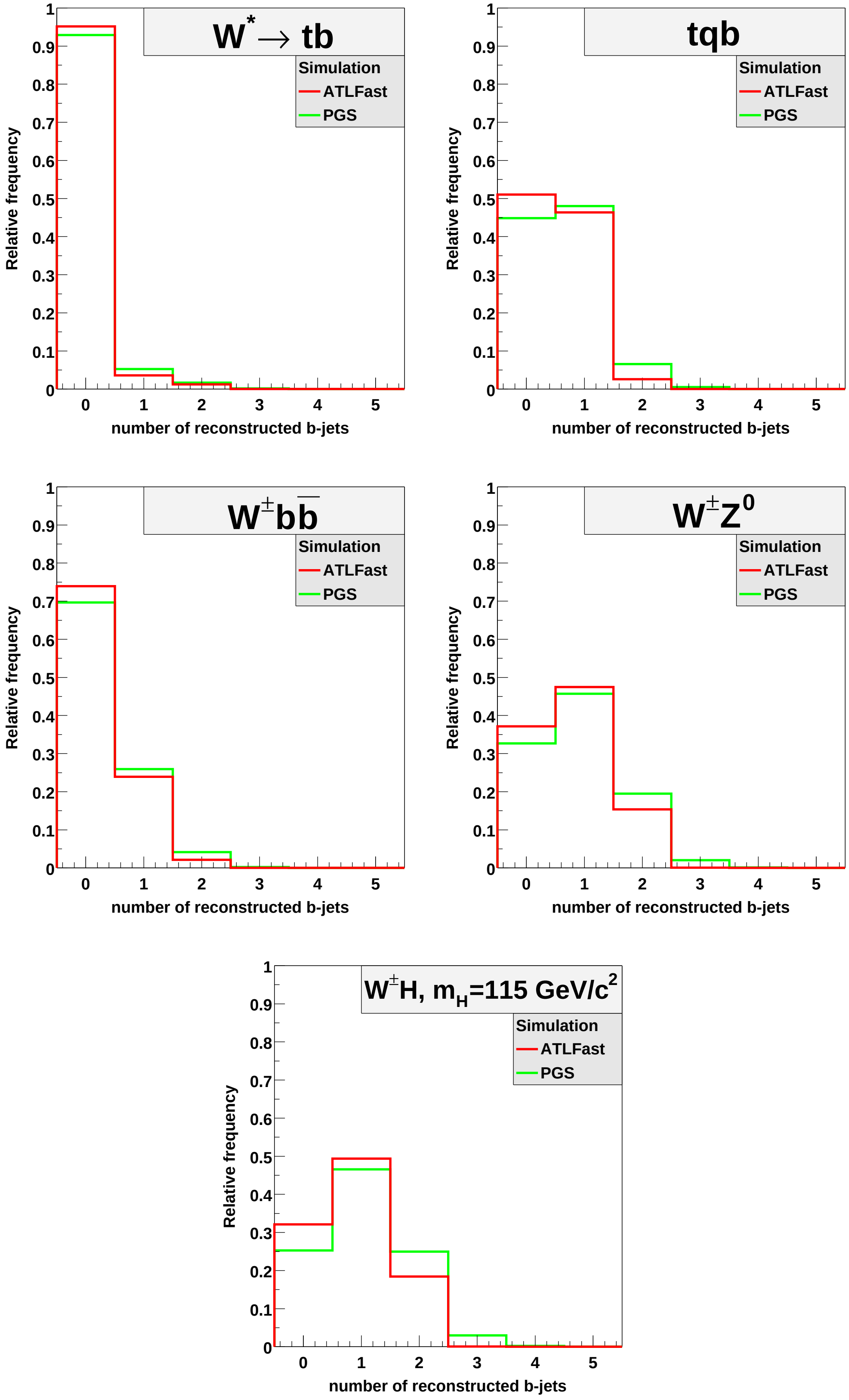

Figure 5.22: *Number of b-tagged jets for DØ, final state* $l\nu b\bar{b}$

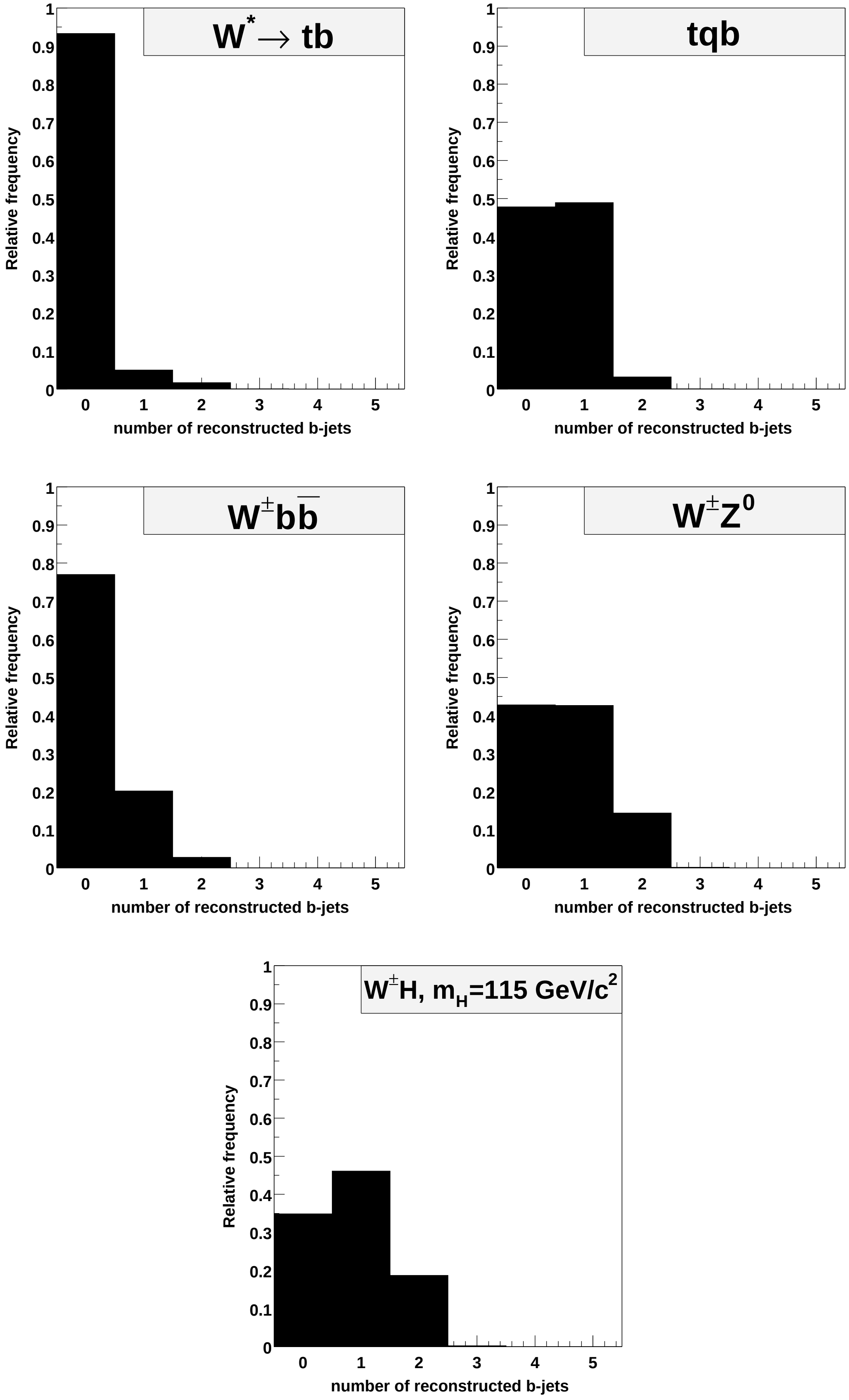

Figure 5.23: *Number of b-tagged jets for ATLAS, final state* $l\nu b\bar{b}$

Number distribution of reconstructed charged light leptons

The number distributions for the processes with a final state resembling $\mathrm{l}^{\pm}\nu\mathrm{b}\bar{\mathrm{b}}$ are given in figures 5.25 and 5.26. The distributions for background and signal processes look similar, which means that in the leptonic channel the different processes – except $\mathrm{b}\bar{\mathrm{b}}$ and $\mathrm{t}\bar{\mathrm{t}}$ – in most cases produce events with at least one isolated electron or muon in the final state.

From the plots one can see a difference between the ATLAS detector and the DØ detector reconstruction performance for light charged leptons. This difference is explained by the very different transverse momentum distributions of the final state lepton (see figure 5.25). In the case of the PGS simulation a significant increase in the number of leptons with low transverse momentum is observed. This effect is also found for the final state $\mathrm{l}^{+}\mathrm{l}^{-}\mathrm{b}\bar{\mathrm{b}}$. These surplus leptons most likely are falsely identified as isolated.

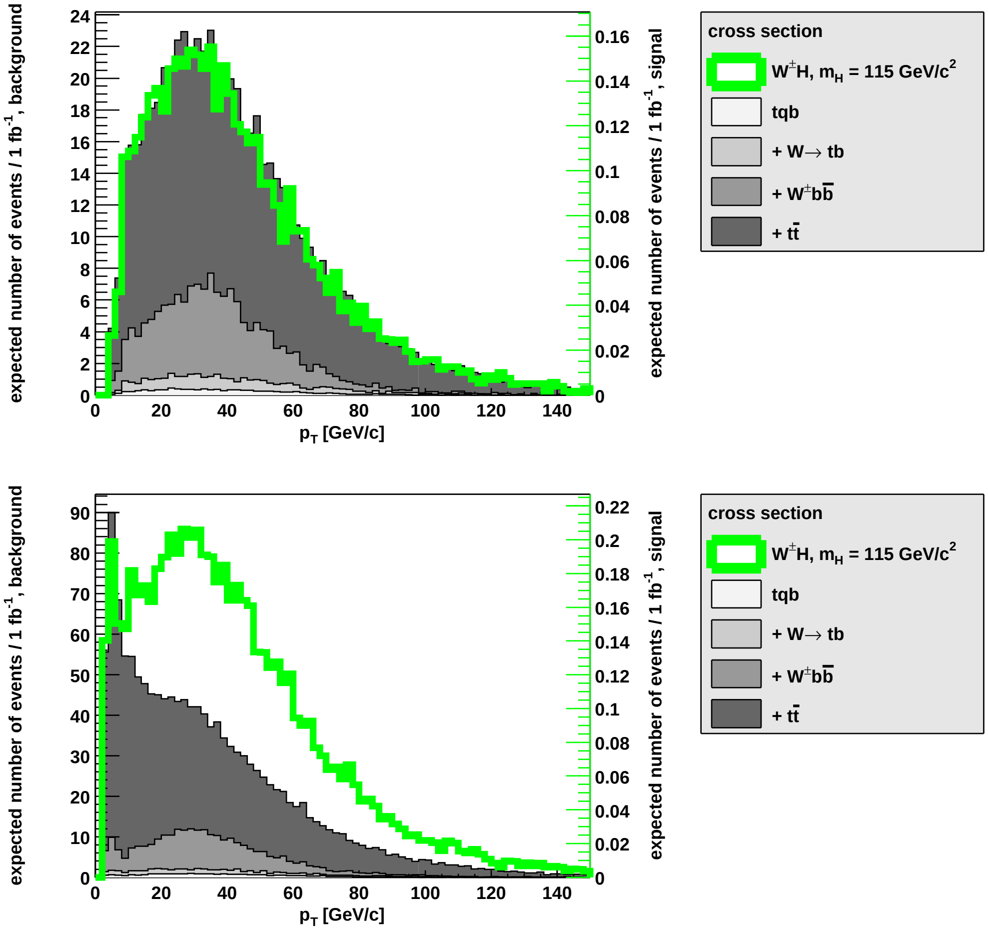

Figure 5.24: *Differences in the p_T distribution for the light lepton in the final state $l^{\pm}\nu b\bar{b}$ between the ATLFast (top) and the PGS (bottom) simulation of the DØ detector*

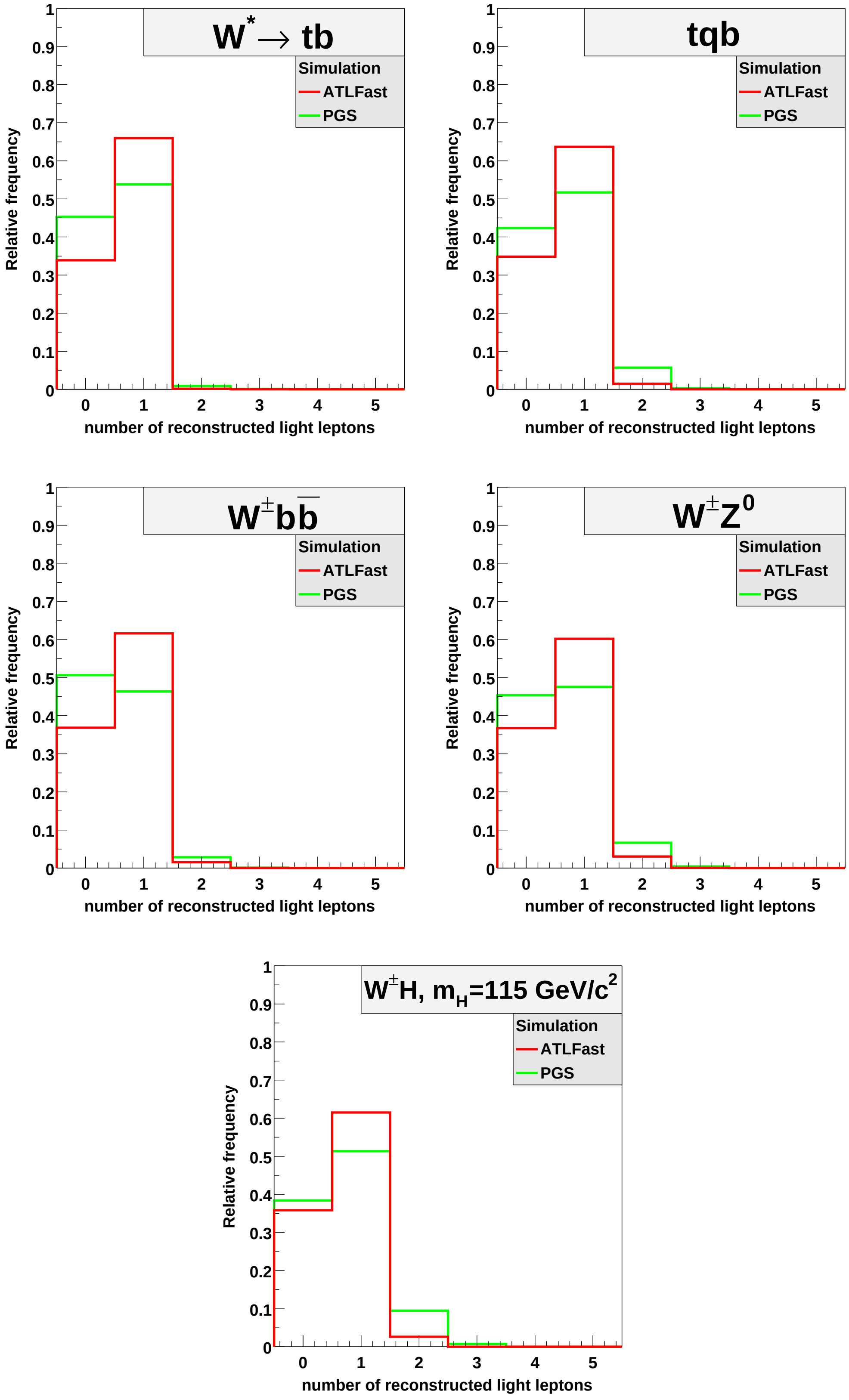

Figure 5.25: *Number of leptons for DØ, final state $l\nu b\bar{b}$*

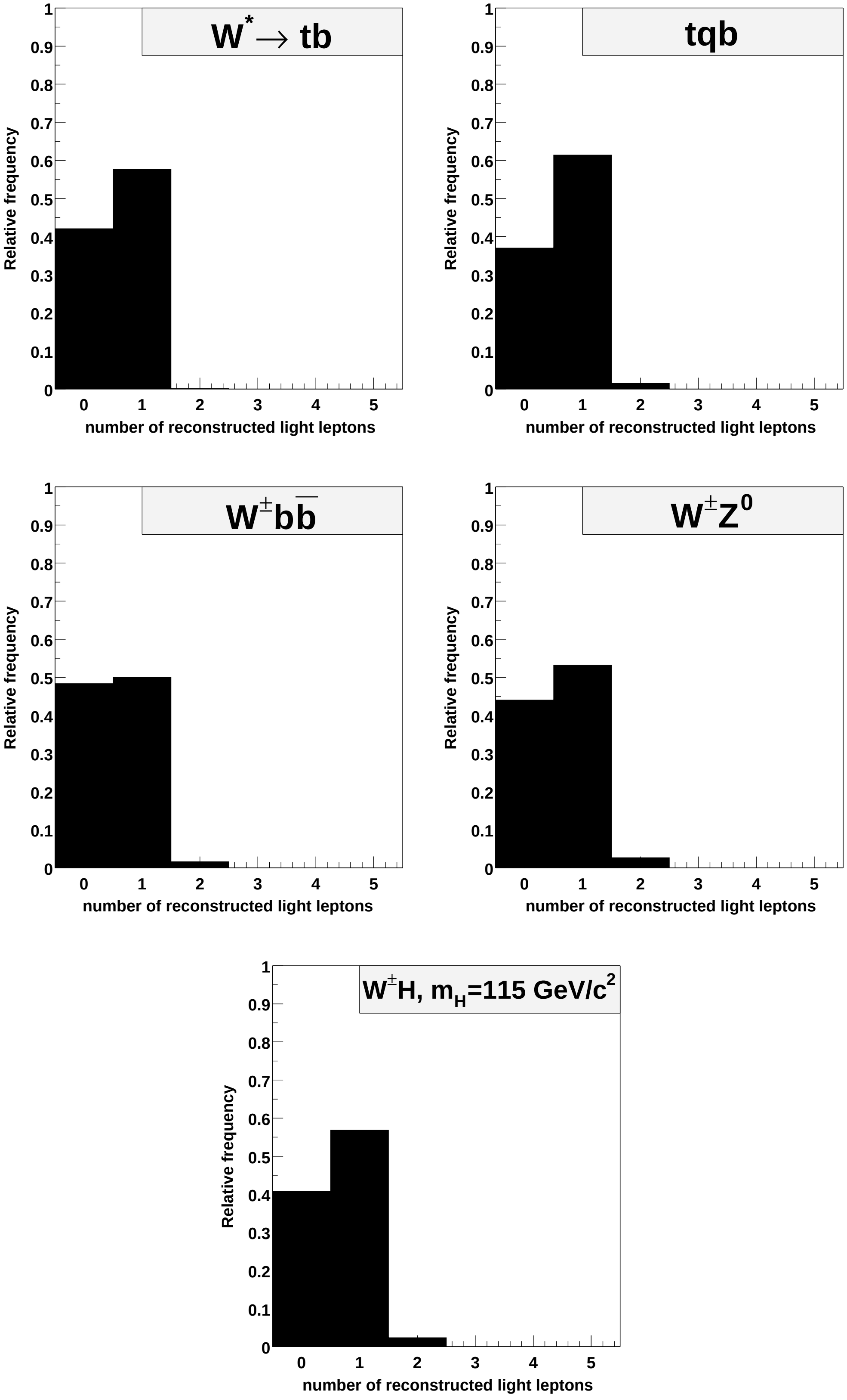

Figure 5.26: *Number of leptons for ATLAS, final state* $l\nu b\bar{b}$

Accepted cross sections for the final state $l\nu b\bar{b}$

As acceptance criteria for the final state labelled $l^{\pm}\nu b\bar{b}$ an event is required to include:

- Two bottom flavour-tagged jets
- One light charged leptons

A pre-selection for missing energy was left out since this selection would require a precise knowledge and correct simulation of the energy loss due to detector inefficiencies.

Regarding the selection criteria listed above one obtains the fractions of accepted events found in table 5.2. For the $W^{\pm}b\bar{b}$ process the combined cross section for all lepton flavours is cited.

Table 5.2: **Accepted cross sections for the final state $l\nu b\bar{b}$**

Process	surviving events [%]		accepted cross section [fb]	
	DØ	ATLAS	DØ	ATLAS
$W^{\pm}H$, $m_H = 90$ GeV/c^2	14.3 (18.2)	9.4	13 (17)	84
$W^{\pm}H$, $m_H = 115$ GeV/c^2	16.0 (20.1)	11.6	5.8 (7.2)	45
$W^{\pm}H$, $m_H = 120$ GeV/c^2	16.4 (20.6)	12.0	4.8 (6.0)	38
$W^{\pm}H$, $m_H = 125$ GeV/c^2	16.6 (20.7)	12.0	3.7 (4.6)	31
$W^{\pm}H$, $m_H = 130$ GeV/c^2	16.7 (20.9)	12.5	2.9 (3.7)	25
$b\bar{b}$	5.7×10^{-4} (0.024)	≈ 0	2.6×10^{5} (1.1×10^{7})	≈ 0
$t\bar{t}$	9.7 (17.0)	10.0	640 (1100)	6.6×10^{4}
$W^{\pm *} \rightarrow tb$	1.0 (1.3)	0.98	32 (42)	350
tqb	2.5 (5.5)	1.9	15 (34)	1500
$W^{\pm}b\bar{b}$	1.9 (4.0)	1.5	180 (370)	1900
$W^{\pm}Z^{0}$	13.1 (15.1)	7.9	17.2 (19.8)	115

Accepted fraction of events and cross sections for the final state $l\nu b\bar{b}$

Table 5.2 clearly shows the differences between the ATLFAST and PGS simulation. For the signal processes the accepted cross section varies about twenty to twenty-five percent, for background processes the differences can vary by a factor of two.

As was mentioned in section 5.2.1 on page 101 the electron reconstruction efficiency is underestimated by the PGS simulation while the b-tagging efficiency is overestimated. The net effect if both effects are combined gives lower (and more realistic) acceptance values.

If, for example, one considers the inclusive $\mathrm{W^{\pm}b\bar{b}}$ sample, 63 % off all events include two OSSF leptons in case of the ATLFast simulation while only 49 % survive in case of the PGS simulation. Of the remaining events reconstructed by the ATLFast simulation about 1.6 % survive the double b-jet test, while this value is 8 % for the PGS simulation.

For all Monte Carlo samples containing bottom quarks originating from the decay of particles with a low mass, like gluons, the difference in the b-tagging efficiency is the dominant effect which leads to different acceptance values.

From these observations one can conclude that the ATLFast packages better simulates the true DØ detector response than the PGS reconstruction software, because b-tagging and electron identification efficiency better resemble the upgraded DØ detector performance.

5.3.2 Selection of kinematic variables

The selection of kinematic variables again follows [25, 62, 63]. No full kinematic reconstruction of the final state $\mathrm{l^{\pm}\nu b\bar{b}}$ is possible because the neutrino momentum vector cannot be fully reconstructed.

Instead the transverse missing energy can be calculated from the event information, which only partially resembles the neutrino information and is also influenced by detection inefficiencies.

Nevertheless an event with a high value of missing energy is likely to contain an undetected neutrino in the final state. Thus the selected kinematic variables are

1. **Missing transverse energy**, $\mathrm{E_T}$
2. **Transverse momentum**, $\mathrm{p_T}$, of b-jets and the single charged light lepton
3. **Pseudorapidity**, η, of b-jets and the single charged light lepton
4. **Invariant mass** of the b-jet pair

Those events containing tau leptons in the final state are expected to include a neutrino from the decay of the tau lepton which adds to the observed missing energy.

Possible non-b-jet contributions are included by the choice of the

- **Transverse momentum** of jets with no bottom flavours an the
- **Pseudorapidity** of jets with no bottom flavours

5.3.3 Selection of events

Although the associated production of a Higgs boson with a $W^{\pm}$ boson and a Z^0 are similar, the corresponding background processes are not. The kinematic constraints have been adopted to this difference by raising the minimum value for the transverse b-jet momentum and for the single final state lepton.

The abbreviations introduced in 5.3.3 are retained in the following text, the missing transverse energy is specified by E_T^{miss}.

Selection criteria for a center of mass energy of 2 TeV

The constraints set for the kinematic variables at a center of mass energy of 2 TeV were set to [25]

1. One lepton with $p_T > 20$ GeV/c in $|\eta| < 2.0$
2. No second lepton with $p_T > 10$ GeV/c within $|\eta| < 2.0$
3. $E_T^{miss} > 20$ GeV
4. Two b-jets in the region $|\eta| < 2.0$
    - one with $p_T > 30$ GeV/c
    - the other with $p_T > 15$ GeV/c
5. A maximum of one additional jet with $p_T > 15$ GeV/c within $|\eta| < 2.5$
6. No additional jet with $p_T > 30$ GeV/c within $|\eta| < 2.5$
7. $|m_{b\bar{b}} - m_H| < 30\ \%\ m_H$

where he newly introduced lower bound on the missing transverse energy helps to select those events with a high-energy neutrino in the final state.

Selection criteria for a center of mass energy of 14 TeV

The kinematic cuts for a center of mass energy of 14 TeV were chosen as follows [63]

1. One lepton with $p_T > 20$ GeV/c in $|\eta| < 2.5$
2. No second lepton with $p_T > 6$ GeV/c within $|\eta| < 2.5$
3. Two b-jets $p_T > 15$ GeV/c in the region $|\eta| < 2.0$
4. No additional jet with $p_T > 15$ GeV/c within $|\eta| < 5.0$
5. $|m_{b\bar{b}} - m_H| < 20\ \%\ m_H$

No missing energy cut was chosen for the center of mass energy of 14 TeV, since the contribution to the missing transverse energy coming from the single neutrino in the final state is much harder to reconstruct and does not allow for a good estimate of the neutrino energy.

Chapter 6

Results

6.1 Results for the channel $l^+l^-b\bar{b}$

6.1.1 Efficiencies of the kinematic selection criteria

Efficiencies for a center of mass energy of 2 TeV

The reduction efficiencies for the kinematic cuts introduced in section 5.2.3 quoted in table 6.1 are obtained with the ATLFAST simulation, the figures in parentheses give the values obtained with the PGS simulation. The labels given in the second row correspond to these cuts.

For the final reduction efficiency listed in the last column they differ by a factor of two for the background processes while for the signal process the difference is given by a factor of 1.5. These factors originate in the different lepton and b-jet reconstruction efficiencies used in the ATLFAST and PGS reconstruction. For the background processes these differences have a greater effect than for the signal process.

The requirement of two b-jets with high transverse momentum mainly reduces the $b\bar{b}$ and $Z^0b\bar{b}$ background. For the $t\bar{t}$ sample this constraint only selects those events with exactly two b-jets in the final state, owing to the fact that most of the b-jets in this sample originate from the decay of a heavy top-quark.

Demanding two OSSF leptons in the final state reduces the $t\bar{t}$ by a factor of 3000. With this cut no events of the $b\bar{b}$ background are left for the sample sizes considered, which is denoted by ≈ 0. For the – inclusive – $Z^0b\bar{b}$ and Z^0Z^0 samples this cut mainly selects final states with exactly two leptons.

Constraining the invariant mass of the lepton pair again reduces the $t\bar{t}$ background but leaves the $Z^0b\bar{b}$ and Z^0Z^0 background almost untouched, since for these two backgrounds the lepton pair also originates in a Z^0 boson decay.

The effect of a test on additional jets is marginal for all processes.

Table 6.1: **Reduction efficiencies for $l^+l^-b\bar{b}$ at the Tevatron center of mass energy**

Process	Fraction of surviving events [%]			
Cut	2 b-jets	2 leptons	$m_{l^+l^-}$	add. jets
Z^0H, $m_H = 90$ GeV/c^2	20.2 (59.0)	8.7 (16.5)	7.7 (14.1)	7.6 (12.7)
Z^0H, $m_H = 115$ GeV/c^2	22.8 (62.0)	9.9 (18.0)	8.7 (15.4)	8.6 (13.6)
Z^0H, $m_H = 120$ GeV/c^2	23.3 (62.3)	10.0 (18.1)	8.9 (15.4)	8.8 (13.6)
Z^0H, $m_H = 125$ GeV/c^2	23.6 (62.7)	10.1 (18.4)	9.0 (15.7)	8.9 (13.8)
Z^0H, $m_H = 130$ GeV/c^2	24.0 (62.8)	10.3 (18.4)	9.1 (15.7)	9.0 (13.8)
$b\bar{b}$	0.17 (0.28)	≈ 0 (≈ 0)	≈ 0 (≈ 0)	≈ 0 (≈ 0)
$t\bar{t}$	7.0 (31.3)	2.3×10^{-3} (0.021)	4.9×10^{-5} (2.2×10^{-4})	4.7×10^{-5} (1.3×10^{-4})
$Z^0b\bar{b}$	3.4 (13.2)	1.3 (3.5)	1.0 (2.7)	1.0 (2.4)
Z^0Z^0	19.7 (30.8)	3.4 (6.5)	2.7 (5.0)	2.7 (4.5)

Reduction efficiencies of the kinematic cuts for the final state $l^+l^-b\bar{b}$ at a center of mass energy of 2 TeV obtained with the ATLFast simulation. Numbers in parentheses give the corresponding PGS values

Efficiencies for a center of mass energy of 14 TeV

For a center of mass energy of 14 TeV the reduction efficiencies for the kinematic cuts described in section 5.2.3 are listed in table 6.2.

Compared to the values calculated for the TEVATRON center of mass energy the selection criteria yield similar values for the overall efficiencies for signal and background. The performance for the $t\bar{t}$ and Z^0Z^0 background is found to be slightly enhanced, while a decrease is observed if the signal process is regarded.

It has to be pointed out that the reduction efficiencies only give the relative factor of reduction. Although the TEVATRON and ATLAS values are comparable the cross sections for the background processes at the LHC center of mass energy scale with much higher factors than the signal processes.

Table 6.2: **Reduction efficiencies for $l^+l^-b\bar{b}$ at the LHC center of mass energy**

Process	Fraction of surviving events [%]			
Cut	2 leptons	$m_{l^+l^-}$	2 b-jets	add. jets
Z^0H, $m_H = 90$ GeV/c^2	32.8	27.0	5.0	4.9
Z^0H, $m_H = 115$ GeV/c^2	34.4	28.4	6.4	6.2
Z^0H, $m_H = 120$ GeV/c^2	34.8	28.8	6.6	6.5
Z^0H, $m_H = 125$ GeV/c^2	35.0	29.1	6.7	6.6
Z^0H, $m_H = 130$ GeV/c^2	35.4	29.4	7.0	6.8
$b\bar{b}$	≈ 0	≈ 0	≈ 0	≈ 0
$t\bar{t}$	0.27	1.5×10^{-4}	1.0×10^{-5}	9.4×10^{-6}
$Z^0b\bar{b}$	44.0	34.9	1.3	1.3
Z^0Z^0	19.2	14.8	2.0	2.0

Reduction efficiencies of the kinematic cuts for the final state $l^+l^-b\bar{b}$ at a center of mass energy of 14 TeV

6.1.2 Expected number of events and significance

Expected number of events at a center of mass energy of 2 TeV

To give an estimate of the detection capabilities of the DØ detector for a Higgs boson produced in association with a Z^0 boson table 6.3 lists the expected number of events for an integrated luminosity of 10 fb^{-1} for the signal process Z^0H and the corresponding background processes.

To obtain a feeling for the ratios of signal and background a simple Gaussian approximation to the significance s is used:

$$s = S/\sqrt{B_{tot}} \tag{6.1}$$

where S is the number of expected signal events and B_{tot} the number of expected events for the total background. It is a measure to decide if the number of detected events is consistent with the assumption that a Higgs boson was observed. A significance value of three, also called a 3σ OBSERVATION, is an indication that a Higgs signal might have be observed. A discovery can be claimed for a significance value of five.

Two different values for the significance are found in table 6.3. The first one gives the ratio for $S/\sqrt{B_{con}}$ before the final cut of ±30 % m_H is applied to the data. This so called mass window cut rejects all the events for which the invariant mass of the reconstructed b-jet pair is not found in a range of ±30 % m_H around the true Higgs mass.

Table 6.3: **Expected number of events for processes with the final state $l^+l^-b\bar{b}$ at 2 TeV center of mass energy**

Process	Higgs mass [GeV/c^2]				
	90	115	120	125	130
without mass cut					
Z^0H	13 (21)	6 (9)	5 (8)	4 (6)	3 (5)
$t\bar{t}$	45 (74)				
$Z^0b\bar{b}$	177 (427)				
B_{con}	222 (501)				
$S/\sqrt{B_{con}}$	0.87 (0.94)	0.40 (0.40)	0.34 (0.36)	0.27 (0.27)	0.20 (0.22)
Z^0Z^0	23 (39)				
B_{tot}	245 (540)				
30% m_H mass cut					
mass window [GeV/c^2]	63-117	80.5-149.5	84-156	87.5-162.5	91-169
Z^0H	12 (18)	5 (8)	4 (7)	4 (5)	3 (4)
$t\bar{t}$	14 (28)	17 (29)	17 (29)	18 (28)	19 (29)
$Z^0b\bar{b}$	68 (126)	48 (89)	44 (83)	42 (75)	38 (71)
B_{con}	82 (154)	65 (118)	61 (112)	60 (103)	57 (100)
$S/\sqrt{B_{con}}$	1.3 (1.45)	0.62 (0.73)	0.51 (0.66)	0.51 (0.49)	0.40 (0.40)
Z^0Z^0	21 (33)	18 (25)	17 (22)	15 (18)	13 (15)
B_{tot}	103 (187)	83 (143)	78 (134)	75 (121)	70 (115)
$S/\sqrt{B_{tot}}$	1.18 (1.32)	0.55 (0.67)	0.45 (0.60)	0.46 (0.45)	0.36 (0.37)

Expected number of events at an integrated luminosity of 10 fb^{-1}, final state $l^+l^-b\bar{b}$, center of mass energy 2 TeV. Numbers in parentheses give the corresponding PGS values.

The significance value obtained if the mass-window cut is not applied helps to estimate if a signal peak corresponding to a Higgs boson can be separated from the background mass spectrum. The smaller this significance value the less it is probable that a separation will be possible. The most dominant background contribution to the continuous background comes from the $Z^0b\bar{b}$ process.

For higher Higgs masses a separation becomes more difficult. Here two competing effects have to be considered. On the one hand if the Higgs mass is increased the cross section for associated Higgs production decreases and the

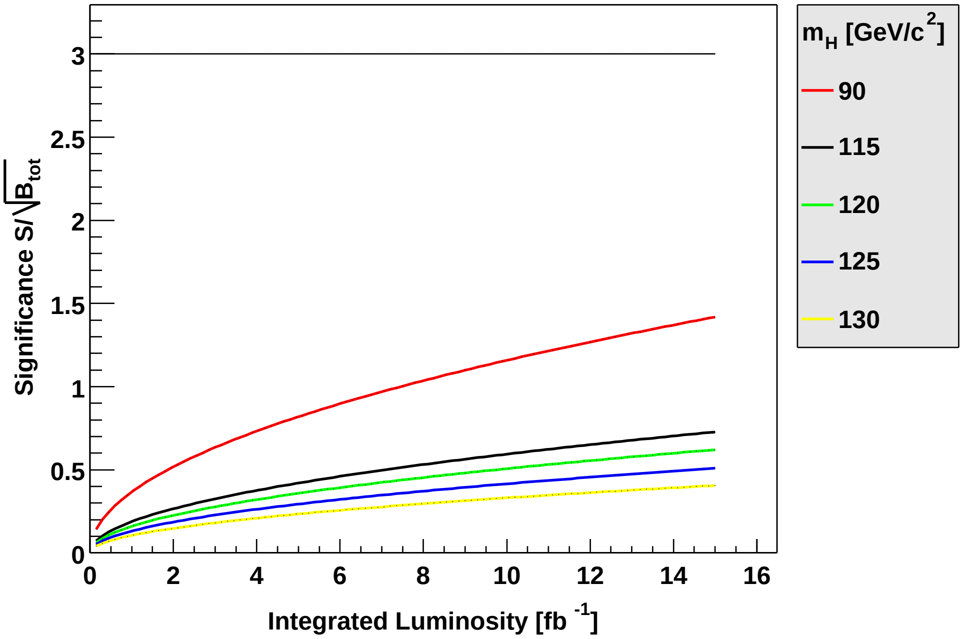

Figure 6.1: *Significance v.s integrated luminosity for the Z^0H process at a center of mass energy of 2 TeV.*

observed peak in the mass spectrum shrinks. On the other hand the peak in the mass spectrum caused by the resonant background process Z^0Z^0 and the Higgs mass peak are more separated.

It is clear from the values given in table 6.3 that a further reduction of the background contribution is needed to better distinguish the Higgs mass peak from the background mass spectrum.

The final values for the significance after the mass window cut has been applied are found to be in good agreement[1] with [25]. The chosen range of the mass window cut assumes a mass resolution of $\delta m_H/m_H$ of 15%, the value achieved with the DØ detector in Run I.

The number of expected events related to the PGS simulation – which are put in parentheses behind the ATLFAST related number – are of a factor two higher for the background processes and of a factor 1.5 for the signal processes. These deviations are mainly caused by the different reconstruction efficiencies for light leptons and b-tagged jets implemented in ATLFAST and PGS. The net effect of these differences results in comparable values for the significance.

Figure 6.2 shows the significance (after the mass window cut has been applied) for the Z^0H process depending on the integrated luminosity. The graphs correspond to the values obtained with the ATLFAST detector simulation.

---

[1] The values in [25] are given for an integrated luminosity of 2 fb^{-1}. The values in this study thus have to be divided by $\sqrt{5}$ to resemble the Tevatron Higgs working group numbers

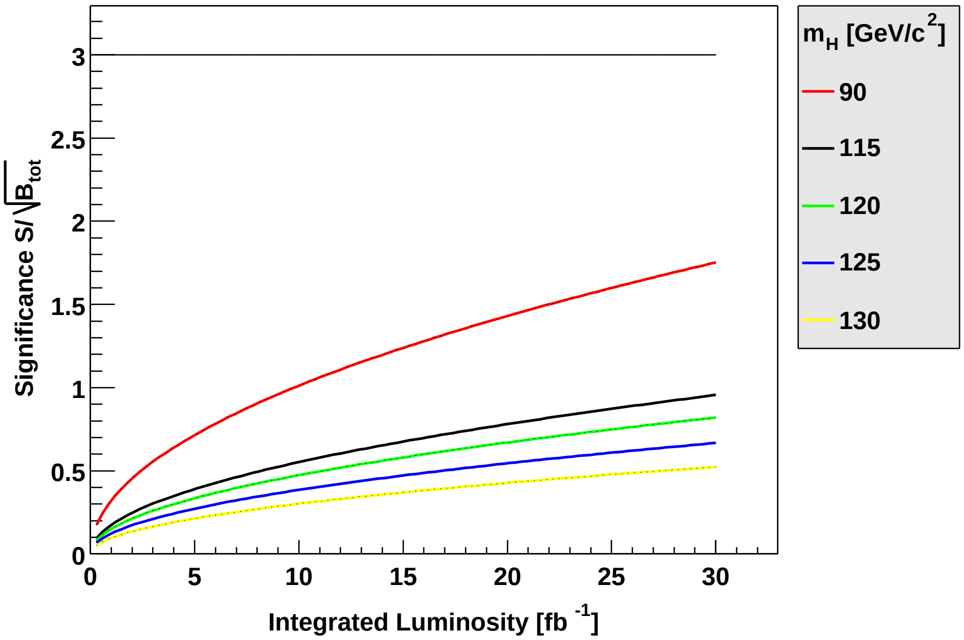

Figure 6.2: *Significance v.s integrated luminosity for the Z^0H process at a center of mass energy of 14 TeV.*

Expected number of events at a center of mass energy of 14 TeV

At a center of mass energy of 14 TeV the number of background processes (not taking into account the mass window cut) increases by a factor of 130-160 if compared to the TEVATRON values. For the signal process this factor is about 13.

The significance values calculated before and after applying the mass window constraint are higher than at a center of mass energy of 2 TeV and are in agreement with the values cited in [63]. The dominant background contribution comes from the $Z^0b\bar{b}$ background as was the case for the TEVATRON center of mass energy.

The significance[2] for the Z^0H process depending on the integrated luminosity is plotted in figure 6.2 for all Higgs mass values studied.

---

[2] after the mass window cut has been applied

Table 6.4: **Expected number of events for processes with the final state $l^+l^-b\bar{b}$ at 14 TeV center of mass energy**

Process	Higgs mass [GeV/c^2]				
	90	115	120	125	130
without mass cut					
Z^0H	220	122	105	87	69
$t\bar{t}$	6072				
$Z^0b\bar{b}$	30715				
B_{con}	36787				
$S/\sqrt{B_{con}}$	1.14	0.64	0.55	0.45	0.31
Z^0Z^0	504				
B_{tot}	37291				
20% m_H mass cut					
mass window [GeV/c^2]	72-108	92-138	96-144	100-150	104-156
Z^0H	165	87	75	60	47
$t\bar{t}$	1122	1518	1782	1782	1980
$Z^0b\bar{b}$	7404	6694	6495	6339	6195
B_{con}	8526	8212	8277	8121	8175
$S/\sqrt{B_{con}}$	1.8	0.96	0.82	0.67	0.52
Z^0Z^0	377	140	89	51	30
B_{tot}	8903	8352	8366	8172	8205
$S/\sqrt{B_{tot}}$	1.75	0.95	0.82	0.66	0.52

Expected number of events at an integrated luminosity of 30 fb^{-1}*, final state* $l^+l^-b\bar{b}$*, center of mass energy 14 TeV*

6.2 Results for the channel $l^\pm \nu b\bar{b}$

6.2.1 Efficiencies of the kinematic selection criteria

Efficiencies for a center of mass energy of 2 TeV

Table 6.5 lists the reduction efficiencies for the kinematic cuts defined in section 5.3.3. One light charged lepton with a minimum transverse momentum of 20 GeV/c is required in the final state. By this selection rule about a half of all signal events are discarded, mainly those events including hadronically decaying taus (about a third of a sample).

The other 20% include leptons outside the reconstruction region and leptons which are not correctly reconstructed. The main purpose of this cut is to reduce the $b\bar{b}$ background contribution. Selecting events accompanied by missing transverse energy decreases the fraction of surviving events for the signal process but also that for the $t\bar{t}$ background.

Table 6.5: **Reduction efficiencies for $l\nu b\bar{b}$ at the Tevatron center of mass energy**

Process	Fraction of surviving events [%]			
Cut	1 lepton	E_T^{miss}	2 b-jets	add. jets
$W^\pm H$, $m_H = 90$ GeV/c^2	49.1 (41.8)	40.9 (35.7)	8.9 (20.6)	8.8 (18.9)
$W^\pm H$, $m_H = 115$ GeV/c^2	50.2 (42.9)	42.4 (37.5)	10.2 (23.5)	10.1 (21.0)
$W^\pm H$, $m_H = 120$ GeV/c^2	50.6 (43.3)	42.7 (37.9)	10.6 (23.5)	10.5 (21.1)
$W^\pm H$, $m_H = 125$ GeV/c^2	50.6 (43.5)	42.9 (38.2)	10.8 (24.3)	10.6 (21.7)
$W^\pm H$, $m_H = 130$ GeV/c^2	50.7 (43.4)	42.8 (38.3)	10.9 (24.4)	10.7 (21.7)
$b\bar{b}$	0.043 (8.6×10^{-4})	0.039 (5.7×10^{-4})	≈ 0 (≈ 0)	≈ 0 (≈ 0)
$t\bar{t}$	6.1 (5.9)	4.9 (5.0)	0.33 (1.7)	0.16 (0.050)
$W^{\pm *} \to tb$	60.4 (51.1)	59.3 (32.7)	0.68 (1.5)	0.67 (1.3)
tqb	51.0 (42.6)	45.0 (38.6)	1.3 (5.7)	1.3 (2.1)
$W^\pm b\bar{b}$	47.7 (37.4)	41.9 (24.9)	0.92 (2.7)	0.92 (2.6)
$W^\pm Z^0$	46.7 (36.8)	39.8 (31.1)	7.6 (15.7)	7.6 (14.2)

Reduction efficiencies of the kinematic cuts for the final state $l\nu b\bar{b}$ at a center of mass energy of 2 TeV

With demanding two b-jets with high transverse momentum the $b\bar{b}$ contribution becomes negligible. Additionally the number of surviving events produced in the $W^{\pm}b\bar{b}$ process is decreased as well as the number of the tqb events in which one of the bottom quark originates from a gluon splitting to a quark-anti-quark pair.

In the case of the $W^{\pm *} \to tb$ process only those events with a top and a bottom quark in the intermediate state are selected[3]. A kinematic veto on jets with no bottom flavour tag here helps to reduce the $t\bar{t}$ background by a factor of two. Differences between the ATLFast and the PGS simulation are less pronounced for the background channels, but instead are bigger for the signal process.

Efficiencies for a center of mass energy of 14 TeV

The reduction efficiencies for the kinematic cuts introduced in section 5.3.3 are found in table 6.6. At the center of mass energy of 14 TeV the efficiency of the kinematic constraints is comparable to those obtained for the Tevatron case. Only the $W^{\pm}Z^0$ process contribution is found to be smaller.

Table 6.6: **Reduction efficiencies for $l\nu b\bar{b}$ at the LHC center of mass energy**

Process	Fraction of surviving events [%]		
Cut	1 leptons	2 b-jets	add. jets
$W^{\pm}H$, $m_H = 90$ GeV/c^2	43.0	7.8	7.5
$W^{\pm}H$, $m_H = 115$ GeV/c^2	46.0	9.7	9.3
$W^{\pm}H$, $m_H = 120$ GeV/c^2	46.2	10.0	9.5
$W^{\pm}H$, $m_H = 125$ GeV/c^2	46.4	10.2	9.8
$W^{\pm}H$, $m_H = 130$ GeV/c^2	46.7	10.5	9.9
$b\bar{b}$	8.6×10^{-4}	≈ 0	≈ 0
$t\bar{t}$	6.4	0.49	0.17
$W^{\pm *} \to tb$	53.7	0.81	0.74
tqb	48.5	1.6	1.4
$W^{\pm}b\bar{b}$	38.4	1.2	1.2
$W^{\pm}Z^0$	40.1	6.2	5.9

Reduction efficiencies of the kinematic cuts for the final state $l\nu b\bar{b}$ at a center of mass energy of 14 TeV

---

[3] Remember that the $W^{\pm}$ boson can also decay leptonically.

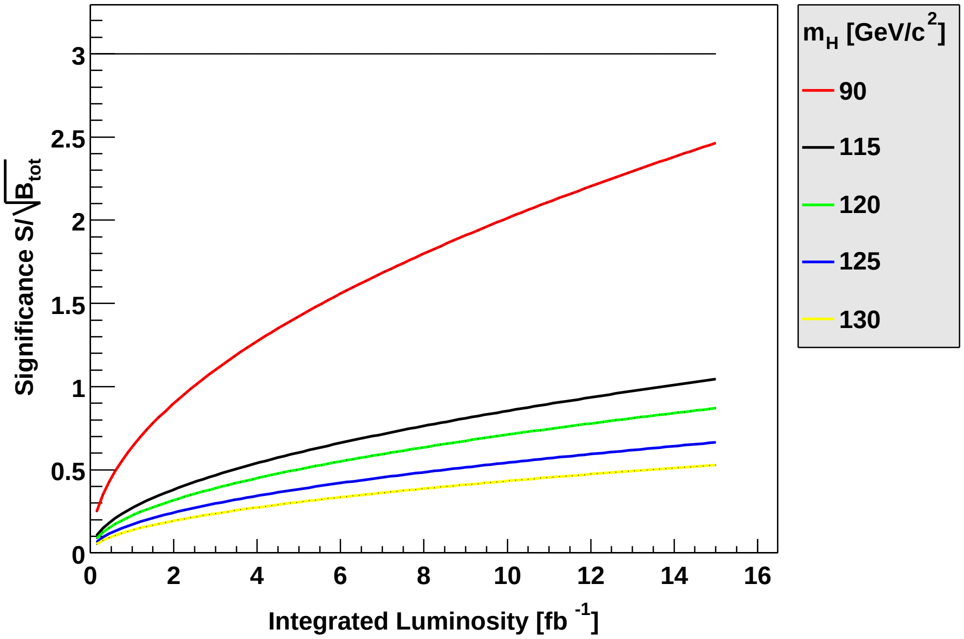

Figure 6.3: *Significance v.s integrated luminosity for the* $W^{\pm}H$ *process at a center of mass energy of 2 TeV.*

6.2.2 Expected number of events and significance

Expected number of events at a center of mass energy of 2 TeV

For the $W^{\pm}H$ signal process and the corresponding backgrounds the numbers of expected events are presented in table 6.7 for an integrated luminosity of 10 fb^{-1}. The selection range for the mass window cut was again chosen to be 30% of the Higgs mass. The values for significance are smaller than those cited in [25], which is caused by differences in the number of surviving events for the $t\bar{t}$ and $W^{\pm}b\bar{b}$ background processes.

These differences are induced by the lepton reconstruction and b-tagging efficiencies. The effects of b-tagging and lepton identification sum up in case of the $W^{\pm}b\bar{b}$ final state while they are competitive for the $t\bar{t}$ background. This shows that the differences in the efficiencies depend on the kinematics of the process involved. The significances calculated from the PGS simulation reduction efficiencies agree with the figures cited in the Tevatron Higgs working group report.

In total the $t\bar{t}$ background becomes much more pronounced than was the case in former studies while the $W^{\pm}b\bar{b}$ background contribution is reduced and the $t\bar{t}$ contribution becomes dominant – see also [63] where the $t\bar{t}$ background is found to be more severe than the $W^{\pm}b\bar{b}$ background. The significances for the process $W^{\pm}H$ after the mass windows cut are plotted in figure 6.3.

Table 6.7: **Expected number of events for processes with the final state $l^{\pm}\nu b\bar{b}$ at 2 TeV center of mass energy**

Process	Higgs mass [GeV/c^2]				
	90	115	120	125	130
without mass cut					
$W^{\pm}H$	80 (172)	36 (76)	31 (62)	23 (48)	19 (38)
$t\bar{t}$	2649 (1481)				
$W^{\pm *} \to tb$	215 (419)				
tqb	80 (129)				
$W^{\pm}b\bar{b}$	851 (2381)				
B_{con}	3795 (4410)				
$S/\sqrt{B_{con}}$	1.3 (2.6)	0.58 (1.14)	0.50 (0.93)	0.37 (0.72)	0.31 (0.57)
$W^{\pm}Z^0$	99 (187)				
B_{tot}	3894 (4597)				
30% m_H mass cut					
mass window [GeV/c^2]	63-117	80.5-149.5	84-156	87.5-162.5	91-169
$W^{\pm}H$	75 (151)	33 (65)	28 (53)	21 (41)	17 (32)
$t\bar{t}$	853 (503)	1113 (627)	1149 (641)	1177 (650)	1202 (661)
$W^{\pm *} \to tb$	81 (153)	101 (179)	103 (179)	104 (178)	103 (180)
tqb	35 (34)	38 (36)	38 (37)	39 (35)	37 (34)
$W^{\pm}b\bar{b}$	317 (648)	193 (396)	181 (358)	163 (321)	149 (295)
B_{con}	1286 (1338)	1445 (1238)	1471 (1215)	1483 (1184)	1491 (1170)
$S/\sqrt{B_{con}}$	2.1 (4.1)	0.87 (1.85)	0.73 (1.52)	0.55 (1.19)	0.44 (0.94)
$W^{\pm}Z^0$	92 (162)	78 (117)	72 (102)	64 (85)	54 (67)
B_{tot}	1378 (1500)	1523 (1355)	1543 (1317)	1547 (1269)	1545 (1237)
$S/\sqrt{B_{tot}}$	2.02 (3.9)	0.84 (1.77)	0.71 (1.46)	0.53 (1.15)	0.43 (0.91)

Expected number of events at an integrated luminosity of 10 fb^{-1}, final state $l^{\pm}\nu b\bar{b}$, center of mass energy 2 TeV. Numbers in parentheses give the corresponding PGS values.

Table 6.8: **Expected number of events for processes with the final state $l^{\pm}\nu b\bar{b}$ at 14 TeV center of mass energy**

Process	Higgs mass [GeV/c^2]				
	90	115	120	125	130
without mass cut					
$W^{\pm}H$	2001	1084	915	763	592
$t\bar{t}$	805992				
$W^{\pm *} \rightarrow tb$	7970				
tqb	33384				
$W^{\pm}b\bar{b}$	46543				
B_{con}	893889				
$S/\sqrt{B_{con}}$	2.1	1.1	0.97	0.81	0.63
$W^{\pm}Z^0$	2583				
B_{tot}	896472				
20% m_H mass cut					
mass window [GeV/c^2]	72-108	92-138	96-144	100-150	104-156
$W^{\pm}H$	1533	774	646	533	408
$t\bar{t}$	161172	205590	211926	216876	219384
$W^{\pm *} \rightarrow tb$	1584	2174	2160	2138	2088
tqb	7192	8736	8845	8970	8845
$W^{\pm}b\bar{b}$	8501	6592	6244	5895	5573
B_{con}	178449	223092	229175	233879	235890
$S/\sqrt{B_{con}}$	3.63	1.64	1.35	1.10	0.84
$W^{\pm}Z^0$	1975	707	425	226	119
B_{tot}	180424	223779	229600	234105	236009
$S/\sqrt{B_{tot}}$	3.61	1.64	1.35	1.10	0.84

Expected number of events at an integrated luminosity of 30 fb^{-1}, final state $l^{\pm}\nu b\bar{b}$, center of mass energy 14 TeV

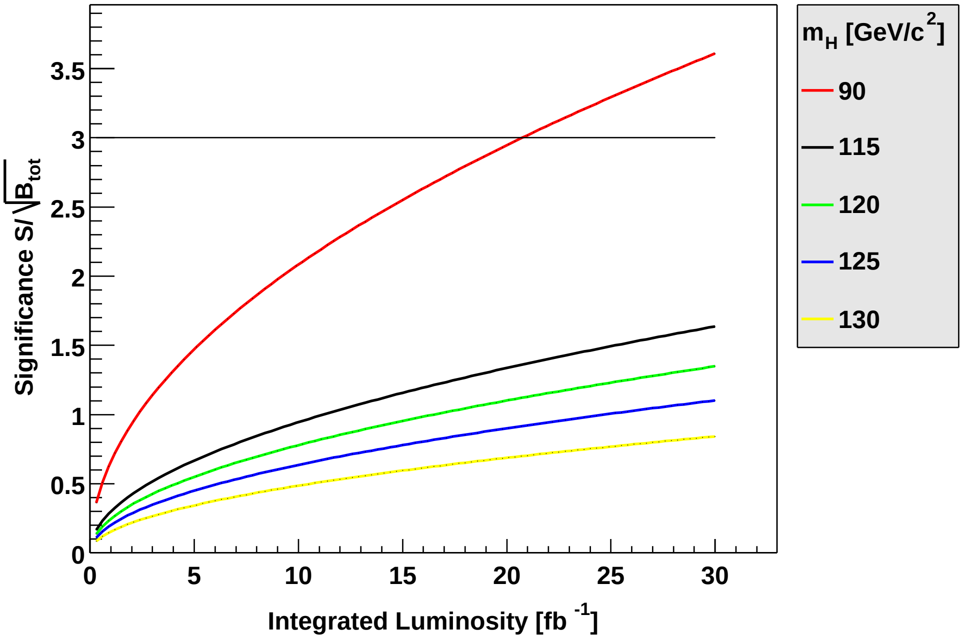

Figure 6.4: *Significance v.s integrated luminosity for the $W^{\pm}H$ process at a center of mass energy of 14 TeV.*

The values for the significances listed in table 6.8 are consistent with the results given in [63].

Similar to the case of 2 TeV center of mass energy the most dominant background contribution comes from the $t\bar{t}$ process. Nevertheless this contribution has to be interpreted with caution. Although the reduction efficiency for the $t\bar{t}$ background leads to a number of over 800000 surviving events this number is greatly influenced by the cross section for the $t\bar{t}$ process at 14 TeV center of mass energy.

A small change in the efficiencies leads to a big change in the surviving number of events, because the reduction efficiency is scaled with the $t\bar{t}$ cross section. In the particular case quoted here this scaling lead to an expected number of events (before the mass-window cut) more than twice as high as the original sample size.

A sample size with at least ten million events would give a better estimate of the influence of the $t\bar{t}$ process on the total background. As was pointed out available disk space did not allow for sample sizes of this order.

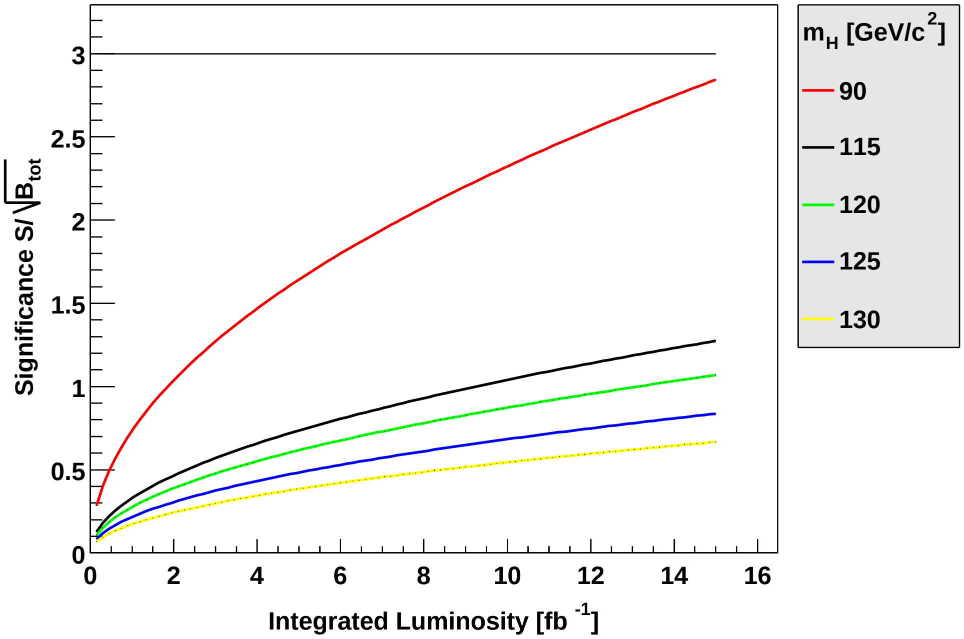

Figure 6.5: *Significance v.s integrated luminosity for the combined signal processes at a center of mass energy of 2 TeV.*

6.2.3 Combination of the results obtained for the signal process Z^0H and $W^{\pm}H$

Figure 6.5 shows the combined significances for both signal processes $W^{\pm}H$ and Z^0H at a center of mass energy of 2 TeV.

The significances for both the $W^{\pm}H$ and Z^0H processes are comparable and too low to allow for the discovery of a Higgs boson in one channel alone. Only with a combination of the channels it can be hoped that a discovery of a Higgs in the intermediate mass range becomes possible.

The significances obtained in the previous chapters quantify the deviations from the pure background signal caused by a possible Higgs produced in association with a gauge boson. Since these deviations are small the Gaussian approach can only be an approximation. Nevertheless it gives an estimate of the gain in significance a combination of the channels allows for.

Staying with the simple Gaussian approximation the total significance is given by

$$S_{tot} = \sqrt{(S_{\mathrm{W^{\pm}H}})^2 + (S_{\mathrm{Z^0H}})^2}$$

as an estimate of the discovery potential if the results for both channels are combined. One can see that even the combination of the two channels does not increase the significance sufficiently (see also chapter 7).

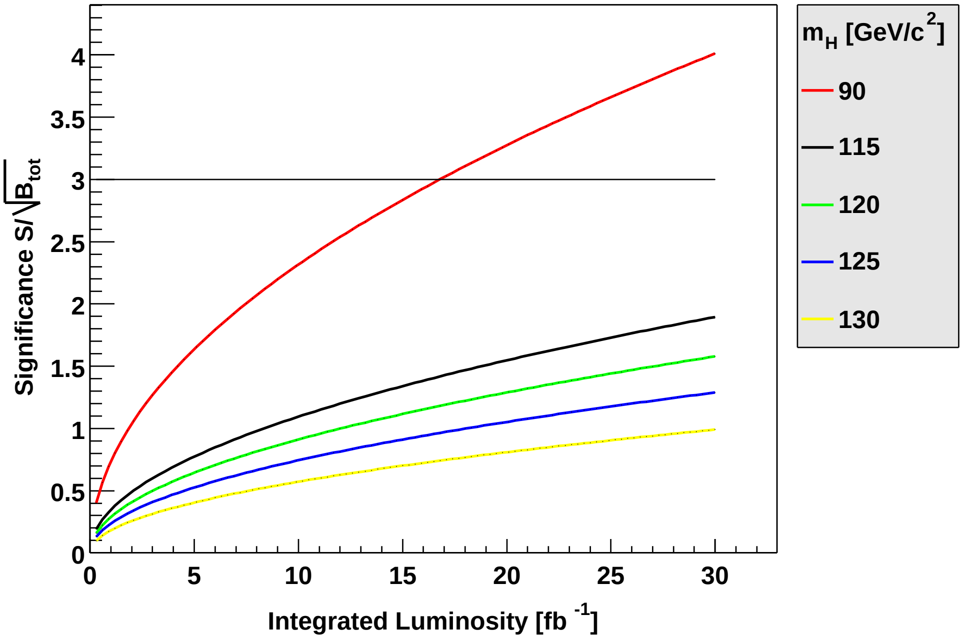

Figure 6.6: *Significance v.s integrated luminosity for the combined signal processes at a center of mass energy of 14 TeV.*

For a center of mass energy of 14 TeV the combined significances are plotted in figure 6.6 for all studied Higgs masses.

An integrated luminosity of 30 fb^{-1} corresponds to a nominal run time of three years at low luminosity for the LHC. In this period the discovery of a Higgs boson in the intermediate mass range produced in association with a gauge boson is not possible.

Chapter 7

Conclusion and Outlook

In this thesis the signal processes $Z^0H \rightarrow l^+l^- + b\bar{b}$ and $W^{\pm}H \rightarrow l^{\pm}\nu + b\bar{b}$ and the corresponding background processes have been studied for TEVATRON and LHC center of mass energies.

Signal and background cross sections scale differently for 2 TeV and 14 TeV center of mass energy. At the higher energy the signal process cross sections were found to be higher by a factor of 10 if compared to the values at the lower center of mass energy while the factors for the background processes range up to 130.

This difference in the signal to background ratio degrades the prospects for a 5 σ discovery of a standard model Higgs boson within the mass range of 115 GeV/c^2 and 160 GeV/c^2 with the ATLAS detector. For the associated production of a Higgs boson a search at the TEVATRON is more promising than at LHC.

In agreement with previous studies it can be concluded that the search for associated production of a Standard Model Higgs boson with a Z^0 or $W^{\pm}$ gauge boson in the channels $l^+l^-b\bar{b}$ and $l^{\pm}\nu b\bar{b}$ alone is not sufficient for the discovery of a Higgs boson with a mass between 115 GeV/c^2 and 160 GeV/c^2 at the TEVATRON and the LHC.

A considerable spread of significances quoted in previous studies of associated Higgs production at the TEVATRON made it important to identify the crucial elements which influence the value of the significance.

With an enhanced fast detector simulation including the detector parameters of the DØ upgrade of interest for the final states $l^+l^-b\bar{b}$ and $l^{\pm}\nu b\bar{b}$ these elements were identified to be

- The parameterization of the **b-tagging efficiency**
- The parameterization of the **identification efficiency for light leptons**, in particular electrons
- The **di-jet mass resolution** for the invariant mass of the b-jets

Furthermore cross section values obtained with new Monte Carlo samples which include matrix element calculations not available before differ from those quoted in previous studies. These differences influence the final number of events for signal and background processes expected, degrading the value of significance.

A flexible object oriented analysis framework developed for this thesis made a reliable comparison of the enhanced detector simulation with the standard fast simulation of the DØ detector possible. It allows for the integration of different Monte Carlo generators and detector simulations and can be easily adapted and reused for future studies.

For the observation of a Higgs boson in the intermediate mass range decaying to a bottom quark-anti-quark pair the combination of both channels $\mathrm{Z^0H \to l^+l^-b\bar{b}}$ and $\mathrm{W^\pm H \to l^\pm \nu b\bar{b}}$ with other promising channels like $\mathrm{Z^0H} \to \nu\bar{\nu}$ increases the significance.

Nevertheless additional requirements have to be fulfilled if a 5 σ discovery should be achieved. Increasing the b-tagging efficiency above 65 % while keeping the mistagging probabilities low and enhancing the di-jet mass resolution for b-jets to 10 % or lower can increase the significance by a factor of 1.8.

Together with an increase in the integrated luminosity of a factor two and the combination of the data collected with both detectors DØ and CDF a 5 σ discovery is in reach. If new selection criteria and advanced analysis methods reducing the background contributions are applied a Higgs boson in the intermediate mass range can be discovered at the TEVATRON.

Appendix A

Initial Pythia settings

Table A.1: **Initial Pythia settings**

Switch	Value	Explanation
PMAS(6,1)	175.0	top quark mass in GeV/C^2
MSTP(51)	4053	CTEQ5M1 structure function
MSTP(52)	2	using PDF Library version 8.04
MSTP(61)	1	with ISR
MSTP(71)	1	with FSR
MSTP(81)	1	with multiple interactions
MSTP(82)	3	multiple interactions model
PARP(82)	2.41	lower $\mathrm{p_T}$ cut-off for multiple interactions
MSTP(111)	3	with fragmentation
MSTJ(41)	2	shower branching model
MSTJ(11)	4	longitudinal fragmentation function
PARJ(54)	-0.07	Peterson fragmentation parameter for c quarks
PARJ(55)	-0.006	Peterson fragmentation parameter for b quarks
PARJ(56)	-10^{-6}	Peterson fragmentation parameter for t quarks

Common settings for Pythia version 6.1 and 6.2

Table A.2: **Individual settings for $\mathrm{W^\pm b\bar{b}}$ and $\mathrm{Z^0 b\bar{b}}$**

Switch	Value	Explanation
VLPHOT	1	Full $\mathrm{Z^0}/\gamma^*$ propagator
VLPHMASS	10.0	Lower cut-off for off-shell photon mass in GeV/c^2
MSTP(191)	1	choice of scale for running coupling constant $\alpha_\mathrm{s}(\mathrm{Q})$, only for $\mathrm{W^\pm b\bar{b}}$

Individual settings for external processes to Pythia version 6.1

Appendix B

Branching ratios obtained from the Pythia Monte Carlo generator

Table B.1: **Branching ratios obtained from Pythia**

Decay channel	PYTHIA 6.203/6.161
$\mathrm{t} \to \mathrm{W}^{\pm}\mathrm{b}$	99.82%
$\mathrm{W}^{\pm} \to \mathrm{e}\nu_{\mathrm{e}}$	10.79%
$\mathrm{W}^{\pm} \to \mu\nu_{\mu}$	10.79%
$\mathrm{W}^{\pm} \to \tau\nu_{\tau}$	10.78%
$\mathrm{W}^{\pm} \to \mathrm{l}^{\pm}\nu, \quad \mathrm{l} = \mathrm{e}, \mu, \tau$	32.36%
$\mathrm{Z}^0 \to \mathrm{e}\bar{\mathrm{e}}$	3.349%
$\mathrm{Z}^0 \to \mu\bar{\mu}$	3.349%
$\mathrm{Z}^0 \to \tau\bar{\tau}$	3.341%
$\mathrm{Z}^0 \to \mathrm{l}^{+}\mathrm{l}^{-}, \quad \mathrm{l} = \mathrm{e}, \mu, \tau$	10.039%
$\mathrm{Z}^0 \to \mathrm{b}\bar{\mathrm{b}}$	15.24%

Branching ratios for decay channels. Note that no changes took place for the branching ratio values between version 6.161 and 6.203 of PYTHIA.

Appendix C

ATLFast detector simulation parameters for DØ and ATLAS

C.1 ATLFast cluster parameters

Table C.1: **ATLFast cluster parameters**

Detector	DØ	ATLAS	unit
Cone Radius	0.7	0.4	–
Rapidity coverage	4.0	5.0	–
granularity in η	0.1	0.1	–
granularity in ϕ	$2\pi/64$	0.1	–

Table C.2: **Explanation of ATLFast cluster parameters**

Variable for cluster	Explanation
Cone Radius	maximum cluster radius in the (η, ϕ) plane.
Rapidity coverage	rapidity coverage of the calorimeter system
granularity in η	calorimeter resolution in η
granularity in ϕ	calorimeter resolution in ϕ

C.2 ATLFast lepton parameters

Table C.3: **ATLFast electron parameters**

Detector	DØ	ATLAS	unit
Minimum E_T	5.0	5.0	GeV
Maximum pseudorapidity	2.6	2.5	–
Isolation radius	0.2	0.4	–

Table C.4: **ATLFast muon parameters**

Detector	DØ	ATLAS	unit
Minimum E_T	8.0	6.0	GeV
Maximum pseudorapidity	2.0	2.5	–
Isolation radius	0.5	0.4	–

Table C.5: **ATLFast tau parameters**

Detector	DØ	ATLAS	unit
Minimum E_T	10.0 (5.0 in section 3.4.2)	10.0	GeV
Maximum pseudorapidity	1.5	2.5	–
Isolation radius	0.4	0.3	–

Table C.6: **Explanation of ATLFast lepton parameters**

Variable for lepton	Explanation
Minimum E_T	minimum energy required for lepton reconstruction
Maximum pseudorapidity	value of $\|\eta\|$ up to which reconstruction is possible
Isolation radius	minimum distance in the (η, ϕ) plane to the next calorimeter cluster

C.3 ATLFast jet parameters

Table C.7: **ATLFast jet parameters**

Detector	DØ	ATLAS	unit
Minimum energy	10.0	10.0	GeV
Maximum pseudorapidity	2.5	5.0	–

Table C.8: **ATLFast b-jet parameters**

Detector	DØ	ATLAS	unit
Minimum p_T	5.0	5.0	GeV/c
Maximum pseudorapidity	2.5	2.5	–

Table C.9: **Explanation of ATLFast jet parameters**

Variable for jets and b-jets	Explanation
Minimum p_T	minimum transverse momentum for reconstruction/tagging
Maximum pseudorapidity	value of $\|\eta\|$ up to which reconstruction/tagging is possible

Bibliography

[1] The LEP working group for Higgs boson searches. Search for the Standard Model Higgs Boson at LEP. CERN-EP/ 2001-055, ALEPH, DELPHI, L3 and OPAL Collaborations, July 2001.

[2] D. Groom et al. Review of Particle Physics. *The European Physical Journal*, C15:1+, 2000.

[3] Q. Ho-Kim and X. Pham. *Elementary Particles and Their Interactions.* Springer-Verlag Berlin Heidelberg, 1998.

[4] P. Schmüser. *Feynman-Graphen und Eichtheorien für Experimentalphysiker.* Springer-Verlag Berlin Heidelberg, 1995.

[5] I. Aitchinson and A. Hey. *Gauge Theories in Particle Physics.* Institute of Physics Publishing Bristol and Philadelphia, 2nd edition, 1989.

[6] M. Peskin and D. Schroeder. *An Introduction to Quantum Field Theory.* Perseus Books Publishing, 1995.

[7] C. Yang and R. Mills. Conservation of Isotopic Spin and Isotopic Gauge Invariance . *Physical Review*, 96:191, 1986.

[8] S. Glashow. Partial Symmetries of Weak Interactions. *Nuclear Physics*, 22:579, 1961.

[9] A. Salam and J. Ward. Electromagnetic and Weak interactions. *Physics Letters*, 13:168, 1964.

[10] S. Weinberg. A Model of Leptons. *Physical Review Letters*, 19:1264, 1967.

[11] C. Wu, E. Hayward, D. Hoppes, and R. Hudson.

[12] R. Feynman. Mathematical Formulation of the Quantum Theory of Electromagnetic Interaction. *Physical Review*, 80:440, 1950.

[13] H. Fritzsch, M. Gell-Mann, and H. Leutwyler.

[14] J. Goldstone. Field Theories with "Superconductor" Solutions. *Nuovo Cimento*, 19:154, 1961.

[15] P. Higgs. Broken Symmetries, Massless Particles and Gauge Fields. *Physics Letters*, 12:132, 1964.

[16] Brout R. Englert, F. Broken Symmetry and the Mass of Gauge Vector Mesons. *Physical Review Letters*, 13:321, 1964.

[17] T. Kibble. Symmetry Breaking in Non-Abelian Gauge Theories. *Physical Review*, 155:1554, 1967.

[18] Y. Fukuda et. al. Measurement of a small atmospheric neutrino ν_μ/ν_e ratio. *Physics Letters*, B433:9–18, 1998.

[19] S. Glashow, J. Iliopoulos, and L. Maiani. Weak Interaction with Lepton-Hadron Symmetry. *Physical Review D*, 2:1285, 1970.

[20] M. Kobayashi and K. Maskawa. CP Violation in the renormalizable Theory of weak Interaction. *Progress of Theoretical Physics*, 49:625, 1973.

[21] G. Kane, editor. *Perspectives on Higgs Physics*, volume 13 of *Advanced Series on Directions in High Energy Physics.* World Scientific Publishing Co. Pte. Ltd., 1993.

[22] E. Eichten, I. Hinchcliffe, K. Lane, and C. Quigg. Supercollider physics. *Review of Modern Physics*, 56(4):579–707, October 1984. See also Erratum.

[23] E. Eichten, I. Hinchcliffe, K. Lane, and C. Quigg. Erratum: Supercollider physics. *Review of Modern Physics*, 58(4):1065–1073, October 1986.

[24] M. Spira. Higgs Boson Production and Decay at the Tevatron. hep-ph/ 9810289, October 1998.

[25] M. Carena, J. Conway, H. Haber, and J. Hobbs. Report of the Tevatron Higgs Working Group. hep-ph/ 0010338, October 2000.

[26] R. Feynman. *Photon-Hadron Interactions.* Westview Press, 1998.

[27] J. Bjorken. Asymptotic Sum Rules at Infinite Momentum. *Physical Review*, 179(5):1547–1553, March 1969.

[28] M. Gell-Mann. A Schematic Model of Baryons and Mesons. *Physics Letters*, 8:214, 1964.

[29] G. Zweig. An SU(3) Model for Strong Interaction Symmetry and its Breaking I. CERN- 8419-TH-412, 1964.

[30] G. Zweig. An SU(3) Model for Strong Interaction Symmetry and its Breaking II. CERN- 8419-TH-412, 1964.

[31] J. Poucher, M. Breidenbach, R. Ditzler, J. Friedman, and H. Kendall. High-Energy Single-Arm Inelastic e-p and e-d Scattering at 6 and 10. *Physical Review Letters*, 32(3):118–121, January 1973.

[32] C. Kiesling. *Tests of the Standard Theory of Electroweak Interactions.* Springer-Verlag Berlin Heidelberg, 1988.

[33] G. Altarelli and G. Parisi. Asymptotic Freedom in Parton Language. *Nuclear Physics B*, 126:298, 1977.

[34] H. Lai et al. Global QCD Analysis of Parton Structure of the Nucleon: CTEQ5 Parton Distributions. hep-ph/ 9903282, CTEQ collaboration, August 1999.

[35] C. Peterson, D. Schlatter, I. Schmitt, and P. Zerwas. Scaling violations in inclusive e^+e^- annihilation spectra. *Physical Review D*, 27(1):105–111, January 1983.

[36] K. Wille. *Physik der Teilchenbeschleuniger und Synchrotronstrahlungsquellen.* B.G. Teubner Stuttgart, 1996.

[37] J. Jackson. *Classical Electrodynamics.* Westview Press, 3rd edition, July 1998.

[38] Fermilab Beams Division. www-bd.fnal.gov/runii/index.html. Website, December 2001. see also the Beam Division's homepage http://adwww.fnal.gov.

[39] D. McGinnis. TEVATRON Collider Luminosity Upgrades. Talk at the joint experimental theoretical physics seminar, Fermilab Beams Division, March 2001. see http://www-bd.fnal.gov/runII.

[40] PS Division. http://cern.web.cern.ch/cern/divisions/ps/welcome.html. Website, December 2001.

[41] SL Division. http://cern.web.cern.ch/cern/divisions/sl/welcome.html. Website, December 2001.

[42] The LHC project. http://lhc.web.cern.ch. Website, December 2001.

[43] ATLAS detector and physics performance Technical Design Report Vol.I. ATLAS TDR 14, CERN/LHCC 99-14, ATLAS Collaboration, May 1999.

[44] K. Grupen. *Teilchendetektoren.* BI Wissenschaftsverlag, 1993.

[45] K. Kleinknecht. *Detectors for particle radiation.* Cambridge University Press, 1998.

[46] The DØ Upgrade - The Detector and Its Physics. D0 pub-96/357-e, DØ collaboration, July 1996. see also the DØ website at http://www-d0.fnal.gov/.

[47] DØ collaboration. The DØ Detector. *Nuclear Instruments and Methods in Physics Research*, A338:185, 1994.

[48] M. Narain. The DØ Upgrade. Overview talk given at the institut des sciences nucleaire de grenoble, Boston University, 2001. see http://isnwww.in2p3.fr/d0/documentation/materials.html.

[49] D. Schinzel. High-resolution electro-magnetic calorimetry with noble liquids. *Nuclear Instruments and Methods in Physics Research A*, 419:217–229, 1998.

[50] F. Bauer, U. Bratzler, S. Chouridou, M. Deile, H. Dietl, O. Kortner, H. Kroha, T. Lagouri, A. Manz, A. Ostapchuk, R. Richter, S. Schael, A. Staude, R. Ströhmer, and T. Trefzger. Construction and Test of MDT Chambers for the ATLAS Muon Spectrometer. submitted to NIM A, 2000.

[51] M. Jaffré. EM ID Status. Technical report, DØ EM ID Group, June 2000. DØ workshop 2000.

[52] M. Bhattarcharjee. Triggering on electrons/photons. Em id talk, DØ EM ID Group, January 2000.

[53] C. Leonidopoulos. The Muon Trigger at DØ. Chep 2001 talk, DØ Collaboration, 2000.

[54] T. Trefzger, R. Ströhmer, and T. Christiansen. Muon identification. Talk given at the DØ Meeting Mainz, LMU Munich, March 2000.

[55] DØ Tau ID Group. Website, December 2001.

[56] Y. Gershtein. Tau ID. ADM talk, DØ Tau ID Group.

[57] I. Iashvili. First look at "gamma+jet" events in data. ADM talk, DØ JES Group, August 2000.

[58] R. Van Koten. Status and Plans for Heavy Flavor/b-id. B id status talk at convenor's meeting, DØ B ID group, October 2001.

[59] T. Sjöstrand. High-Energy-Physics Event Generation with PYTHIA 5.7 and JETSET 7.4. *Comp. Phys. Comm.*, 82:74, 1994.

[60] B. Kersevan and E. Richter-Waş. The $\mathrm{q\bar{q}} \to \mathrm{W}(\to \mathrm{l}\nu)\mathrm{g}^*(\to \mathrm{b\bar{b}})$ process: matrix element implementation to Pythia 6.1. ATLAS Physics Notes ATL-PHYS-2001-020, July 2001.

[61] B. Kersevan and E. Richter-Waş. The $\mathrm{gg}, \mathrm{q\bar{q}} \to \mathrm{Z}/\gamma^*(\to \mathrm{ll})\mathrm{b\bar{b}}$ processes: matrix element implementation to Pythia 6.1. ATLAS Physics Notes ATL-PHYS-2001-021, July 2001.

[62] E. Richter-Waş. Prospects for the observability of the WH and ZH, H-¿bb channels in 14 TeV pp and 2 TeV pp collisions. ATLAS Physics Notes ATL-PHYS-2000-023, October 2000.

[63] E. Richter-Waş. Revisiting the observability of the WH and ZH, H-¿bb channel in 14 TeV pp and 2 TeV pp collisions. ATLAS Physics Notes ATL-PHYS-2000-024, August 2000.

[64] ATLAS detector and physics performance Technical Design Report Vol.II. ATLAS TDR 15, CERN/LHCC 99-15, ATLAS Collaboration, May 1999.

[65] E. Richter-Waş, D. Froidevaux, and Luc Poggioli. ATLFAST 2.0 – a afst simulation package for ATLAS. ATLAS Physics Notes ATL-PHYS-98-131, November 1998.

[66] Sjöstrand T., Lönnbald L., and S. Mrenna. Pythia 6.2, Physics and Manual. hep-ph/ 0108264, August 2001.

[67] R. Brun and F. Rademakers. ROOT - An Object Oriented Data Analysis Framework. In *Proceedings AIHENP'96 Workshop, Lausanne*, 1996. Nucl. Inst. & Meth. in Phys. Res. A 389 (1997) 81-86.

[68] A. Schwartzmann and M. Narain. Technical report.

[69] P. Bhat, R. Gilmartin, and H. Prosper. Strategy for discovering a low-mass Higgs boson at the Fermilab Tevatron. hep-ph/ 0001152v3, August 2000.

Acknowledgements

Zuallererst möchte ich mich bei Frau Professorin Dr. Dorothee Schaile für die Aufgabenstellung und die Möglichkeit an ihrem Lehrstuhl arbeiten zu dürfen bedanken.

Bedanken möchte ich mich auch bei

- Thomas Trefzger für seine Betreuung meiner Diplomarbeit und die Diskussionen, die mir geholfen haben, die assoziierte Higgs Produktion und ihre Analyse zu verstehen.
- Cornelius Fritz Vollmer, der mir mit seinem Einsatz und seinem Humor bei der Erstellung und Korrektur der Arbeit sehr geholfen hat.
- Jörg Dubbert, der mir immer zur Verfügung stand für Fragen und mir ebenfalls eine grosse Hilfe war.
- Birgit Bussmann, wegen des Nachnamens.
- Otto Schaile für die Hilfe bei allen Computerproblemen und der Rettung meiner Arbeit vor dem Festplattencrash.
- Günter Duckeck und Raimund Ströhmer, die fast immer eine Antwort auf meine Fragen wussten.

und natürlich danke ich auch:

Oliver Sahr, Axel Leins, Johannes Elmsheuser, Philipp Schieferdecker, Wolfram Stiller, Felix Rauscher, Oliver Kortner, Sofia Chouridou, Meta Binder, Jana Traupel, Herta Franz und allen anderen.

Zuletzt möchte ich meinen Eltern danken, denen ich diese Arbeit widmen möchte.

Danke.

Ich versichere hiermit, die vorliegende Arbeit selbständig verfasst zu haben und keine anderen als die angegebenen Quellen und Hilfsmittel verwendet zu haben.

Michael Bussmann

München, 14. Februar 2002